Technical Report Documentation Page

1. Report No. FHWA/TX-0-1805-1	2. Government Accession No.	3. Recipient's Catalog No.
4. BACKWATER EFFECTS OF PIERS IN SUBCRITICAL FLOW		5. Report Date October 2001
7. Author(s) Randall J. Charbeneau and Edward R. Holley		6. Performing Organization Code 8. Performing Organization Report No. Research Report 0-1805-1
9. Performing Organization Name and Address Center for Transportation Research The University of Texas at Austin 3208 Red River, Suite 200 Austin, TX 78705-2650		10. Work Unit No. (TRAIS) 11. Contract or Grant No. 0-1805
12. Sponsoring Agency Name and Address Texas Department of Transportation Research and Technology Implementation Office P.O. Box 5080 Austin, TX 78763-5080		13. Type of Report and Period Covered Project Summary Report, 1999-2001 14. Sponsoring Agency Code

15. Supplementary Notes
Project conducted in cooperation with the U.S. Department of Transportation, Federal Highway Administration, and the Texas Department of Transportation.

16. Abstract
Construction or renovation of bridge structures may require placement of bridge piers within the channel or floodplain of natural waterways. These piers will obstruct the flow and may cause an increase in water levels upstream of the bridge structure. The water level increase caused by the presence of bridge piers is called backwater. In this experimental research, the backwater effects caused by bridge piers were investigated in the laboratory for different pier sizes and for a range of subcritical flow conditions. Both water level changes and drag forces on bridge piers were measured during two research programs. The results from this research suggest that use of standard formula for calculation of backwater will over-predict water level increases. An improved formula for calculating backwater is presented.

17. Key Words piers, backwater, drag forces, Yarnell's equation	18. Distribution Statement No restrictions. This document is available to the public through the National Technical Information Service, Springfield, Virginia 22161.

19. Security Classif. (of report) Unclassified	20. Security Classif. (of this page) Unclassified	21. No. of pages 110	22. Price

Form DOT F 1700.7 (8-72) Reproduction of completed page authorized

BACKWATER EFFECTS OF BRIDGE PIERS IN SUBCRITICAL FLOW

by

Randall J. Charbeneau and Edward R. Holley

Research Report Number 0-1805-1

Research Project 0-1805
Evaluation of the Extent of Backwater Effects of Bridge Piers

Conducted for the

TEXAS DEPARTMENT OF TRANSPORTATION

in cooperation with the

U.S. Department of Transportation
Federal Highway Administration

by the

CENTER FOR TRANSPORTATION RESEARCH
Bureau of Engineering Research
THE UNIVERSITY OF TEXAS AT AUSTIN

October 2001

DISCLAIMERS

The contents of this report reflect the views of the authors, who are responsible for the facts and the accuracy of the data presented herein. The contents do not necessarily reflect the official views or policies of the Federal Highway Administration or the Texas Department of Transportation. This report does not constitute a standard, specification, or regulation.

There was no invention or discovery conceived or first actually reduced to practice in the course of or under this contract, including an art, method, process, machine, manufacture, design or composition of matter, or any new and useful improvement thereof, or any variety of plant which is or may be patentable under the patent laws of the United States of America or any foreign country.

This report was prepared in cooperation with the Texas Department of Transportation and the U.S. Department of Transportation, Federal Highway Administration.

ACKNOWLEDGMENTS

The authors express appreciation to Amy Ronnfeldt, TxDOT project director for this study, for her guidance and support.

NOT INTENDED FOR CONSTRUCTION, PERMIT, OR BIDDING PURPOSES

Edward R. Holley, P.E. (Texas No. 51638)
Research Supervisor

TABLE OF CONTENTS

CHAPTER 1. INTRODUCTION 1
1.1. Background 1
1.2. Study Objectives 2
1.3. Overview 2

CHAPTER 2. LITERATURE REVIEW 3
2.1. Introduction 3
2.2. Backwater Equations 4
2.3. Type I Flow Definition 9
2.4. Definition of Drag Forces on Piers 11
2.5. Determination of Drag Coefficient from Momentum Equation 13
2.6. Physical Model Studies 16
2.7. Accounting for Backwater Using Manning's Equation 19
2.8. High Cost of Regulations 20

CHAPTER 3. EQUIPMENT 23
3.1. Introduction 23
3.2. The Channel 23
3.3. Pumps 24
3.4. Piers 26
3.5. Flow Rate 27
3.5.1. Flow Meters 27
3.5.2. Venturi Meter 28
3.5.3. Thin-Plate Weir 32
3.6. Water Level 34
3.7. Drag Force Equipment 34
3.7.1. Mechanical Components 34
3.7.1.1. Model Pier 34
3.7.1.2. Other Model Components 38
3.7.2. Electrical and Electronic Components 45
3.7.2.1. Strain Gages 45
3.7.2.2. Strain Gage Conditioner and Amplifier System 48
3.7.2.3. Two-Channel Digital Oscilloscope 48
3.7.2.4. Data Transfer Software 49
3.7.3. Calibration Procedure 49
3.7.4. Calibration Results 51

CHAPTER 4. EXPERIMENTAL PROCEDURES 55
4.1. Introduction..... 55
4.2. Drag Coefficient for Bridge Piers..... 55
4.3. Backwater Effect of Bridge Piers..... 57
4.3.1. Data Collection..... 57
4.3.2. Processing Water Level Data 59

CHAPTER 5. RESULTS AND ANALYSIS 65
5.1. Introduction..... 65
5.2. Flow Calibration..... 65
5.3. Drag Coefficient Results..... 68
5.4. Backwater Results..... 75
5.5. Two-Dimensional Mound of Water Upstream of Piers 77
5.6. Comparison between Yarnell's Equation and the Experimental Data 79
5.7. Drag Coefficients and Scale Effects 85

CHAPTER 6. SUMMARY, DISCUSSION, AND CONCLUSIONS 91

CHAPTER 7. REFERENCES..... 93

APPENDIX A. DATA FROM DRAG FORCE EXPERIMENTS..... 95

APPENDIX B. DATA FROM BACKWATER EXPERIMENTS..... 99

CHAPTER 1. INTRODUCTION

1.1. BACKGROUND

The construction or renovation of bridge structures may require placement of bridge piers within the channel or floodplain of natural waterways. These piers will obstruct the flow and may cause an increase in water levels upstream of the bridge structure. The amount of obstruction caused by a bridge pier depends mainly upon its geometric shape, its position in the stream, the quantity of flow, and the percentage of channel contraction. Investigation of how pier shape influences channel obstruction and hydraulic efficiency is an important issue in bridge design. Furthermore, it has been postulated that the hydraulic effects of the piers are localized and dissipate quickly in the upstream direction. As yet, there has been no investigation of this postulate.

For subcritical channel flow, which is the type of flow that exists in most rivers, the rise in the water level due to bridge piers and abutments is usually assumed to occur where the flow contraction begins upstream of the bridge. This distance upstream of the bridge is approximately equal to the average encroachment distance of the roadway embankment into the channel. The hydraulic effects of bridge piers on backwater profiles have traditionally been included in the overall backwater effects of a roadway crossing of a stream.

The National Flood Insurance Program, which is administered by the Federal Emergency Management Agency (FEMA), requires permits for channel improvements and floodway map revisions for any encroachment into a designated floodway. FEMA considers bridge piers in a floodway to be an encroachment, so regulations effectively allow no increase in the water surface without a map revision due to the piers. The map review, while both time-consuming and expensive, can also include the possibility of purchasing flood easements, yielding another construction-related cost.

The current work attempts to evaluate the water level change due to bridge piers and to study the nature of the variation of water surface upstream of the piers.

1.2. STUDY OBJECTIVES

The following three objectives were addressed in the current effort:

1. Evaluate the drag coefficient of bridge piers to obtain a better understanding of scaling relationships between laboratory and prototype conditions;
2. Compare the obtained experimental values to the results provided by previous studies and, where appropriate, develop models that relate the water level variation to the Froude number (and possibly other factors); and
3. Study the nature of the water level variation upstream of the piers.

To accomplish these objectives, two series of experiments were performed using a large physical model. The first series evaluated the drag coefficient, while the second series focused on water level variation.

1.3. OVERVIEW

Much research has been undertaken on backwater effects from channel obstructions, and a few studies relate specifically to bridge piers. Differences exist among the research findings. The current research effort addresses the differences in the literature equations to predict backwater effects of bridge piers and their upstream influence based on a series of experiments. The research data were analyzed in order to develop a new equation that relates the backwater to the Froude number and to the amount of obstruction caused by the piers.

Chapter 2 provides both a review of literature that quantifies the effects of different pier shapes and the theoretical background for the problem analyzed. Chapter 3 presents the experimental facilities and describes the materials and equipment used. Chapter 4 describes the experimental procedures and the data. Chapter 5 provides an interpretation and a discussion of the results. Conclusions and recommendations are presented in Chapter 6.

CHAPTER 2. LITERATURE REVIEW

2.1. INTRODUCTION

Any obstacle in a river has a drag force exerted on it by the flow and causes an energy loss in the flow. Whether viewed in terms of drag force or energy loss, the flow must adjust itself to compensate for the effects of the obstacle. In subcritical open channel flow, which is the type of flow that exists in most rivers, one of the primary adjustments due to bridge piers is an increase in the water level (Δy) upstream of the obstacle (Figure 2.1). The higher upstream water level caused by piers provides both the force to overcome the drag on the pier and a higher energy level to overcome the energy loss due to the pier.

This chapter presents an overview of the most important previous work done to quantify the value of the water level upstream of an obstacle such as a bridge pier. Definition of the drag forces, which are responsible for the increase in water elevation, is also provided. Moreover, a theoretical study is developed explaining the relations between a prototype and a model to achieve a better representation of actual conditions.

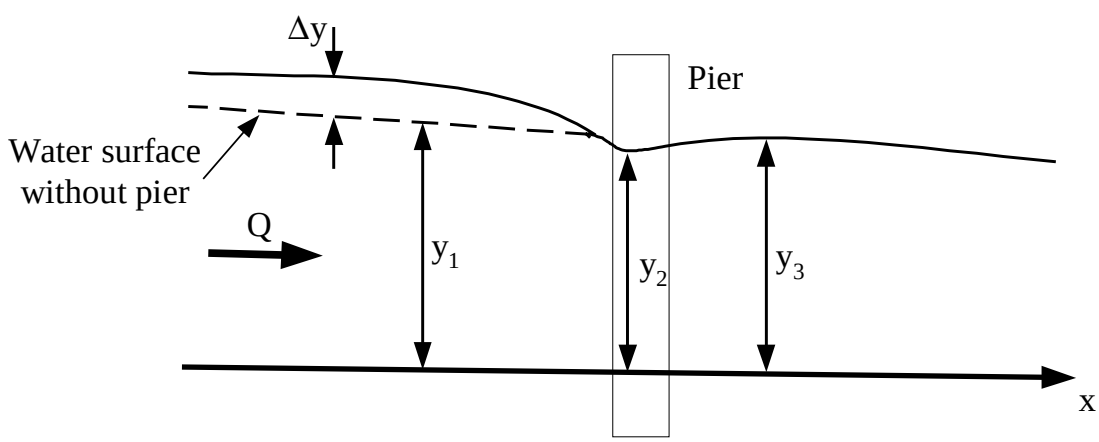

Figure 2.1: Schematic profile of a river in the vicinity of a pier

2.2. BACKWATER EQUATIONS

Most researchers have been interested in computing the magnitude of the backwater Δy. Among the hydraulicians who were interested in the obstruction caused by bridge piers were Yarnell (1934a,b), D'Aubuisson (1852), Nagler (1918), Rehbock (1919), and Al-Nassri (1994).

The most widely used equation for calculating the increase in the water level due to bridge piers is the Yarnell equation (Yarnell, 1934a, 1934b):

$$\Delta y = 2K\left(K + 5Fr_3^{\,2} - 0.6\right)\left(\alpha + 15\alpha^4\right)\frac{V_3^{\,2}}{2g} \tag{2.1}$$

Equation 2.1 may also be written in the following form

$$\frac{\Delta y}{y} = K\left(K + 5Fr_3^{\,2} - 0.6\right)\left(\alpha + 15\alpha^4\right)Fr_3^{\,2} \tag{2.2}$$

In Equations 2.1 and 2.2, Δy is the backwater generated by the bridge pier(s), y is the original (i.e., undisturbed) local flow depth, Fr_3 is the corresponding Froude number at section 3 downstream of piers (Figure 2.1), α is the ratio of the flow area obstructed by the piers to the total flow area downstream of the piers, and K is a coefficient reflecting the pier shape. Yarnell's experimentally obtained values for K are summarized in Table 2.1. Note that for the twin-cylinder piers, L is the distance between the two piers and D is the diameter of each pier.

Table 2.1: Bridge pier backwater coefficients (after Yarnell 1934b)

Pier shape	K
Semicircular nose and tail	0.9
Lens-shaped nose and tail	0.9
Twin-cylinder piers with connecting diaphragm (L/D = 4)	0.95
Twin-cylinder piers without diaphragm (L/D = 4)	1.05
90º triangular nose and tail	1.05
Square nose and tail	1.25

Equations 2.1 and 2.2 are for flows classified as Class A by Yarnell and as Type I (Section 2.3) by TxDOT. These are low flows that do not impinge on the bridge superstructure and which remain subcritical throughout the region of flow contraction so that the flow

contraction does not cause critical flow to occur. Yarnell used α values of 11.7%, 23.3%, 35%, and 50% in his experiments. In spite of the relatively large values of α compared to present designs, Yarnell equation's is used for the effects of bridge piers in popular computer programs such as HEC-2 and HEC-RAS. Soon after the equation was published, it was found to have acceptable agreement with prototype tests (Anon, 1939). However, some limitations have been noted when Yarnell's equation is used in the HEC-2 computational model (Wisner *et al*., 1989).

One reason that Yarnell's equation has found wide acceptance is probably the large number of experiments that were performed. Yarnell did 2600 experiments in a large channel; although not all of them were for Type I flows. His channel was 10 ft (3.05 m) wide with flows up to 160 ft^3/s (4.5 m^3/s). Most of Yarnell's piers were rectangular in plan form, 14 in. (35.6 cm) wide by 3.5 ft (1.07 m) long, giving an aspect (length to width) ratio of 3:1. Other shapes (e.g., semicircles, 90º triangles) were added on the nose and tail (upstream and downstream ends of the pier). The additional nose and tail made the overall aspect ratio 4:1 or a little greater. He called these piers the "regular" or "standard" piers. For these piers, he used eleven different combinations of end shapes in his first series of tests and fourteen combinations in his second series. His third and fourth series had a much smaller variation of geometry. These tests included a few tests with two in-line circular piers with a web or with cross bracing. To investigate the effect of the aspect ratio, he also did tests with rectangles two and three times longer than the rectangles for the standard piers. These piers had overall aspect ratios of 7:1 to 13:1.

While Yarnell's equation has found wide acceptance, certain limitations of the HEC-2 model with Yarnell's equation have been demonstrated by comparing the results from a physical model to those from the computational model (Wisner *et al*., 1989). Specifically, the limitations were found to be associated with the channel cross sections, skew, and actual pier shapes.

As a first step in bridge hydraulics, the HEC-2 model determines the nature of the flow through the structure. Next, in the case of Type I conditions, it applies Yarnell's empirical equation. Yarnell's equation was developed from physical model experiments performed in a rectangular channel with regular cross sections upstream and downstream of the obstruction.

This geometry is not present in many rivers where cross sections in the vicinity of a bridge can be highly irregular. Moreover, Yarnell indicated that his formula holds for a skew (angle between the channel centerline and the perpendicular to the bridge structure) of up to 10-degrees only, which is not the case for many bridges. As for the determination of K, it is clear that Yarnell did not cover all the possible pier shapes in his experiments, which obliges the designer to approximate a K value in the case where the piers have special geometric forms.

Comparing the results obtained from HEC-2 and from a physical model showed that differences in water surface elevations across a particular section vary with the discharge (Wisner *et al*., 1989). These differences were found to be acceptable for all flows except for the 500-year discharge. For this latter case the difference between calculated and measured flow was significant, and Wisner *et al*. (1989) concluded that HEC-2 with Yarnell's equation cannot simulate all flow conditions.

Research carried out by D'Aubuisson (1852) also resulted in an equation for estimating backwater. With Figure 2.2 representing a bridge pier with water flowing through the contracted region, the D'Aubuisson equation is based on the theory that the drop H_2 in the water surface is defined as the difference of the velocity heads between the two positions 1 and 2 (Figure 2.2). He concluded that

$$\frac{\Delta y}{y} = \left[\frac{8}{27K_{DA}^2} \frac{(1+0.5Fr_{3c}^2)^3}{Fr_{3c}^2} - \left(\frac{1}{1+\Delta y/y} \right)^2 \right] \frac{Fr_3^2}{2} \tag{2.3}$$

where Fr_{3c} is the Froude number at Section 3 downstream of the piers (Figure 2.1) when choked or critical flow occurs at Section 2 and K_{DA} is the D'Aubuisson pier-shape coefficient. Table 2.2 gives the value of K_{DA} for Type I flow for different shapes of piers.

Nagler (1918) proposed

$$\frac{\Delta y}{y} = \left[\frac{8}{27K_N^2} \frac{(1+0.5Fr_{3c}^2)^3}{Fr_{3c}^2(1-0.3Fr_3^2/2)} - \beta \left(\frac{1}{1+\Delta y/y} \right)^2 \right] \frac{Fr_3^2}{2} \tag{2.4}$$

where β is a correction coefficient that depends on the conditions at the site of the bridge pier and K_N is the Nagler pier-shape coefficient. β varies with the percentage of channel contraction. K_N values for some pier shapes and for Type I flow are presented in Table 2.3.

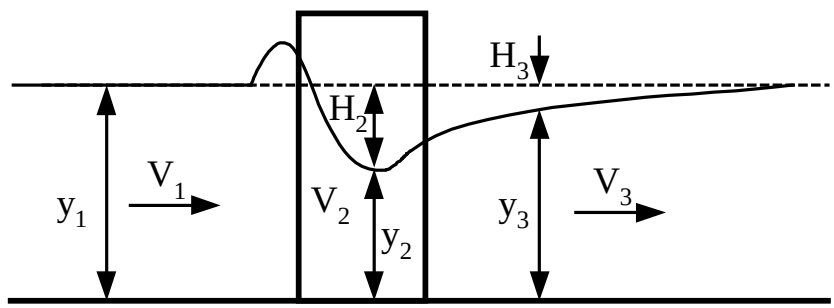

Figure 2.2: Bridge pier with the water flowing through the contracted region

Table 2.2: Bridge pier backwater coefficients (after D'Aubuisson, 1852)

Pier shape	K_{DA}
Semicircular nose and tail	1.079
Lens-shaped nose and tail	1.051
Twin-cylinder piers with connecting diaphragm (L/D = 4)	0.966
Twin-cylinder piers without diaphragm (L/D = 4)	0.991
90º triangular nose and tail	1.05
Square nose and tail without batter	1.065

Table 2.3: Bridge pier backwater coefficients (after Nagler, 1918)

Pier shape	K_N
Semicircular nose and tail	0.934
Lens-shaped nose and tail	0.952
Twin-cylinder piers with connecting diaphragm (L/D = 4)	0.907
Twin-cylinder piers without diaphragm (L/D =4)	0.892
90º triangular nose and tail	0.887
Square nose and tail without batter	0.871

According to Rehbock (1919), the equation for computing the backwater height for all pier shapes in a rectangular channel with "ordinary flow" is

$$\frac{\Delta y}{y} = \frac{1}{2}\left[\delta_0 - \alpha(\delta_0 - 1)\right]\left[0.4\alpha + \alpha^2 + 9\alpha^4\right] Fr_3^2\,(1 + Fr_3^2) \qquad (2.5)$$

where δ_0 is the Rehbock pier-shape coefficient. Rehbock stated that this equation is for ordinary or "steady" flow, i.e., flow where water passes the obstruction with very slight or no turbulence. Table 2.4 gives the value of δ_0 for different shapes of piers.

Table 2.4: Bridge pier backwater coefficients (after Rehbock, 1919)

Pier shape	δ_0
Semicircular nose and tail	3.35
Lens-shaped nose and tail	3.55
Twin-cylinder piers with connecting diaphragm (L/D = 4)	5.99
Twin-cylinder piers without diaphragm (L/D = 4)	6.13
90º triangular nose and tail	3.54
Square nose and tail without batter	2.64

Al-Nassri (1994) summarized the results of another study on the effect of bridge piers on backwater. The results of his experimental study can be written as

$$\frac{\Delta y}{y_3} = \frac{0.0678}{\varphi^{0.95}}\left[\frac{Fr_3}{(1-\alpha)^{1.8}}\right]^{2.29} \tag{2.6}$$

where φ is a shape factor, which was defined as the ratio of the geometrical cross-sectional area of the pier to the area of the separation zone downstream of the piers. This equation is based on experiments that also included large values of α ranging from 7% to 47%. Al-Nassri gave φ = 2.36 for square piers, 3.19 for circular piers, and 5.85 for piers with semicircular nose and tail. He did not give the aspect ratio for the piers with a semicircular nose and tail.

A comparison of Equations 2.2 through 2.6 is shown in Figure 2.3 for semicircular nose and tail piers. Each of the curves stops at an approximate limit of TxDOT Type I flow (Yarnell's Class A flow) where the piers choke the channel, i.e., at the conditions that force critical depth to occur near the piers (Equation 2.12). An expansion loss coefficient of 0.5 was used in calculating the Fr at which choking occurs. As Figure 2.3 shows, there is an order of magnitude difference between the predictive equations. The reason for this large difference is not yet known. At the very least, the differences in Figure 2.3 illustrate that extreme care is needed in conducting experiments to determine the effects of piers.

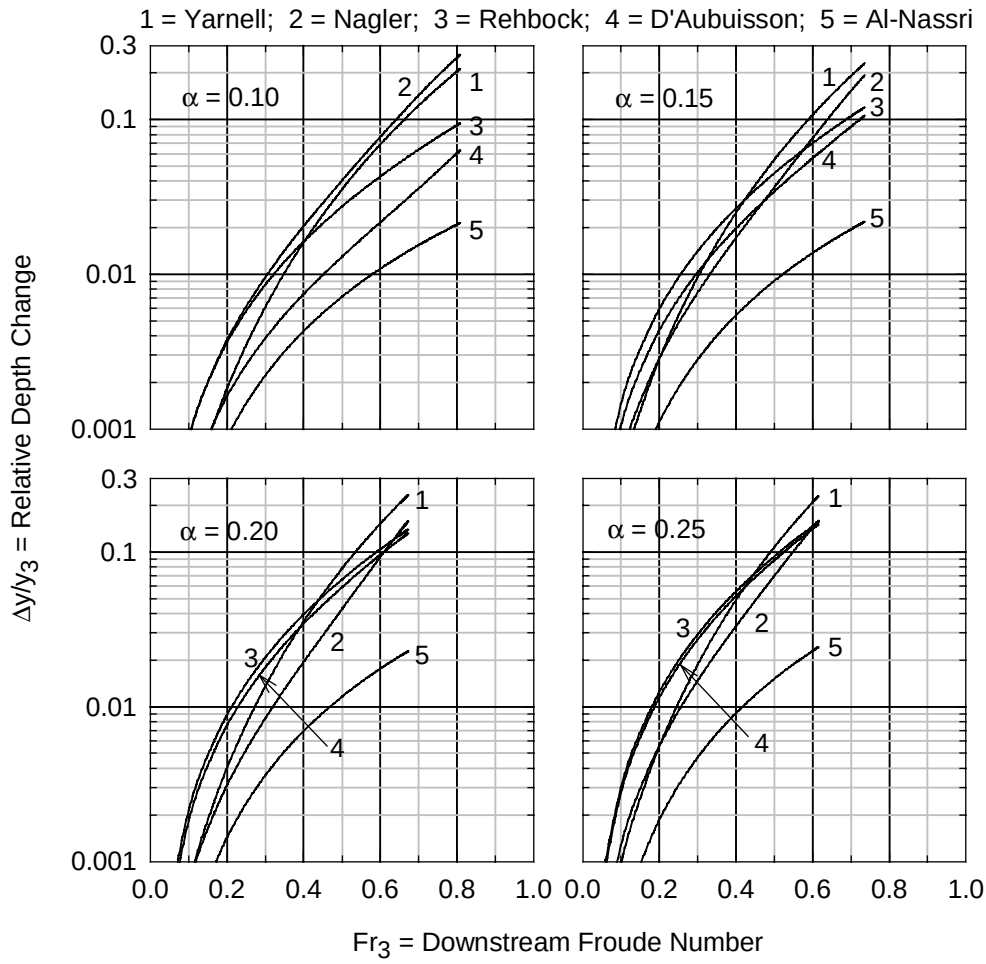

Figure 2.3: Various empirical relationships for backwater

2.3. TYPE I FLOW DEFINITION

Type I flow is defined as being a low flow that does not impinge on the superstructure and remains subcritical in the contracted region. The limit of such a flow is given in this section. Letting cross section 2 be at the most contracted flow (Figure 2.1) and assuming a rectangular channel, critical flow gives

$$y_2 = y_c = \frac{V_2^2}{g} \tag{2.7}$$

where y_c is the critical depth. The energy equation between cross section 2 and 3 (Figure 2.1) for a horizontal channel is

$$\left(y+\frac{V^2}{2g}\right)_2 - K_L\left(\frac{V_2^2}{2g}-\frac{V_3^2}{2g}\right)=\left(y+\frac{V^2}{2g}\right)_3 \tag{2.8}$$

where K_L is an expansion-loss coefficient. Elimination of V_2 using Equation 2.7 and some rearrangement give

$$\frac{y_2}{y_3}=\frac{2+(1-K_L)Fr_3^2}{3-K_L} \tag{2.9}$$

If it is assumed that the width of the separation zone downstream of each pier is the same as the width of the pier, then continuity gives

$$V_2 y_2 (1-\alpha)B = V_3 y_3 B \tag{2.10}$$

Again, elimination of V_2 using Equation 2.7 and some rearrangement give

$$\alpha = 1-\frac{Fr_{3c}}{(y_2/y_3)^{3/2}} = 1-\frac{Fr_{3c}}{(y_c/y_3)^{3/2}} \tag{2.11}$$

where Fr_{3c} is the downstream Froude number for which choked conditions occur. Substitution of Equation 2.9 into Equation 2.11 gives

$$\alpha = 1-\left(\frac{3-K_L}{2+(1-K_L)Fr_{3c}^2}\right)^{3/2} Fr_{3c} \tag{2.12}$$

as the relationship between α and Fr_{3c}. The limit of Type I flow in Figure 2.3 came from this equation with $K_L = 0.5$ for expansion losses. Values of Fr_{3c} for various values of α and K_L are shown in Figure 2.4.

If the separation zone is wider than the piers, then each of the α values in Figure 2.4 for a given Fr_{3c} value should be reduced in proportion to the increase in the width of the separation zone. For example, if the separation zone is 10% wider, then the α value should be divided by 1.10. Similarly, a larger separation zone causes Fr_{3c} to be smaller for a given α value, but there is not a simple relationship for determining the change in Fr_{3c}. The numerical

value of the smaller Fr_{3c} can be obtained from Equation 2.12 by multiplying α by 1 plus the fractional increase (e.g., by 1.10 if the separation zone is 10% wider than the pier) and solving Equation 2.12 for Fr_{3c}.

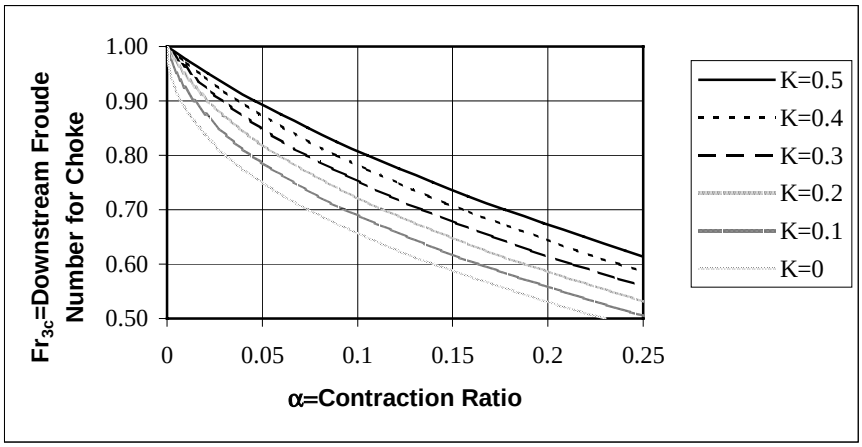

Figure 2.4: Limiting downstream Froude numbers for choked conditions

2.4. DEFINITION OF DRAG FORCES ON PIERS

As noted previously, drag forces on bridge piers cause energy loss in the flow and consequent water level increase upstream of the obstacle for subcritical flows. For flows with no free surface, the total drag on a body is the sum of the friction drag and the pressure drag:

$$F_D = F_f + F_p \tag{2.13}$$

where F_f is due to the shear stress on the surface of the object and F_p is due to the pressure difference between the upstream and downstream surfaces of the object.

In the case of a well-streamlined body, such as an airplane wing or the hull of a submarine, the friction drag is the major part of the total drag. Only rarely is it desired to compute the pressure drag separately from the friction drag. When the wake resistance becomes significant, one usually is interested in the total drag only, which is the case with bridge piers. Moreover, the analysis of drag forces on piers and the associated drag coefficients is helpful in understanding both previous experimental results and proper physical modeling of bridge piers.

For open channel flow, the drag consists of three components:

1) Surface drag, which is due to the shear stress acting on the surface of the pier.
2) Form drag, which is due to the difference between the higher pressure on the upstream side of the pier (where the flow impacts on the pier and where the depth is greater) and the lower pressure in the wake or separation zone on the downstream side of the pier.
3) Wave drag, which is due to the force required to form the standing surface waves around a pier.

As noted at the beginning of Section 2.1, river flow exerts a drag force on bridge piers. The drag force F_D can be expressed as:

$$F_D = C_D \rho \frac{V^2}{2} A_{pier} \tag{2.14}$$

where C_D = drag coefficient, ρ = fluid density, A_{pier} = projected area of the submerged part of a pier onto a plane perpendicular to the flow direction, and V = flow velocity. The undisturbed flow conditions immediately downstream of the pier are used to evaluate A_{pier} and V.

The functional dependence of pier drag coefficients for rectangular channels can be written as

$$C_D = f\left(\text{pier shape}, Re_p, \frac{k_p}{B_p}, I_T, Fr, \frac{B_p}{B}, \frac{B_p}{y}\right) \tag{2.15}$$

where Re_p = pier Reynolds number, which is given by

$$Re_p = \frac{VB_p}{\nu} \tag{2.16}$$

where V = flow velocity, B_p = width of pier perpendicular to the flow, ν = kinematic viscosity, k_p = roughness of pier surface, I_T = turbulence intensity in the approach flow, Fr = Froude number, which is given by

$$Fr = \frac{V}{\sqrt{gy}} \tag{2.17}$$

where g = acceleration of gravity, y = flow depth, and B = channel width. In Equation 2.15, the pier shape, k_p/B_p (a relative roughness), B_p/B, and B/y are basically geometric parameters. B_p/B is indicative of the blockage caused by the piers and is essentially the same as α in Equations 2.1 and 2.6. B_p/y is an aspect ratio and probably is not very important for piers since there is no flow over or under the ends of a pier. Re_p represents the effects of viscosity and is important primarily for piers that are curved in plan view (e.g., circular piers rather than square ones).

2.5. DETERMINATION OF DRAG COEFFICIENT FROM MOMENTUM EQUATION

The backwater, or the increase in water surface elevation (Δy) immediately upstream of a pier, is schematically illustrated in Figure 2.1. A theoretical approach based on the development of the momentum equation can quantitatively relate the magnitude of Δy to the drag force on the pier. To make the analysis tractable, the flow conditions are idealized as shown in Figure 2.5, where all the forces are shown as they act on the water. In particular, the drag force on the water is equal and opposite of the force on the pier. In the following analysis, it is assumed that the velocity distribution is relatively uniform at each cross section and that the channel slope is small so that the differences between the horizontal and flow directions and between vertical direction and the normal to the bed are negligible. The one-dimensional momentum equation for the control volume from cross section 1 to cross section 3 gives

$$F_{p1} - F_{p3} - F_{\tau 1} - F_{\tau 3} + W_{x1} + W_{x3} - F_D = \rho Q(V_3 - V_1) \tag{2.18}$$

where F_p = pressure force, F_τ = boundary shear force, W_x = x component of the weight of water (not shown), F_D = drag force, and Q = flow rate.

The pressure force for any shaped cross section is $\bar{p}A$, where $\bar{p}$ is the pressure at the centroid of the cross sectional area and A is the flow area. For a rectangular channel of width B, the net pressure force is

$$F_p = F_{p1} - F_{p3} = (\bar{p}A)_1 - (\bar{p}A) = \gamma \frac{y_1}{2} y_1 B - \gamma \frac{y_3}{2} y_3 B = \gamma y_3^2 B \left(\frac{\Delta y}{y_3} + \frac{1}{2}\left[\frac{\Delta y}{y_3}\right]^2 \right) \tag{2.19}$$

where $\bar{p} = \gamma y/2$ and γ = specific weight. The boundary shear stress at any cross section is

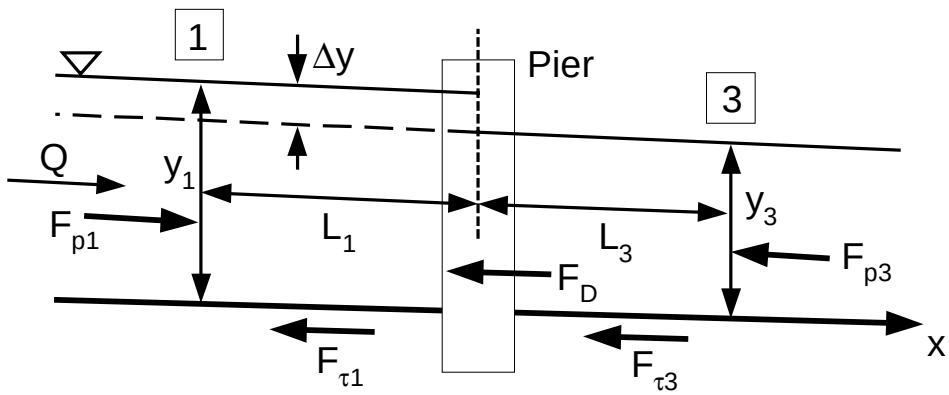

Figure 2.5: Forces for idealized flow conditions

$$\tau_0 = \frac{f}{8}\rho V^2 \tag{2.20}$$

where f = Darcy-Weisbach friction factor. The relationship between f and Manning's n is

$$f = \frac{8g}{R_H^{1/3}}\left(\frac{n}{\phi}\right)^2 \tag{2.21}$$

where ϕ = 1 for SI units and 1.486 for English units, R_H = hydraulic radius and g = acceleration of gravity. The total shear force, using Equation 2.20, is

$$F_\tau = F_{\tau 1} + F_{\tau 3} = (\tau_0 PL)_1 + (\tau_0 PL)_3 = \frac{f}{8}\rho\left(V^2(B+2y)L\right)_1 + \left(V^2(B+2y)L\right)_3$$

or

$$F_\tau = \frac{f}{8}\rho V_3^2 BL\Phi_\tau \tag{2.22}$$

where P = wetted perimeter = B + 2y, L = L_1 + L_3, and

$$\Phi_\tau = \left[\left(\frac{1}{1+\Delta y/y_3}\right)^2\left\{1+2\frac{y_3}{B}\left(1+\frac{\Delta y}{y_3}\right)\right\}\frac{L_1}{L} + \left\{1+2\frac{y_3}{B}\right\}\frac{L_3}{L}\right] \tag{2.23}$$

Assuming that A (flow area) is constant along each L, the total x-component of the weight is

$$W_x = W_{x1} + W_{x3} = (\gamma ALS_0)_1 + (\gamma ALS_0)_3 = \gamma y_3 BS_0 \left[\left(1 + \frac{\Delta y}{y_3} \right) L_1 + L_3 \right] \tag{2.24}$$

where S_0 = channel bed slope for the idealized representation (Figure 2.5). The momentum terms on the right-hand side of Equation 2.18 give

$$\rho Q(V_3 - V_1) = \rho V_3^2 y_3 B \left(\frac{\Delta y / y_3}{1 + \Delta y / y_3} \right) \tag{2.25}$$

In several of the preceding equations, the expressions Q = VBy and $y_1 = y_3 + \Delta y$ have been used.

Equations 2.18 through 2.25 can be combined to give the relationship between the drag force and the backwater as

$$F_D = \gamma y_3^2 B \left(\frac{\Delta y}{y_3} + \frac{1}{2} \left[\frac{\Delta y}{y_3} \right]^2 \right) - \frac{f}{8} \rho V_3^2 B \Phi_\tau$$

$$+ \gamma y_3 BS_0 \left[\left(1 + \frac{\Delta y}{y_3} \right) L_1 + L_3 \right] - \rho V_3^2 y_3 B \left(\frac{\Delta y / y_3}{1 + \Delta y / y_3} \right) \tag{2.26}$$

From Equations 2.14 and 2.26, the quantitative relationship between the drag coefficient and the backwater caused by a pier is

$$C_D = \frac{1}{\alpha Fr_3^2} \left(2 \frac{\Delta y}{y_3} + \left[\frac{\Delta y}{y_3} \right]^2 \right) - \frac{f}{16} \frac{L}{y_3} \frac{\Phi_\tau}{\alpha}$$

$$+ \frac{2}{\alpha Fr_3^2} \frac{L}{y_3} S_0 \left[\left(1 + \frac{\Delta y}{y_3} \right) \frac{L_1}{L} + \frac{L_3}{L} \right] - \frac{2}{\alpha} \left(\frac{\Delta y / y_3}{1 + \Delta y / y_3} \right) \tag{2.27}$$

Thus, an expression that gives the backwater due to a pier can also be used to obtain a drag coefficient. Care must be taken, however, in using Equation 2.27 to conclude what the dependence of C_D is on Fr. Fr appears explicitly in the denominator of each term in Equation

2.27, but Δy also depends on Fr (Equation 2.2). For a horizontal channel ($S_0 = 0$) with a short distance between the two cross sections so that the friction force is negligible, Equation 2.27 becomes

$$C_D = \frac{1}{\alpha Fr_3^2}\left(2\frac{\Delta y}{y_3} + \left[\frac{\Delta y}{y_3}\right]^2\right) - \frac{2}{\alpha}\left(\frac{\Delta y/y_3}{1+\Delta y/y_3}\right) \tag{2.28}$$

2.6. PHYSICAL MODEL STUDIES

Small-scale physical models can be used to study flow phenomena under controlled laboratory conditions. There are well-established modeling laws or relationships between quantities in the model and in the prototype. These modeling laws are derived from dimensional analysis and provide a means for determining the values that should be used in a model (e.g., the velocity or flow depth) to correctly represent the corresponding quantities in the prototype. The modeling laws also provide for scaling quantities measured in a model (e.g., head loss, drag force, or water surface profile) to prototype conditions.

Proper physical modeling starts by operating the model so that certain dimensionless parameters are the same in the model and the prototype. The parameters that must be equal in model and prototype are chosen to represent the physical parameters that are most important in the flows being modeled. The two most common dimensionless parameters for flow under bridges are the Reynolds number and the Froude number. In general, a Reynolds number (Re) is defined by

$$Re = \frac{VL}{\nu} \tag{2.29}$$

where V = a representative velocity, L = a characteristic length, and ν = kinematic viscosity. Reynolds number modeling, i.e., having $Re_m = Re_p$ where sub-m means model and sub-p means prototype, is used when the effects of viscous flow resistance are important in the flow. The Froude number (Fr) is defined by

$$Fr = \frac{V}{\sqrt{gy}} \tag{2.30}$$

where g = acceleration of gravity. Froude modeling ($Fr_m = Fr_p$) is used when gravitational forces are important. Another way of expressing $Fr_m = Fr_p$ is $Fr_r = 1$, where sub-r indicates the ratio of model to prototype values. From $Fr_r = 1$, we get

$$V_r = \sqrt{L_r} \tag{2.31}$$

where L_r is the model length scale ratio. Thus a model which is 10 times smaller than the prototype will have $L_r = 1/10$ and $V_r = 1/3.16$ so that velocities in the model should be 3.16 times smaller than in the prototype. Since the flow rate (Q) is proportional to a velocity times an area (length squared),

$$Q_r = L_r^{5/2} \tag{2.32}$$

so a 1/10 scale model would have $Q_r = 1/316$.

Models of open channel flows are frequently operated according to Froude model laws since gravity is usually important for these flows. However, for problems such as the one being addressed in this research, it is desirable to represent both gravitational and viscous effects in the model. The gravitational effects are important to correctly represent the force causing the flow and the behavior of the standing waves created by the piers; these waves include the effects that generate the backwater due to the piers. Viscous resistance is important for circular piers or piers with other shapes for which the geometry does not control the separation point. It is this resistance on the piers that causes the backwater effects, which are propagated by gravity. However, when both flow resistance and gravitational effects must be represented in a model, a difficulty arises since it is impossible to do simultaneous Reynolds and Froude modeling when water is the fluid in the prototype. The reason can be seen as follows. The Reynolds number ratio between model and prototype is

$$Re_r = \frac{V_r L_r}{\nu_r} \tag{2.33}$$

Substitution of Equation 2.31 for Froude modeling into Equation 2.33 shows that it would be necessary to have

$$\nu_r = L_r^{3/2} \tag{2.34}$$

in order to achieve both $Re_r = 1$ and $Fr_r = 1$. The implication of Equation 2.34 is that the viscosity of the model fluid would have to be much less than for the prototype if both $Fr_r = 1$ and $Re_r = 1$. There are no commonly available liquids that have a viscosity low enough to satisfy Equation 2.34. Thus, because of the fluid properties of water and other common fluids, it is impossible to operate a model to satisfy both $Re_m = Re_p$ and $Fr_m = Fr_p$.

In Froude models where it is necessary to represent resistance effects but where it is not possible to achieve $Re_m = Re_p$, one alternative approach is to use relationships to demonstrate that it is sufficient if $(C_D)_m = (C_D)_p$, even if $Re_m \neq Re_p$. However, achieving equal model and prototype drag coefficients is difficult for some bridge piers. For a circular prototype pier with a diameter of 3.28 ft (1 m) in a flow with a velocity of 6.6 ft/s (2 m/s), $(Re_{pier})_p = 2x10^6$, so that prototypes piers normally will be well into the range of turbulent boundary layers and lower drag coefficients (Figure 2.6). However, for Froude models with the same fluid in the model and the prototype where $\nu_r = 1$, use of Equation 2.29 gives

$$Re_r = \frac{V_r L_r}{\nu_r} = L_r^{3/2} \tag{2.35}$$

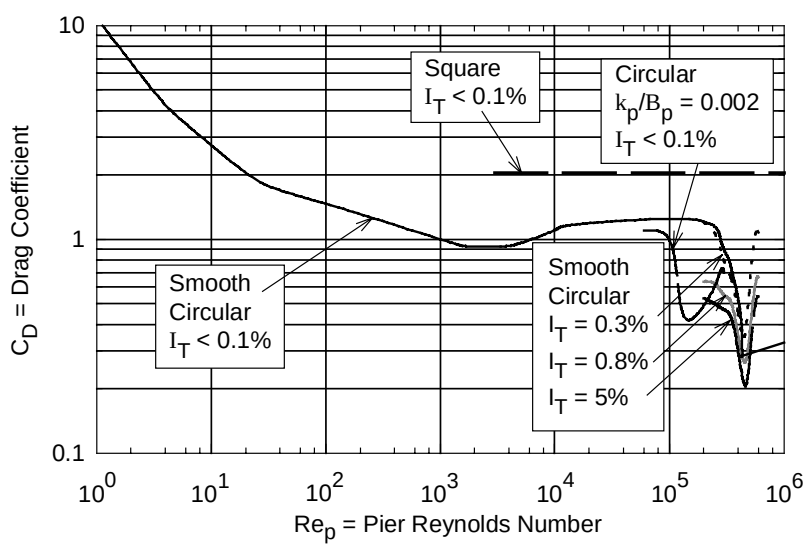

Figure 2.6: Drag coefficients for cylinders without free surface effects

Thus, a 1/10 scale model would have $Re_r = 1/31.6$ or $(Re_{pier})_m = 6.3x10^4$. For this lower model Reynolds number, the drag coefficient may be on the order of three to four times larger than for the prototype. This difference in C_D values can translate into corresponding differences in Δy. These differences are sometimes called scale effects. It is necessary to use extreme care in planning and conducting physical model tests to eliminate or minimize scale effects, since the scale effects can lead to erroneous conclusions from models. For these tests, it probably will not be possible to totally eliminate scale effects, but the modeling procedures can provide for minimizing and evaluating the scale effects so that the model results can be properly interpreted. Also, as implied by Figure 2.6, these scale effects are not present for square piers (or for any type of pier with essentially sharp corners that determine the separation point) since C_D values for such piers are independent of the Reynolds numbers for the range of values encompassing both model and prototype conditions (as long as the model is large enough). However, square piers have larger drag coefficients and larger Δy values, so they normally should not be used.

2.7. ACCOUNTING FOR BACKWATER USING MANNING'S EQUATION

One approximate approach that has been used to account for backwater caused by bridge piers is to increase the value of Manning's n for the channel reach containing the bridge. There is no physical basis for this approximation other than that both bridge piers and larger n values cause higher water levels upstream of bridges. Nevertheless, it is sometimes of interest to quantify the change in Manning's n value that would be necessary to give the same backwater as calculated using common backwater equations, such as Yarnell's Equation 2.2, which is

$$\Delta y = K\, y \left(K + 5Fr_3^{\,2} - 0.6\right)\left(\alpha + 15\alpha^4\right) Fr_3^{\,2} \tag{2.36}$$

Manning's equation may be written (where $\phi = 1$ for metric units and 1.486 for English units).

$$h_f(n) = \frac{v^2\, n^2}{\phi^2 y^{4/3}} L \tag{2.37}$$

In Equation 2.37 the notation $h_f(n)$ designates the head loss through the reach of length L with a Manning's coefficient n, the slope of the energy grade line (friction slope) is $S_f = h_f/L$, and

for a wide channel, the hydraulic radius is $R_h = y$. If n is increased to $n + \Delta n$, the head loss becomes $h_f(n+\Delta n)$, and the resulting change in water elevation is

$$\Delta y \approx h_f(n+\Delta n) - h_f(n) = \frac{v^2 L}{\phi^2 y^{4/3}}\left[(n+\Delta n)^2 - n^2\right] = \frac{g\,L}{\phi^2 y^{1/3}}\left(\Delta n^2 + 2\,n\,\Delta n\right) Fr^2 \quad (2.38)$$

if it is assumed that the Froude number is low enough that $\Delta h_f \approx \Delta y$. Equating Δy in Equations 2.36 and 2.38 and solving for Δn gives after some simplification

$$\frac{\Delta n}{n} = \sqrt{1 + \frac{\phi^2 K\, y_3^{\,4/3}}{g\,L\,n^2}\left(K + 5Fr_3^{\,2} - 0.6\right)\left(\alpha + 15\alpha^4\right)} \;-1 \quad (2.39)$$

For example, at a channel reach (n = 0.035) of length L = 150 ft (45.7 m) with two in-line bridge piers (α = 0.05 and K = 1.05), Figure 2.7 gives $\Delta n/n$ for various downstream Froude numbers and depths. For the conditions in the figure, the increased n-value that allows use of Manning's equation to account for both the friction losses and backwater caused by the bridge piers varies from 2% to 106%. For other flow conditions (i.e., other values of n, L, and α), the relative change in n would be different. Because of the large amount of variation of Δn and all of the variables on which it depends, the effort involved in determining the appropriate Δn is at least as much and possibly more than that needed to calculate $\Delta y/y$.

Note that channel contraction and expansion losses also have to be added since either Δn or Δy accounts for only the effects of the piers.

2.8. HIGH COST OF REGULATIONS

An important aspect of backwater effects is related to the cost of bridge construction. A paper presented by Wood, Palmer, and Petroff (1997) evaluated the implications of zero flood rise regulations - those that require the increase in backwater for a given flood to be less than 0.3 cm (0.01 ft) - for bridge builders in King County, Washington. From a design point of view, the effect of the zero-rise restriction varies depending on the bridge location and configuration. However, in all cases, complications and significant changes are added to the design in order to satisfy the ordinance. Moreover, specific examples showed that the cost of bridge construction increases significantly due to the zero-rise criterion. The average cost increase was found to be around 40%. Wood *et al.*'s paper suggests that a zero-risk

paradigm is unworkable, and that moving towards feasibility-based or technology-based standards that balance costs and benefits is more realistic.

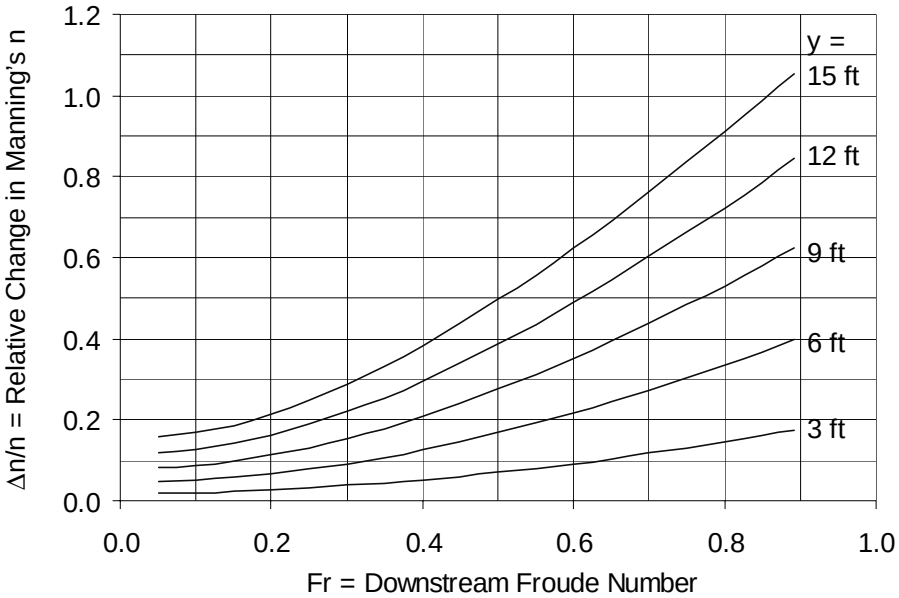

Figure 2.7: Increase in Manning's n to account for bridge piers when n = 0.035, L = 150 ft (45.7 m), and α = 0.05.

CHAPTER 3. EQUIPMENT

3.1. INTRODUCTION

Two types of experiments with different objectives were performed. The first type was to measure the drag forces on piers, while the second quantified the rise in water level upstream of bridge piers, i.e., the backwater. These experiments were undertaken by two different research groups.

This chapter describes the physical model and associated equipment (Figure 3.1). A geometric description of the channel in which all the experiments were undertaken is provided in Section 3.2. The pump installations are described in Section 3.3. The different pier shapes modeled during the research period are presented in Section 3.4. Flow rate and water level measurement procedures are respectively described in Sections 3.5 and 3.6. The equipment described in Section 3.7 was used to determine the magnitude of the drag force F_D along with important parameters for the first set of experiments.

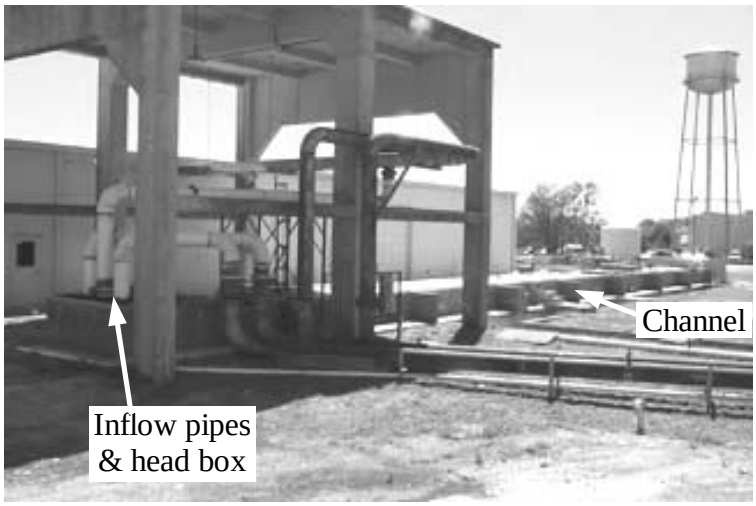

Figure 3.1: Overview of the physical model showing the channel and the pipes that supply the flow

3.2. THE CHANNEL

A rectangular channel (Figure 3.2) was constructed for the experimental part of this research. The channel is 5 ft (1.52 m) wide, 2.6 ft (0.81 m) deep, and 110 ft (33.5 m) long.

This length was needed to provide adequate distance upstream of the model piers for flow establishment and adequate distance downstream of the model piers so that the flow at the piers would not be affected by the depth control (tailgate) at the downstream end of the channel. The channel was built outdoors with approximately the downstream two-thirds on an existing concrete slab, which was extended for the upstream part of the channel. The bed is approximately horizontal. The lowest bed elevation in the channel was taken as the datum for elevation measurements. As shown in Figure 3.2, the whole channel was covered with corrugated fiberglass sheets to minimize wind effects. At the downstream end of the channel, a tailgate was installed to allow easy modification of the water level by changing the gate opening (Figure 3.3).

Figure 3.2: Photograph of the channel and a 3.5 in. (8.9 cm) diameter model pier

3.3. PUMPS

Four vertical turbine pumps provided the flow. The North and South pumps (Figure 3.4) were outdoors and the two Inside pumps (Figure 3.5) were in the laboratory adjacent to the channel. The maximum flow into the channel is approximately 24 ft^3/s (0.68 m^3/s). The flow from each of the North and South pumps was fed through separate 14 in. (35.6 cm) pipes that contracted to 12 in. (30.5 cm) near the channel. The maximum flow rate from each of those pumps is 10.5 ft^3/s (0.30 m^3/s). The flows from the two Inside pumps were combined

and fed through a 12 in. (30.5 cm) pipe. Their combined flow rate is 3 ft^3/s (0.08 m^3/s). Control valves are present on all the pipes.

Figure 3.3: Tailgate located at the downstream end of the channel to regulate the water level

Figure 3.4: North (right) and South (left) pumps as installed on the reservoir

Figure 3.5: Photograph of the Inside pumps

3.4. PIERS

PVC and Plexiglas pipes were used respectively to model the bridge piers for the backwater and for the drag coefficient experiments. Before the end of the drag coefficient experiments, it was decided to roughen these pipes by cementing medium-size sand over their exterior surface in an attempt to move the separation point to decrease the size of the wake and the pressure drag as would exist for larger Re.

For the drag force experiments, only two experiments from a total of 15 were done using a 3.5 in. (8.9 cm) diameter pipe roughened by cementing medium-size sand on the exterior surface, three were performed with a pipe roughened by fixing sandpaper on the exterior surface, while the others were performed with a smooth 3.5 in. (8.9 cm) diameter pipe. The decision to roughen the pipes was made during the experimental period and caused this heterogeneous set of conditions.

In the second part of the research, which studied the backwater effect of bridge piers, the pier configurations were as follow:

- 3.5 in. (8.9 cm) diameter (Figure 3.6).
- 6.5 in. (16.5 cm) diameter (Figure 3.6).
- Rectangular pier with semicircular nose and rectangular tail (diameter of the nose equal to 6.5 in. (16.5 cm) and length of the rectangle equal to 3 ft (91.4 cm)) (Figure 3.7).
- Two 6.5 in. (8.9 cm) diameter piers mounted one behind the other.

All of the circular piers were roughened. The rectangular pier was not roughened.

Figure 3.6: Photograph showing the roughened piers: two 6.5 in. (16.5 cm) piers and one 3.5 in. (8.9 cm) pier

3.5. FLOW RATE

Accurately determining the flow was an integral part of the experiments since its value would be used to compute the flow velocity and the Froude number. Three techniques, namely propeller-type flow meters, a Venturi meter, and a thin-plate weir, were utilized to measure the flow rate. A description of this equipment is presented in the following sections.

3.5.1. Flow Meters

Three Data Industrial propeller-type flow meters (series 1500) measured the flow rates in the three pipes coming to the channel. The first measured the flow coming from the North

pump, the second measured the flow coming from the South pump, and the third measures the flow in the pipe carrying the combined flow from the two Inside pumps. Figure 3.5 illustrates the two Inside pumps, while Figure 3.8 shows the reducers and the two 12 in. (30.5 cm) pipes from the two outside pumps. Figure 3.9 shows the installation of the Data Industrial flow meter for the Inside pumps. Figure 3.10 shows the display panels for the flow measurement devices. These flow meters allowed the flow rate to be computed by dividing the volume of water by the time recorded using a stopwatch.

Figure 3.7: Rectangular pier with semi-circular nose and rectangular tail (not roughened)

These flow meters were used in the first set of experiments involving the drag forces computation, while in the case of determining the water level variation, a Venturi meter and a thin-plate weir were occasionally used along with these flow meters.

3.5.2. Venturi Meter

The flow from the North pump could be routed inside the laboratory building, through a Venturi meter, and then back to the channel. This pump was able to produce all but the highest flow rates required during the model studies. The standard equation for discharge through a Venturi meter (Streeter and Wylie, 1985) is

Figure 3.8: Conduits of the outside pumps (north to the right of the picture)

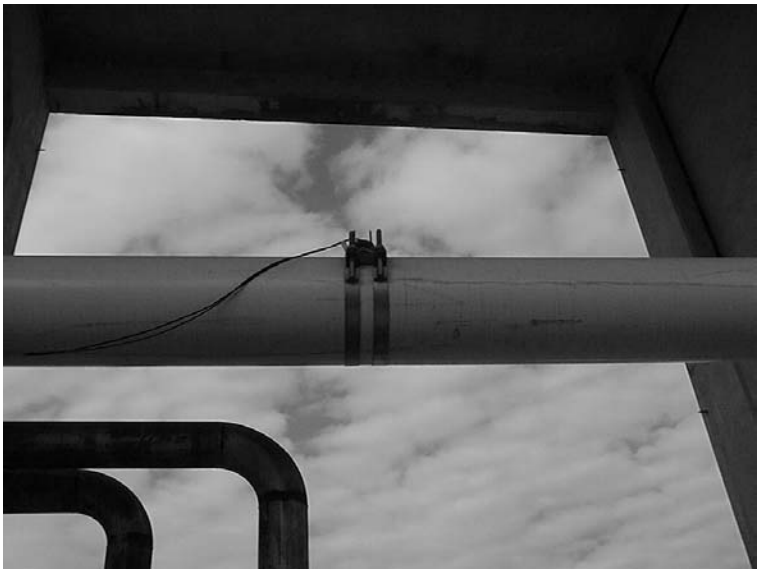

Figure 3.9: Propeller installation of the Data Industrial flow meter for the Inside pumps

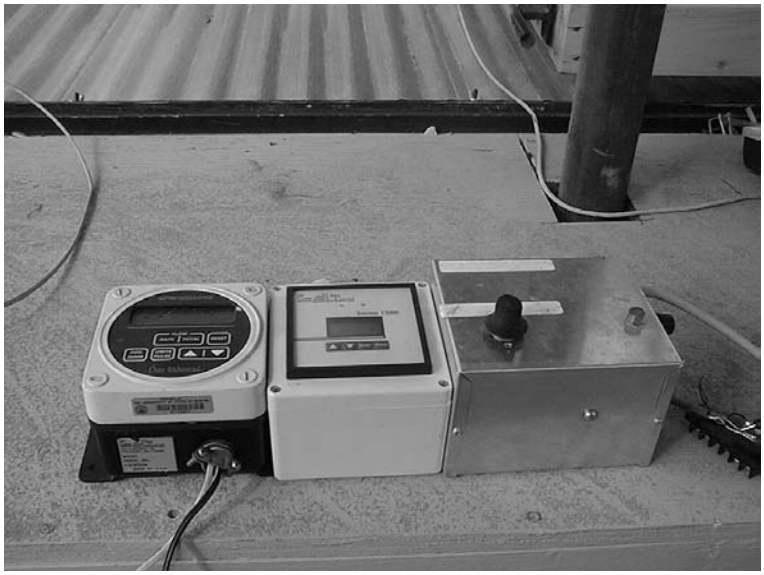

Figure 3.10: Display panels for the flow measurement devices

$$Q = \frac{C_d A_2 \sqrt{2g\Delta h}}{\sqrt{1 - \left(\frac{A_2}{A_1}\right)^2}} \tag{3.1}$$

where Q = discharge, C_d = discharge coefficient, A_1 = area of approach pipe, A_2 = area of Venturi meter throat, Δh = difference in piezometric head between the entrance and the throat of the Venturi meter, and g = acceleration of gravity. For a given Venturi meter, A_1 and A_2 are constants. For a well-made Venturi meter, the discharge coefficient will be constant for throat Reynolds numbers above $2x10^5$ (Streeter and Wylie, 1985), where the pipe Reynolds number (Re) is defined as

$$Re = \frac{VD}{\upsilon} \tag{3.2}$$

where V = mean flow velocity, D = diameter, and υ = kinematic viscosity. Since D and υ are constant (except for small changes in υ due to the temperature changes), the discharge coefficient should be constant for all velocities greater than a certain value, or equivalently, for all discharges greater than a certain value.

The Venturi meter had an approach diameter of 12 in. (30.5 cm) and a throat diameter of 6 in. (15.2 cm). For a Venturi meter of this size, the discharge coefficient should be constant for throat velocities greater than 5 ft/s (1.5 m/s) in the throat or equivalently for 1.25 ft/s (0.38 m/s) in the 12 in. (30.5 cm) approach pipe. The corresponding discharge is 1.0 ft^3/s (0.028 m^3/s). Accordingly, Equation 3.1 can be simplified to

$$Q = K\,\Delta h^{0.5} \tag{3.3}$$

where

$$K = C_d A_2 \sqrt{\frac{2g}{\left[1-\left(\frac{A_2}{A_1}\right)^2\right]}} \tag{3.4}$$

K should be constant for discharges greater than 1 ft^3/s (0.028 m^3/s).

In a previous project, the Venturi meter was calibrated using part of the return floor channel as a volumetric tank. The available volume for calibration was 2060 ft^3 (58.4 m^3). The piezometric head difference (Δh) was measured with either or both an air-water manometer and a water-mercury manometer. Both manometers were connected to the Venturi meter at all times. Because the specific gravity of water is much less than that of mercury, the air-water manometer is more accurate for measuring small flow rates than the mercury-water manometer. However, the capacity of the air-water manometer was not high enough to measure the flow rates above 1.52 ft^3/s (0.043 m^3/s); thus the mercury-water manometer was used (Figure 3.11).

The data obtained from the Venturi meter calibration tests did not give an acceptable fit in the form of Equation 3.3. The best fit was found to be:

$$Q = 0.0686\,\Delta h^{0.53} \tag{3.5}$$

The least-squares correlation coefficient (R^2) of the line was 0.998, with a standard deviation error of 0.083 ft^3/s (0.0024 m^3/s). Even though the implication of Equation 3.5 is that K changes slightly, this calibration continually proved to be reliable and accurate throughout the course of the project. Hence, Equation 3.5 was used in computing the North pump flow rate from the Venturi meter measurements.

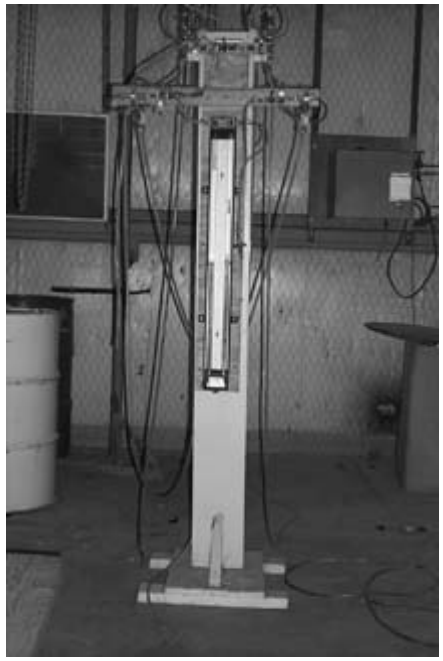

Figure 3.11: The mercury-water manometer for the Venturi meter

3.5.3. Thin-Plate Weir

As noted previously, the Venturi meter was able to measure flow from the North pump only. When higher flow rates were required and the two outside pumps (North and South) were used, the flow was measured either by the flow meters (section 3.5.1) or by a rectangular-notch thin-plate weir placed outdoors in the return channel to the outside reservoir. Occasionally, both methods were used in order to compare the results. The weir is constructed of wood and erected perpendicular to the flow with a thin-plate crest. The upstream face of the weir plate is smooth, and the plate is vertical. The sharp-crested design caused the nappe to spring free, as seen in Figure 3.12, for all but the very lowest heads. The approach channel was long enough (Figure 3.13) to produce a normal velocity distribution and ensure a wave-free water surface. The weir flow was computed from (Bos, 1989)

$$Q = C_e \frac{2}{3}\sqrt{2g}\, b_e h_e^{3/2} \tag{3.6}$$

Figure 3.12: Thin-plate weir used for flow measurement

Figure 3.13: Water flowing in the direction of the weir. The point gage and stilling well are shown on the right of the picture

where $b_e = (b_c + 0.010)$ ft = $(b_c + 0.003)$ m, b_c = width of weir crest = 4.688 ft (1.429 m), $h_e = (h_1 + 0.003)$ ft = $(h_1 + 0.001)$ m, h_1 = measured head, and C_e = discharge coefficient. C_e depends on b_c/B_1, where B_1 = channel width = 5.02 ft (1.53 m) so that $b_c/B_1 = 0.934$.

Interpolating between $(0.602+0.075h_1/p_1)$ for $b_c/B_1 = 1$, where p_1 = weir height, and $(0.599+0.064h_1/p_1)$ for $b_c/B_1 = 0.9$ gives

$$C_e = 0.600 + 0.068 \frac{h_1}{p_1} \tag{3.7}$$

3.6. WATER LEVEL

The experiments required accurate measurement of small changes in water level. For this purpose, the static ports on Pitot tubes were connected to an inclined manometer board via flexible plastic tubing. The inclined manometer board enabled precise measurement of the water levels. The slope of the manometer board was one to five, meaning that the vertical readings were amplified five times. Thus,

$$H_R = \frac{H_A}{5} \tag{3.8}$$

where H_R = the vertical position of the water surface and H_A = the reading from the inclined manometer board. Each of the tubes on the manometer board (Figure 3.16) was 4.3 ft (1.31 m) long.

Twenty-four Pitot tubes were set up in ten cross sections of the channel, on both sides or in the middle of the channel and both upstream and downstream of the piers, as illustrated in Figure 3.14. Figure 3.15 presents a sketch of a Pitot tube. Only the static ports are used.

Since measurement of the water level was needed for both the drag coefficient tests and for determination of the water level, the manometer board was used in both cases.

3.7. DRAG FORCE EQUIPMENT

3.7.1. Mechanical Components

3.7.1.1. Model Pier

In the first part of the research for the measurement of drag forces, the model pier consisted of three families of components, the plastic pier, the top and the bottom supporting

strips, and the calibration device. Figure 3.17 shows the pier installed in the channel and Figure 3.18 gives the components of the model pier.

The plastic pier was 3 ft (91.4 cm) tall with an inside diameter of 2.75 in. (7.0 cm) and an outside diameter of 3.25 in. (8.26 cm). The two aluminum support strips were identical.

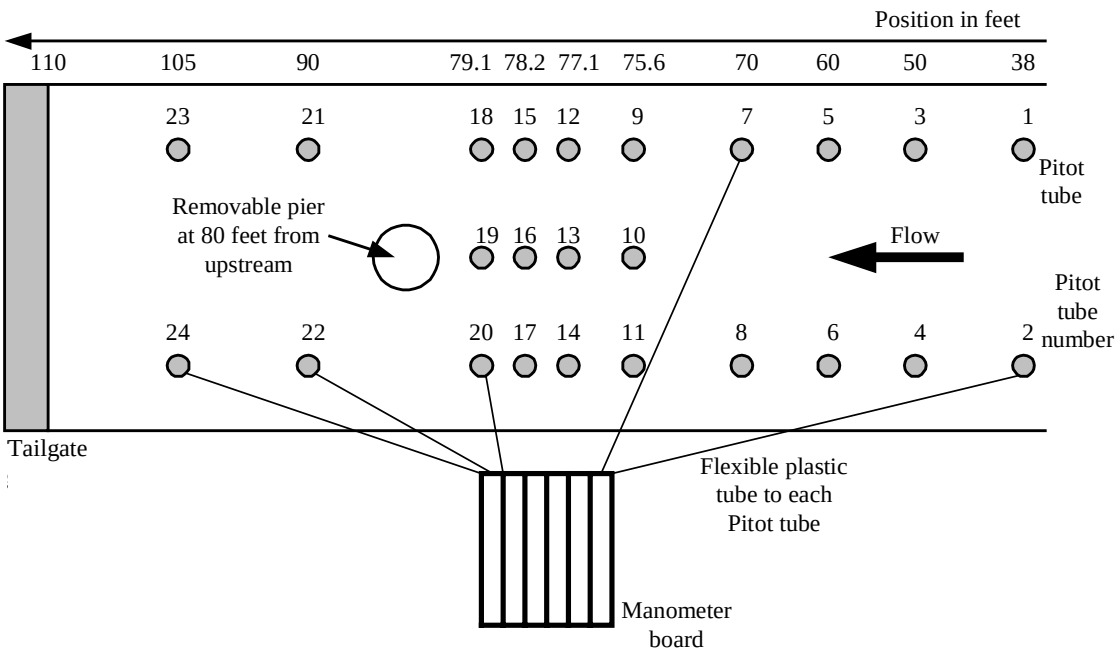

Figure 3.14: Sketch of the physical model showing the location and the index number for each Pitot tube

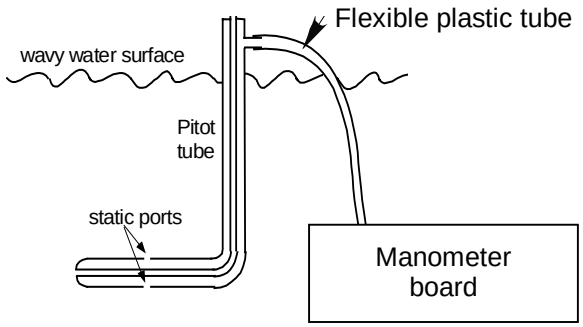

Figure 3.15: Sketch of the water level measurement system

Figure 3.16: Manometer board having twenty-four tubes and a slope of 1/5

Figure 3.17: Pier installed in the channel

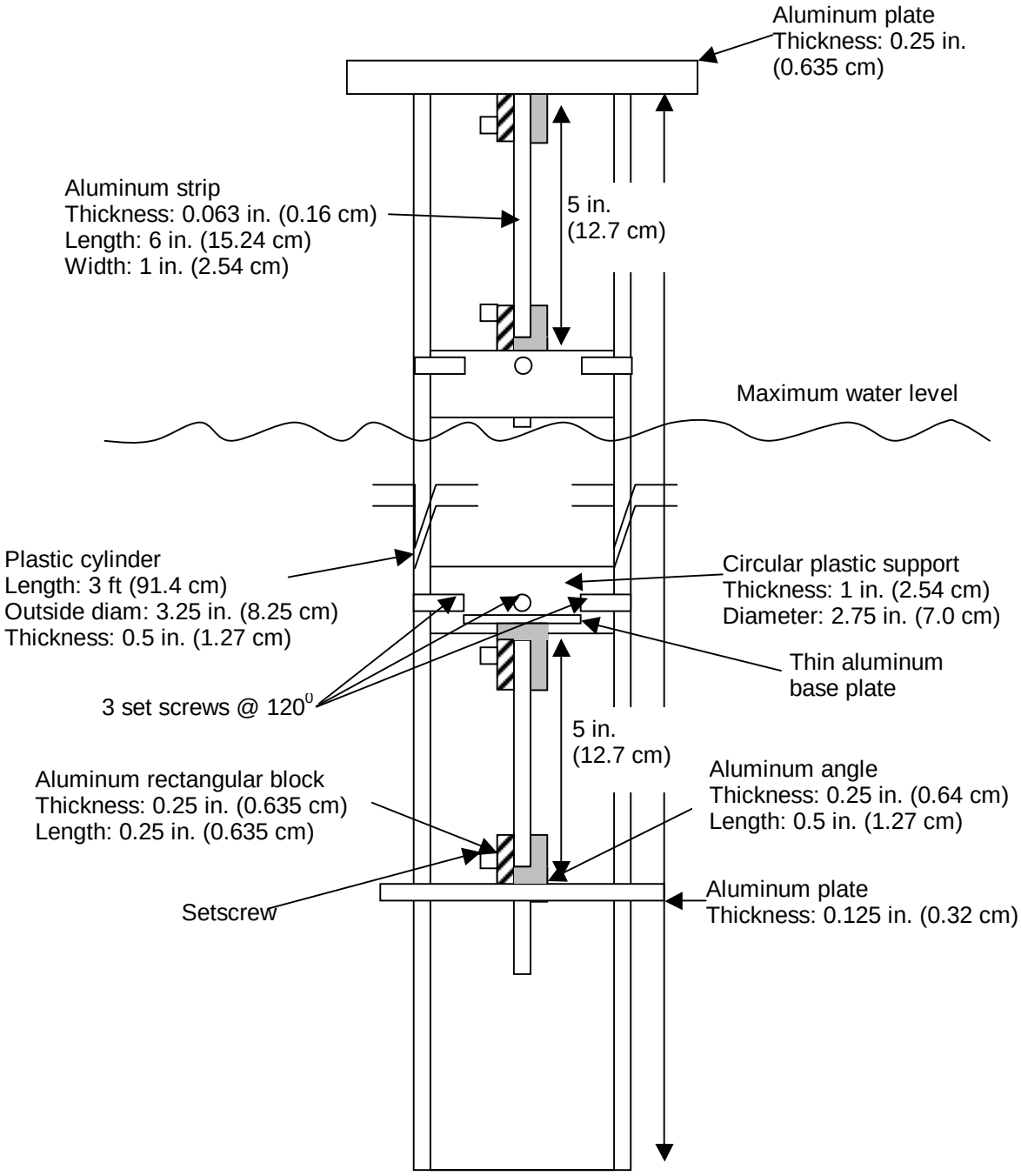

Figure 3.18: Pier model components

The length of each strip was 6 in. (15.24 cm), the width was 1 in. (2.54 cm) and the thickness was 0.063 in. (0.16 cm). Two screw holes were made one each end of the strips in order to fix them to their supports. Figure 3.19 shows a side and an end view of an aluminum strip.

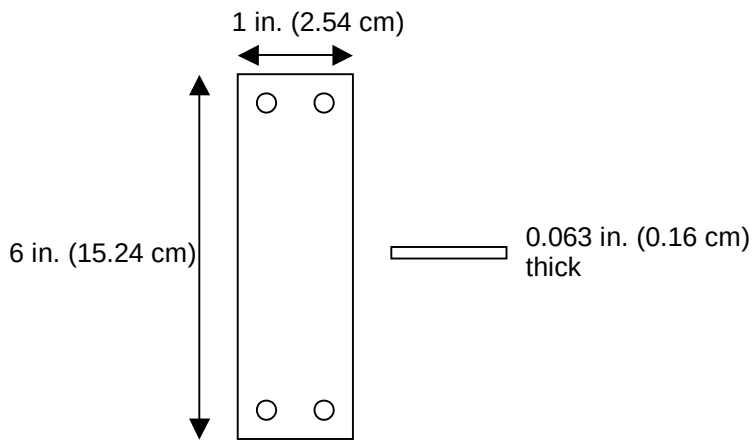

Figure 3.19: Aluminum strip

During the measurements, the pier model vibrated due to vortex shedding. The vibration was minimized by choosing stiff strips. On the other hand, the strain decreased when the moment of inertia of the section was increased. Section 3.7.2.1 discusses this theory in detail. For the purpose of obtaining the highest moment of inertia with acceptable strains during the experiments, the dimensions of the aluminum strips had to be chosen taking into consideration the two previous statements. For this purpose, the Structural Analysis Program SAP 2000 (Anon., 1997) model of the pier was created for the piers and its supports. A force approximately equal to the highest drag force expected was applied to the middle of the model. Afterwards different iterations were performed by changing the dimensions of the strips, and calculating the deflections and the moments. Finally, the dimensions were chosen in order to have the maximum moments of inertia with acceptable deflections. Section 3.7.1.2 gives more details about the SAP 2000 model.

3.7.1.2. Other Model Components

One of the challenges was to transfer the force applied on the pier to the strips in such a manner that the connection conditions would be known and could be analyzed. In order to

do that, a circular disk (Figure 3.20) was attached to each strip. The disks were designed to go inside the plastic cylinder where they could be fixed using three setscrews. Hence, the strips were rigidly attached to the cylinder, allowing the transfer of the moments and the forces from the cylinder to the strips. Figure 3.20, Figure 3.21, and Figure 3.22 give an overview of the supports.

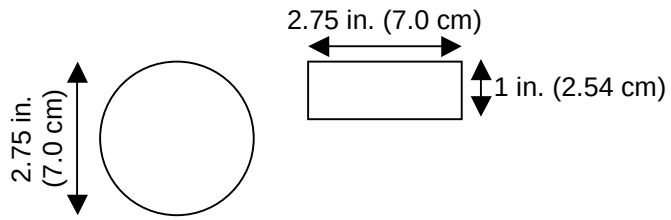

Figure 3.20: Sketch of the circular support

Figure 3.21: Circular support

For this pier model the maximum strain is obtained for the highest moment. The highest moment was obtained if the supports were fixed. The bottom strip was fixed to the bottom of the channel using a bolt. The top strip was fixed with C clamps to an aluminum beam

crossing over the channel transversely. Figure 3.23 and Figure 3.24 show respectively the fixing devices for the top and the bottom.

Figure 3.22: Circular support when connected to the model pier

Figure 3.23: Fixing device for the top

The final component was a mechanical device that permitted the application of a known concentrated force at chosen points on the cylinder. Figure 3.25 gives a sketch of the

device and Figure 3.26 shows a photograph of the device. The supports of the calibration device were designed in a way to allow the device to rotate freely. Hence, no moments were taken by the supports. Figure 3.27 shows a support in detail.

Figure 3.24: Fixing device for the bottom

If a force F were applied at a distance X (Figure 3.25) equal to 12 in. (30.5 cm), the force transmitted to the cylinder is P = FX/Y. SAP 2000 was used to determine the distribution of the force on the two supports. A model identical to the pier was developed using SAP 2000. Figure 3.28 shows the SAP 2000 model in three dimensions and two dimensions with the different inputs. By applying a force equal to P and at the same location (Z from the bottom of the channel), the resulting reactions could be found (Figure 3.28).

In order to illustrate the use of the SAP 2000 model, Table 3.1 shows the inputs needed for the model including an example value for the force P. The table also shows the lengths between the supports for each component. Table 3.2 gives the corresponding results.

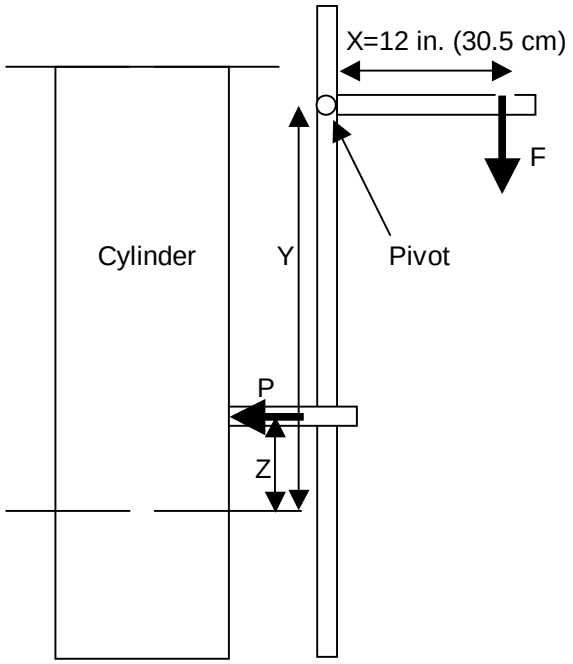

Figure 3.25: Sketch of the calibration device

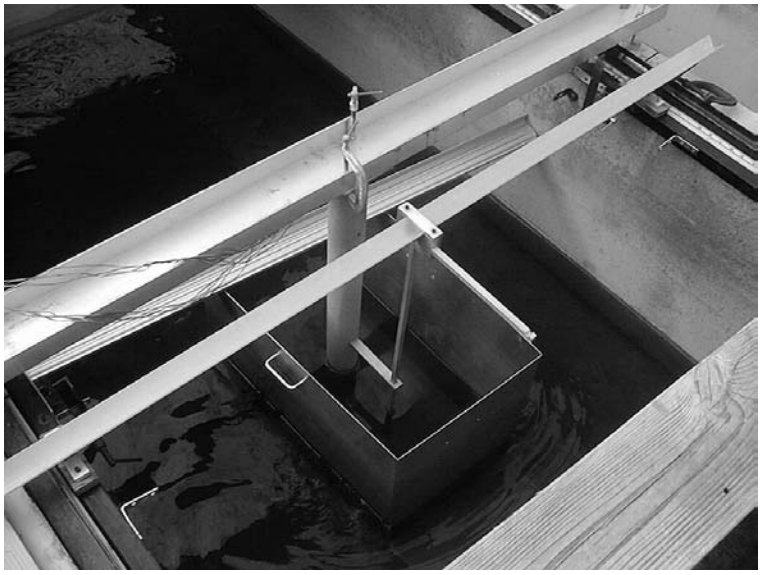

Figure 3.26: The calibration device

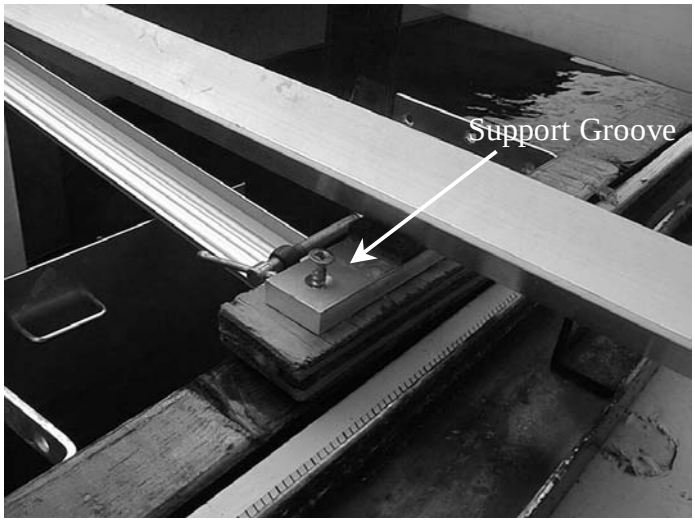

Figure 3.27: The calibration device support

Table 3.1: Input needed for the SAP 2000 model

	Bottom strip		**Plastic cylinder between supports**		**Top strip**	
	(in.)	**(mm)**	**(in.)**	**(cm)**	**(in.)**	**(mm)**
Length	5 in.	12.7 cm	20.75 in.	52.7 cm	5 in.	12.7 cm
Width or exterior diameter	1 in.	2.54 cm	3.5 in.	8.9 cm	1 in.	2.54 cm
Thickness	0.063 in.	0.16 cm	0.25 in.	0.635 cm	0.063 in.	0.16 cm
Force and point of application	-	-	2.25 lb_f @ 5.5 in. from node 2	10 N @ 13.97 cm from node 2	-	-

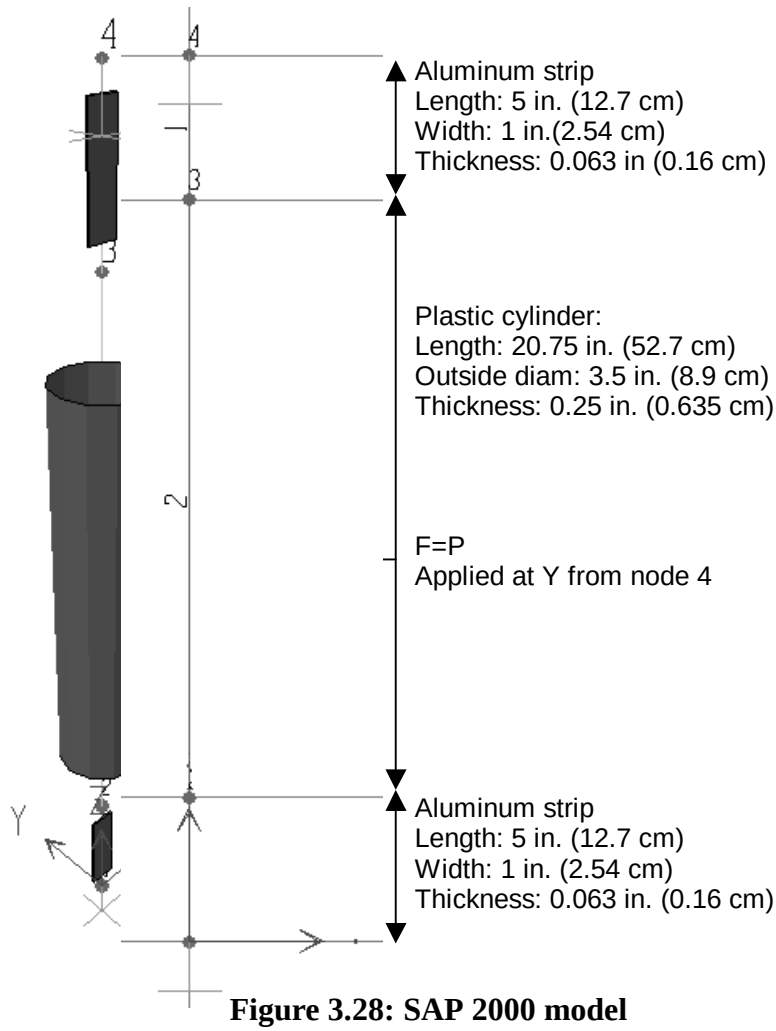

Figure 3.28: SAP 2000 model

Table 3.2: Results for the corresponding inputs

Joint number	Displacement (U_y)		Reaction (R_y)	
	(in.)	(mm)	(lb_f)	(N)
1	0	0	1.53	6.8
2	0.076	1.94	0	0
3	0.037	0.94	0	0
4	0	0	0.72	3.2

3.7.2. Electrical and Electronic Components

3.7.2.1. Strain Gages

Strain gages are variable resistances used to measure the strain in an element. They have to be part of an electrical circuit, which has to include an excitation voltage. For this research, a full Wheatstone bridge with four identical active gages (four variable resistances) was used. Figure 3.29 shows the details of the circuit where E is the input voltage (V), E_0 the output voltage (V) and $\mu\varepsilon$ the microstrain.

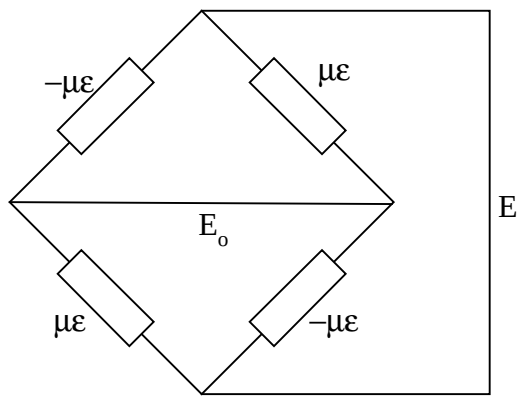

Figure 3.29: Strain gage circuit

When a certain amount of strain is applied to one or more strain gages, the output voltage (E_0) varies from its initial value. The difference between the initial and final values of E_0 corresponds to the strain. Ideally, if the Wheatstone bridge is initially balanced ($E_0 = 0$) then the second value of the voltage corresponds to the strain. Since the goal from the use of strain gages is to calculate the strain, an equation that relates microstrain and volts was used, namely

$$\frac{E_0}{E} = F\,\mu\varepsilon \tag{3.9}$$

where F is the dimensionless gage factor that depends on the strain gages and the instrument (F = 2 in this case) and $\mu\varepsilon$ the actual microstrain. For example if E = 10 V and E_0 = 1 V, knowing that F = 2 gives $\mu\varepsilon = 0.05$. Since the work was done in elastic conditions, Hooke's law states that $\sigma = \varepsilon \times Z$, where σ = stress, ε = strain, and Z = young's modulus. This

relationship means that the stress is proportional to E_0/E because of Equation 3.9. This conclusion is important for the calibration.

After developing the SAP 2000 model, a concentrated force equivalent to the highest expected drag force was applied at the midpoint of the model. The maximum stress generated in each of the strips was converted into strain, and the strain gages were chosen on this basis. The strain gages used for the research were CEA-13-125UW-120 option P2 with a resistance of 120 Ohms (±0.3%) and a gage factor (F) of 2 (± 0.5%), from the Measurements Group (http://www.measurementsgroup.com). Figure 3.30 gives a picture of the strain gages, and Table 3.3 shows their various dimensions.

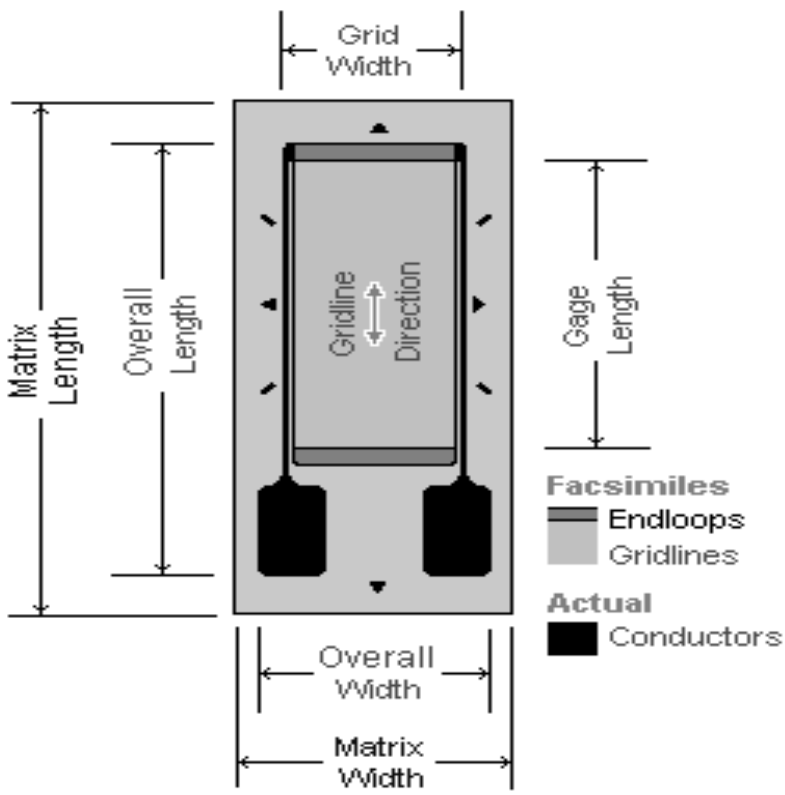

Figure 3.30: Detailed drawing of a strain gage (from the Measurements Group)

Table 3.3: Strain gage dimensions

	Dimensions	
	(in.)	**(mm)**
Gage Length	0.125	3.18
Overall Length	0.325	8.26
Grid Width	0.180	4.57
Overall Width	0.180	4.57
Matrix Length	0.42	10.7
Matrix Width	0.27	6.9

After choosing the strain gage type, the locations of the strain gages on the aluminum strips had to be selected to give the largest possible signals. As mentioned before, according to Hooke's law, $\sigma = \varepsilon Z$. The stress can be calculated using

$$\sigma = M\frac{K}{I} + \frac{N}{S} \tag{3.10}$$

where M is the bending moment, K is the distance to the neutral axis, I is the moment of inertia, N is the tension or compression and S is the section of the strip. The term N/S is a constant since the compression is coming from the weight of the model, which is constant. The section of the strip was rectangular and therefore constant. Equation 3.10 becomes

$$\sigma = M\frac{K}{I} + A_1 \tag{3.11}$$

where A_1 is equal to N/S. If the stress is eliminated using Hooke's law, the above equation can be written as

$$\varepsilon = \frac{M}{E}\frac{K}{I} + A_2 \tag{3.12}$$

where A_2 is equal to A_1/Z, which is a constant. Equation 3.12 shows that the strain reaches a maximum where the moment is the highest. In this case the moment is maximum at the supports. Thus, the four strain gages were placed as close as possible to the top and bottom of the strips, namely, 1 in. (2.54 cm) from each end (Figure 3.31).

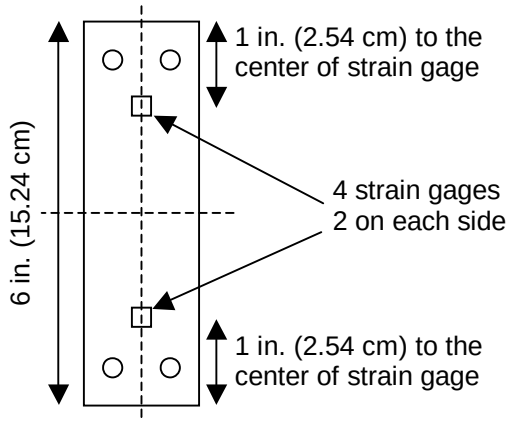

Figure 3.31: Strain gages location

The strain gages were fixed to the strips using the M-Bond AE-10 adhesive from the Measurements Group. As one can see in Figure 3.18, the bottom strip was under water. Therefore, the four strain gages on the bottom strip had to be waterproofed using M-Coat W-1 also from the Measurements Group.

3.7.2.2. Strain Gage Conditioner and Amplifier System

This equipment provided the excitation or input voltage (E) and amplified the output voltage (E_0). The model used for the research is the 2100 system, supplied by the Measurements Group. In addition this instrument allowed the user to balance the bridge within a range of ±6000 microstrain (με). The principal features of the system included:

- Independently variable and regulated excitation for each channel (0.5 to 12 Volts).
- Fully adjustable calibrated gain (amplification) from 1 to 2100.
- Bridge-completion components to accept quarter-, half-, and full-bridge inputs in each channel.
- LED null indicators on each channel, always active.

3.7.2.3. Two-Channel Digital Oscilloscope

The oscilloscope in these experiments was the TDS 200 Series from Tektronix. It was used to

- visualize the voltage variations due to the strain variations in the gages,
- capture and digitize the data, and
- transmit the data to a computer through a cable.

Table 3.4 gives its properties.

Table 3.4: TDS 210 oscilloscope specifications

Bandwidth	60 MHz
Channels	2
Max sample rate per channel	1 GS/s
Sweep speeds	5 ns/div-5 s/div
Vertical accuracy	3%
Record length	2.5k points/channel
Vertical sensitivity	10 mV/div-5 V/div at full bandwidth

3.7.2.4. Data Transfer Software

The Wavestar software from Tektronix was used to transfer the data from the oscilloscope to the computer. The user was then able to process it for different purposes. This program offers the feature of presenting the data in a graphical and tabular format.

3.7.3. Calibration Procedure

The objective of the calibration was to provide knowledge of the reactions at the top and bottom support by reading the voltage at the top and the bottom strips for known applied forces. To achieve this objective, the four strain gages on the top strip were connected to form a full bridge. The circuit was linked to channel 1 of the amplifier, which provided an input voltage of 10 Volts and permitted the reading of an output voltage that is amplified 100 times. The oscilloscope, which was linked to the output voltage, permitted the reading of the amplified signal. The same procedure was done for the bottom strip, using channel 2. A cable that linked the computer to the scope allowed the transfer of the data to the computer. Figure 3.32 shows the circuit.

The calibration was performed as follows. The model pier was set up. The bridge resistance was adjusted until the output voltage was minimized (ideally $E_0 = 0$). The zero reading was taken. Next a known force F was applied at a distance Y (Figure 3.25) using

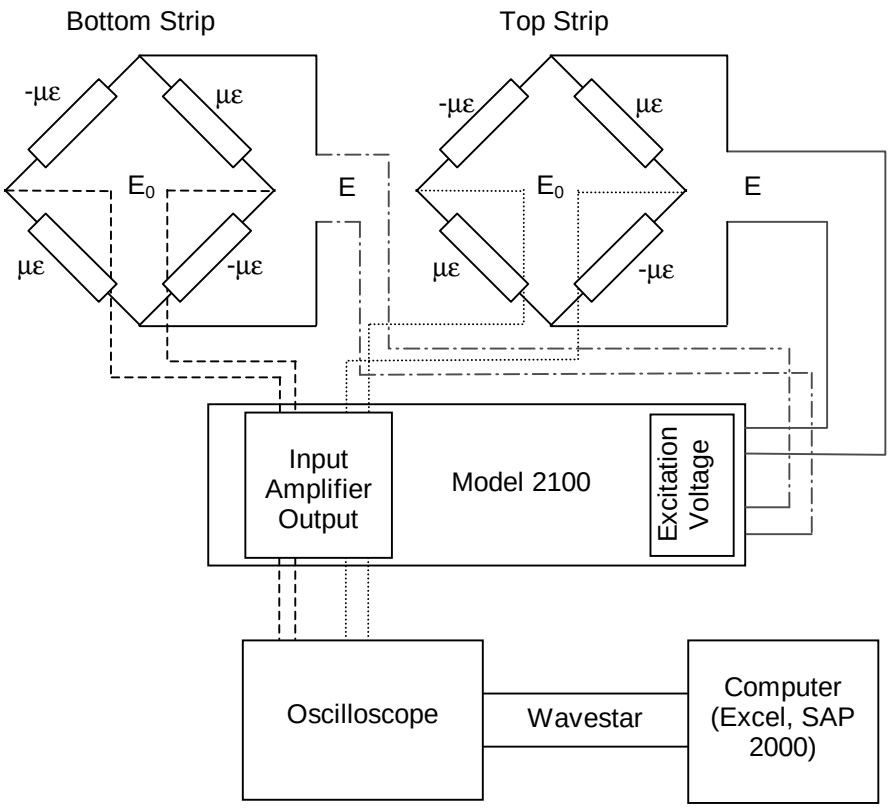

Figure 3.32: Electronic and electric equipment circuit

weights. The stresses generated in the strips caused the resistance of the strain gages to vary and consequently unbalanced the bridge. The new output voltage was acquired by the computer. The procedure was repeated for other weights. The result of each measurement was a specific voltage for each strip. For instance, if six different forces were applied, then each strip would have six data tables and therefore six average voltages over the 2.5 s measurement time. The last step in the calibration was to find the reactions distributed to the supports. The same forces applied during the calibration are used in the SAP 2000 software, allowing the calculations of the reactions. In this way, the relationship between voltage and forces was obtained. A graph showing the voltage (for each strip separately) in terms of force (Newtons) was plotted to get the calibration equation for the strip. Figure 3.33 shows a typical graph of volts vs. Newtons for the bottom strip. During the fitting of a straight line for calibration, the

best-fit equation was constrained to have a zero intercept because when no force was applied, there should be no voltage.

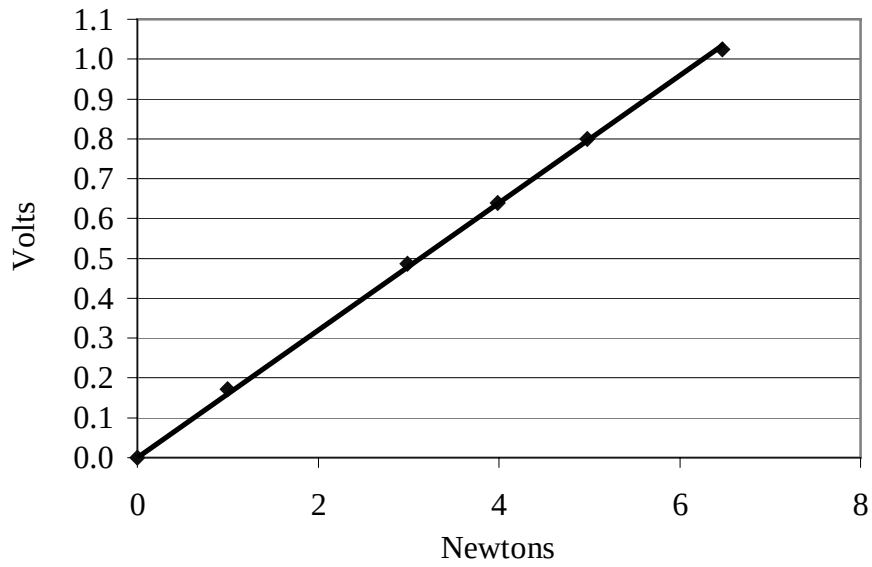

Figure 3.33: Calibration graph for the bottom strip

As mentioned previously, the bottom strain gages were submerged under water during the experiment. To have the same conditions during calibration and measurement, it was decided to perform the calibration in wet conditions. In order to do that, a minimum flow had to be created in the channel. The tailgate used to control the water level had leaks and could not be used to establish a stagnant pool of water. For this reason, the shield shown in Figure 3.34 was fabricated. When placed in front of the pier, this shield eliminated the drag force on the pier. The shield was held in place longitudinally by its weight. A horizontal aluminum bar prevented it from moving transversely. The force application device for the calibration was placed inside the shield. Figure 3.35 shows a photograph of the pier during calibration.

3.7.4. Calibration Results

A series of calibrations was performed. The results of the calibrations for both strips are summarized in Table 3.5, where the m values are for the equation V = mF with V = volt-

age and F = force. These results reinforce the linearity property since $R^2 = 0.999$ for the best-fit equations for most of the tests.

Figure 3.34: Stagnation shield

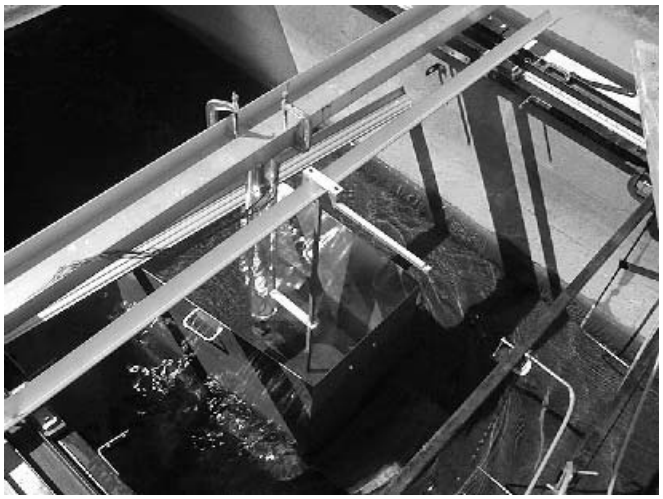

Figure 3.35: Pier during calibration process

In order to verify that the calibrations were independent of the location of the applied force, calibrations 1 and 3 were conducted the same day, but the force was applied at different locations. The same procedure was performed with calibrations 6 and 7 and calibrations 2 and 4. As one can see in Table 3.5, the results were almost identical. Even though the

properties stated previously were verified, the experimental conditions were affecting the behavior of the strain gages. For the same strip, the calibration curves varied from one day to another. Calibrations 1 and 5 were performed during different days by applying the force at the same location. The results were different by 9.5 % for the top strip and 3% for the bottom strip (Table 3.5). In order to show a better picture of the results, a graph showing the mean line for all of the calibrations was drawn. Figures 3.36 and 3.37 show the graph for the top and bottom strips.

Table 3.5: Slope m in V = mF

Calibration	**Top**		**Bottom**	
	F in lb_f	**F in N**	**F in lb_f**	**F in N**
1	0.0308	0.137	0.0360	0.160
2	0.0328	0.146	0.0360	0.160
3	0.0306	0.136	0.0360	0.160
4	0.0324	0.144	0.0351	0.156
5	0.0337	0.150	0.0348	0.155
6	0.0317	0.141	0.0357	0.159
7	0.0312	0.139	0.0355	0.158
Average	0.0319	0.142	0.0355	0.158
Standard deviation	0.005	0.005	0.002	0.002

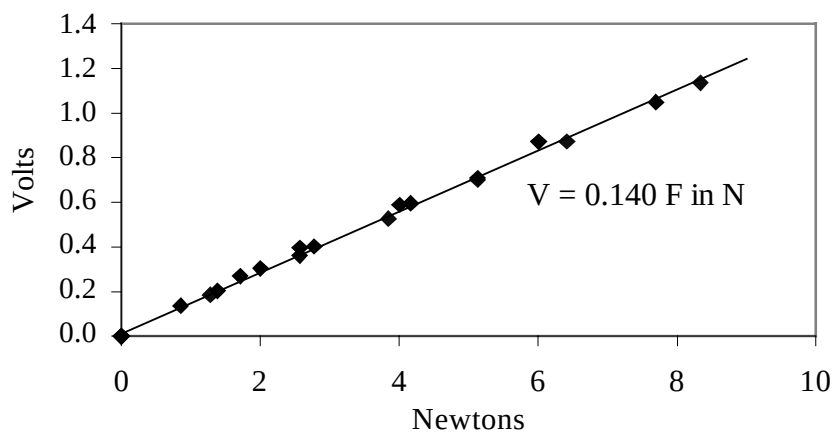

Figure 3.36: Top strip mean

In order to minimize errors due to the changing characteristics of the strain gages, it was decided to perform a calibration before and after each experiment and then take the average of the two. Table 3.6 shows the results of a typical calibration. The calibration method was applied to all the measurements described in the following chapter.

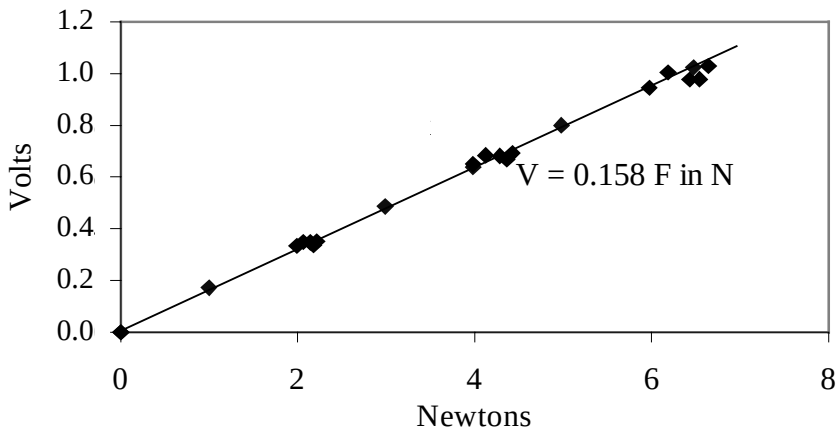

Figure 3.37: Bottom strip mean

Table 3.6: Typical calibration results for slope m in V = mF

Calibration	**Top**		**Bottom**	
	F in lb_f	**F in N**	**F in lb_f**	**F in N**
Before the test	0.0326	0.145	0.0308	0.137
After the test	0.0315	0.140	0.0317	0.141
Average	0.0319	0.142	0.0312	0.139

CHAPTER 4. EXPERIMENTAL PROCEDURES

4.1. INTRODUCTION

This chapter presents the experimental procedures that were used to compute the drag coefficients and to determine the water level variation caused by bridge piers. Two main sections present the different methodologies and the computational processes that led to the determination of the drag coefficient for bridge piers and the backwater effect of bridge piers.

4.2. DRAG COEFFICIENT FOR BRIDGE PIERS

Since the flow coming from the pumps had slight variations, the discharge was measured every three minutes. During the drag force measurements, the flow rate was read for each of the six flow conditions that are described later in this section.

In order to calculate the projected area of the submerged part of a pier onto a plane perpendicular to the flow (Equation 2.14), the water level downstream of the pier (Figure 2.1) had to be measured. For this purpose, the average of the two Pitot tubes just downstream of the pier (numbers 21 and 22, Figure 3.14) was used.

The drag force measurements were taken for six flow conditions in order to cover a wide range of Froude and Reynolds numbers. The first three sets were done with the North outside pump running with three different water levels: high, medium, and low. They were called NPH, NPM, and NPL, respectively. The last three sets were taken with all four pumps running (the two outside pumps, North and South, and the two Inside pumps). The water levels were high, medium, and low. The tests were called NSIPH, NSIPM, and NSIPL, respectively.

The first step in the experiment was to fix the model pier in the channel as described in Chapter 3 (Section 3.7.1.2). Then, the strain gages were linked together in order to form the two Wheatstone bridges for the top and the bottom strips. Figure 4.1 shows the oscilloscope that was used to visualize the voltage variations caused by the strain variations in the gages.

The second step was to perform a calibration using the devices described in Chapter 3 (Section 3.7.3). During the third step, the measurements were taken. First, a zero reading was taken using the flow reduction shield described in Chapter 3 (Figure 3.34). Afterwards,

the six sets of readings were taken. Figure 4.2 shows the piers while readings were being taken. The aluminum bar behind the pier was used to prevent the flow reduction device from moving laterally. Each measurement was acquired four times. After finishing the measurements, a final calibration was performed with similar conditions to the first one. During the

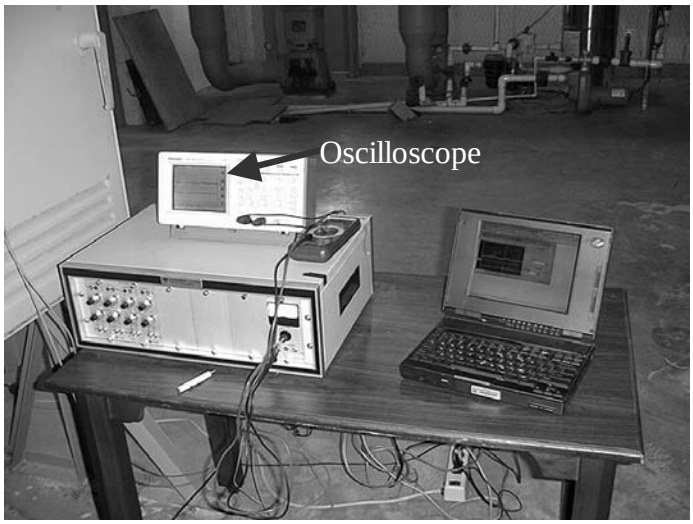

Figure 4.1: Electronic equipment

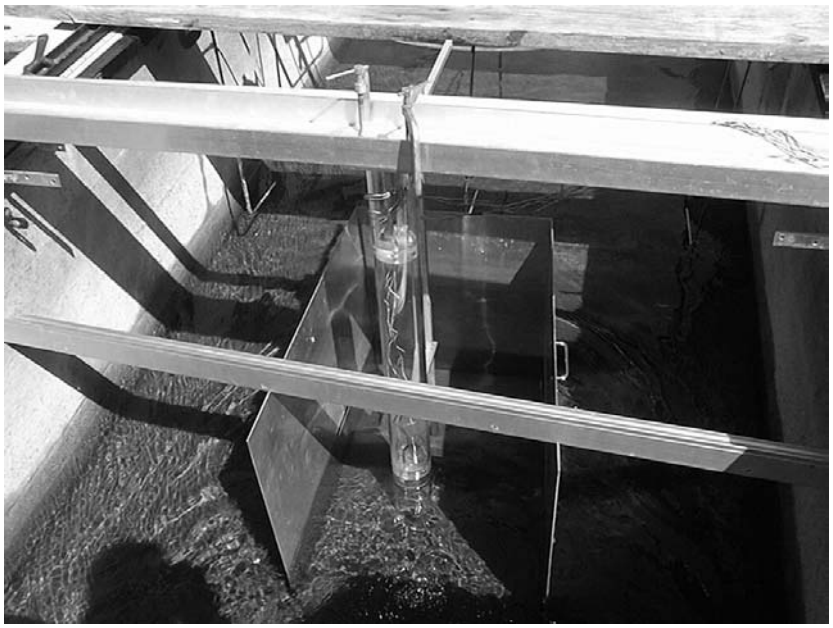

Figure 4.2: Zero reading measurement

data processing, the average of the two calibrations was used. Figure 4.3 shows the pier while measurements were being taken.

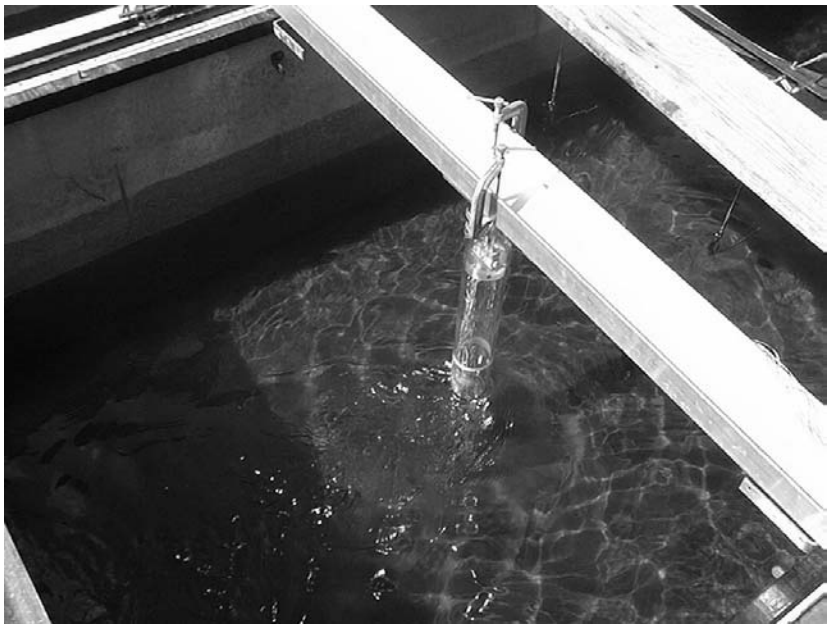

Figure 4.3: Measurement in progress

4.3. BACKWATER EFFECT OF BRIDGE PIERS

4.3.1. Data Collection

These experiments started immediately after the completion of the first series that involved measurement of the drag coefficients. One hundred experiments were done with the four pier configurations described in Section 3.4.

In this part of the research, two water level scenarios were compared; the first reflected the water level variation when the pier was in the channel at the location indicated in Figure 3.14, and the second when the water was freely flowing with no obstruction, i.e., in the absence of the pier. Six sets of measurement were performed for each experiment; three measured the effect of obstruction caused by the pier, and the remaining three described the situation when no pier was included. Since the flow coming from the pumps varied slightly,

six measurements for each working pump were performed using the flow meters. An arithmetic average was used to ascertain a final flow rate value.

At the beginning of each experiment, there was no water in the channel and the pier was not in the channel. The experiment started by flushing the 24 Pitot tubes for about 15 minutes in order to eliminate all the air bubbles from the flexible plastic tubes. Figure 4.4 shows the manifold used for flushing the tubing. At the same time, the Pitot tubes were checked and, if necessary, cleaned, to ensure that all the static ports (Figure 3.15) of each Pitot tube were not plugged.

Figure 4.4: The flushing process of the 24 tubes

While the flushing process was still taking place and after verifying that the Pitot tubes were all clean, the pumps were turned on, and the water level was fixed using the tailgate. When the water level in the channel rose above the Pitot tubes (Figure 4.5), the flushing was stopped and the flexible tubes (Figure 3.15) were connected to the manometer board. This procedure prevented air from re-entering the flexible tubes since air could cause errors in the manometer readings. Twenty to thirty minutes later, the first set of water surface elevations and flow measurements was done using the equipment described in Chapter 3.

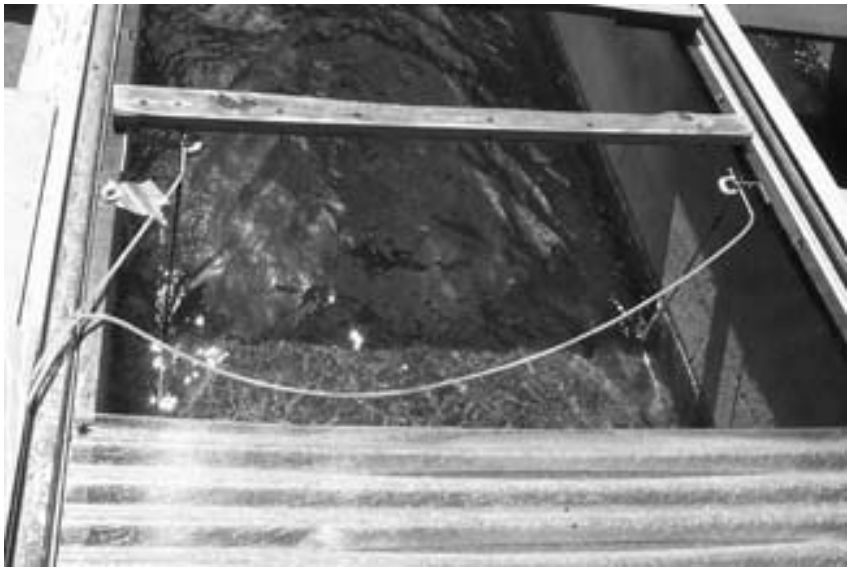

Figure 4.5: Two Pitot tubes in the channel while the water is flowing

Once the first set of readings was finished, the modeled pier was put in the channel (Figures 4.6 and 4.7) at the location indicated by Figure 3.14. As before, the second group of measurements was performed twenty to thirty minutes later, allowing enough time for the flow conditions to stabilize. The pier was then removed from the channel and a second set of readings without the pier was done. This procedure was repeated three times, which means that each experiment is a combination of six sets of measurements: three without the pier and three with the pier.

4.3.2. Processing Water Level Data

Table 4.1 is an example showing the water level measurements for Experiment 1 using the inclined manometer board and the 3.5 in. (8.9 cm) pier. The Station refers to the 24 Pitot tubes with locations shown in Figure 3.14. To establish an absolute reference, the static port of Pitot tube 22 was attached to both the inclined manometer and a vertical manometer with a scale calibrated to measure the water level above the deepest location in the channel. This reference level was measured for each Trial (with and without the pier in place) to determine the position of the water surface. The water level corresponding to each measurement was calculated from

Figure 4.6: 6.5 in. (16.5 cm) diameter pier in the channel when the water is flowing

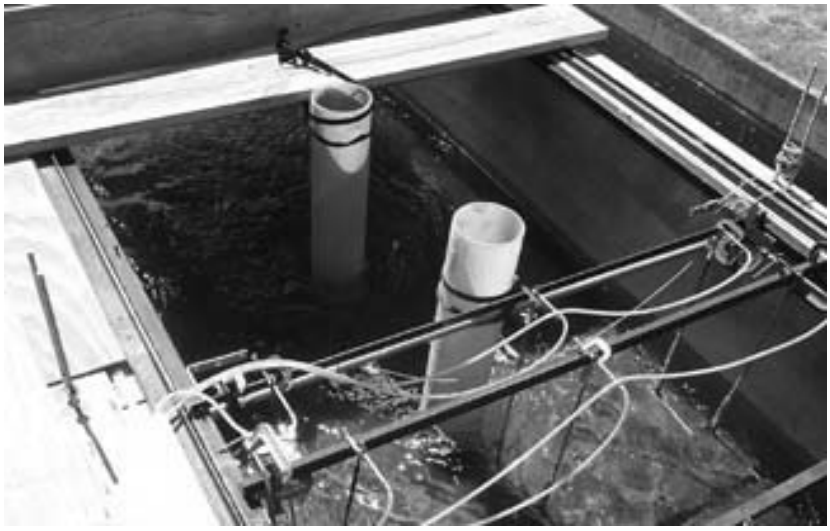

Figure 4.7: Twin-cylinder 6.5 in. (16.5 cm) diameter piers in the channel when the water is flowing

$$y_{i(j)} = \frac{H_{i(j)} - H_{22(j)}}{5} + y_{22(j)} \tag{4.1}$$

In this equation $y_{i(j)}$ is the water surface elevation at Station i for Trial j, $H_{i(j)}$ is the reading on the inclined manometer for Station i, Trial j from the inclined manometer board, $H_{22(j)}$ is the

Table 4.1: Inclined manometer board readings (cm) for Experiment 1 using the 3.5 in. (8.9 cm) pier

Station	Trial 1 No Pier	Trial 2 Pier	Trial 3 No Pier	Trial 4 Pier	Trial 5 No Pier	Trial 6 Pier
1	89.6	91.7	89.7	92.0	88.8	91.5
2	90.4	90.6	87.0	89.9	90.0	91.4
3	82.2	87.4	83.5	88.7	84.1	88.5
4	85.0	86.9	83.5	87.0	84.8	87.2
5	82.5	85.8	81.8	84.5	82.3	84.6
6	83.0	83.8	81.0	82.9	80.3	82.6
7	76.6	77.7	74.5	79.6	75.0	79.5
8	73.2	79.2	74.4	78.8	74.0	78.4
9	73.1	78.6	76.1	75.5	76.9	75.9
10	76.0	77.8	76.6	77.0	75.0	77.2
11	77.3	76.4	77.3	78.9	73.9	79.1
12	75.1	76.5	74.2	80.5	73.5	80.6
13	76.6	80.6	74.5	79.0	74.8	79.6
14	74.3	80.5	75.0	79.1	75.4	79.4
15	74.4	76.7	74.0	75.0	73.6	75.3
16	74.6	77.5	74.2	78.5	73.0	79.0
17	74.8	76.3	74.0	76.8	72.8	76.7
18	73.9	77.3	73.8	76.8	72.7	76.7
19	76.0	82.0	75.2	80.5	74.6	80.7
20	74.9	77.3	73.4	76.7	72.5	76.9
21	66.8	64.0	66.0	63.4	66.5	63.4
22	68.0	65.5	65.0	65.4	64.4	65.0
23	57.0	54.9	57.3	56.0	57.0	56.1
24	57.1	53.4	56.2	54.4	56.3	54.1

inclined manometer board reading for Station 22, Trial j, and $y_{22(j)}$ the reference water level read from the static port of Station 22 for Trial j. For the six trials in the experiment in Table 4.1, the reference water surface elevations were 33.22, 32.92, 32.92, 32.77, 32.77, and 32.77 cm, respectively. The water surface elevations corresponding to the manometer board readings given in Table 4.1 are shown in Table 4.2. The water level downstream from the pier was found by averaging the water level readings from Stations 21 and 22, which are approxi-

mately 10 ft (3.05 m) downstream from the pier. If the data showed consistent and small variations from one trial to the next, then all readings were used in obtaining the average. Otherwise, outliers were excluded. For the results shown in Table 4.2, the downstream water depth is y = 12.9 in. (32.8 cm).

Table 4.2: Water surface elevations (cm) corresponding to manometer board readings given in Table 4.1

Station	Trial 1 No Pier	Trial 2 Pier	Trial 3 No Pier	Trial 4 Pier	Trial 5 No Pier	Trial 6 Pier
1	37.54	38.16	37.86	38.09	37.65	38.07
2	37.70	37.94	37.32	37.67	37.89	38.05
3	36.06	37.30	36.62	37.43	36.71	37.47
4	36.62	37.20	36.62	37.09	36.85	37.21
5	36.12	36.98	36.28	36.59	36.35	36.69
6	36.22	36.58	36.12	36.27	35.95	36.29
7	34.94	35.36	34.82	35.61	34.89	35.67
8	34.26	35.66	34.80	35.45	34.69	35.45
9	34.24	35.54	35.14	34.79	35.27	34.95
10	34.82	35.38	35.24	35.09	34.89	35.21
11	35.08	35.10	35.38	35.47	34.67	35.59
12	34.64	35.12	34.76	35.79	34.59	35.89
13	34.94	35.94	34.82	35.49	34.85	35.69
14	34.48	35.92	34.92	35.51	34.97	35.65
15	34.50	35.16	34.72	34.69	34.61	34.83
16	34.54	35.32	34.76	35.39	34.49	35.57
17	34.58	35.08	34.72	35.05	34.45	35.11
18	34.40	35.28	34.68	35.05	34.43	35.11
19	34.82	36.22	34.96	35.79	34.81	35.91
20	34.60	35.28	34.60	35.03	34.39	35.15
21	32.98	32.62	33.12	32.37	33.19	32.45
22	33.22	32.92	32.92	32.77	32.77	32.77
23	31.02	30.80	31.38	30.89	31.29	30.99
24	31.04	30.50	31.16	30.57	31.15	30.59

Immediately upstream of the pier, there is a mound of water in the middle of the channel, i.e., the water level in the middle of the channel is higher than near the sides. The backwater was calculated from the increase in water surface elevations upstream of the mound. For example, with reference to Figure 3.14 and Table 4.2, Station 19 has a greater depth than Stations 18 and 20 for Trials 2, 4, and 6 with the pier in place. The same situation

exists when comparing Station 16 with Stations 15 and 17. However, looking at Stations 12, 13, and 14, there are no consistent lateral variations in water levels. Thus for this experiment, the two-dimensional mound in the water surface has dissipated across the channel at an upstream distance of approximately 2.9 ft (88 cm), and Stations 12, 13, and 14 can be used to calculate the backwater for this experiment. For each experiment, an evaluation was made to determine the cross section at which the mound had disappeared. The backwater was calculated from the average of the differences in water levels with and without the pier present, using Stations 21, 22, 23, and 24 separately as reference stations for the different trials. For example, using Station 21 as the reference, the backwater Δy_{21} was calculated from

$$\Delta y_{21} = \frac{1}{3} \sum_{i=12,13,14} \left[\frac{1}{3} \left(\sum_{j=2,4,6} \frac{H_{i(j)} - H_{21(j)}}{5} - \sum_{j=1,3,5} \frac{H_{i(j)} - H_{21(j)}}{5} \right) \right] \tag{4.2}$$

Similar equations were used with 22, 23, and 24 replacing 21 when Stations 22, 23, and 24 were used as a reference. The reason for using all four downstream stations as references was to take advantage of the law of large numbers to identify small quantities with multiple measurements using data that naturally shows considerable variation. Since the calculations use differences in differences of measured values, there is no inconsistency in also using Stations 23 and 24 even though their water surface elevations will be lower than Stations 21 and 22.

For this set of data, Δy_{21} = 1.51 cm, Δy_{22} = 1.04 cm, Δy_{23} = 1.23 cm, and Δy_{24} = 1.46 cm, giving an average value Δy = 1.31 cm (0.52 in.). Thus for Experiment 1 using the 3.5 in. (8.9 cm) pier, the value of $\Delta y/y$ is

$$\frac{\Delta y}{y} = \frac{1.31\text{ cm}}{32.8\text{ cm}} = 0.040 \tag{4.3}$$

The average discharge over the six trials was measured using the propeller meters as $Q_{measured}$ = 21.1 cfs (0.597 m^3/s). Using the correction discussed in Chapter 5 (see Equation 5.1), the Froude number for this experiment is

$$Fr = \frac{0.967\, Q_{\text{Flow Meter}}}{B\sqrt{g\, y^3}} = \frac{0.967 \times 0.597\ \frac{m^3}{s}}{\left(5\text{ ft}/3.28\,\frac{\text{ft}}{\text{m}}\right)\sqrt{9.81\,\frac{m}{s^2} \times (0.328\,\text{m})^3}} = 0.643 \tag{4.4}$$

where B is the channel width. Thus, for this experiment the main results are $\alpha = D_{pier}/B = 0.0583$, Fr = 0.643, and $\Delta y/y = 0.040$.

CHAPTER 5. RESULTS AND ANALYSIS

5.1. INTRODUCTION

This chapter presents the analysis of the experimental data. During the research period, flow measurements were made using different equipment. Calibration of the flow measurement devices is initially discussed. Drag coefficient and backwater results are then summarized and analyzed. The longitudinal extent of the mound of water in front of bridge piers is evaluated. Comparisons between experimental backwater values and Yarnell's results are shown, and a new equation is generated to fit the experimental results.

5.2. FLOW CALIBRATION

Three different techniques were used to compute the flow rate through the channel. These included use of propeller-type flow meters, a Venturi meter, and a thin-plate weir. These meters gave slightly different results, and this section provides a discussion of the results of flow calibration.

Forty-five calibration tests were done to compare the flow rates measured from the flow meters and the flow rates calculated from the weir readings. Moreover, four calibration tests compared the Venturi meter results to the propeller meters and to the weir measurements. Figure 5.1 presents the calibration results in all these cases.

The analysis of the results comparing the propeller meters and the weir showed an average difference of 9%, with the flow meter measurements being greater than those from the weir. In one of the calibration tests where three of the four installed pumps were on, the propeller meters gave a flow 22.8% greater than the value from the weir. The flow rate results thus show important differences between these measurement techniques.

In an attempt to control this difference, the propeller meters, which were always used to measure the discharge, were systematically cleaned to remove algae accumulation. Moreover, the propellers in the pipes coming from the pumps were always checked to ensure that this installation satisfied the catalog's requirements.

The cleaning, control, and review procedures did not help in reducing the difference between the flow rate from the flow meters and from the weir. Moreover, since the physical

model presented a closed system with one flow input and one output, no explanation was found of the flow rate discrepancy other than that the previous calibration of the weir possibly was no longer valid.

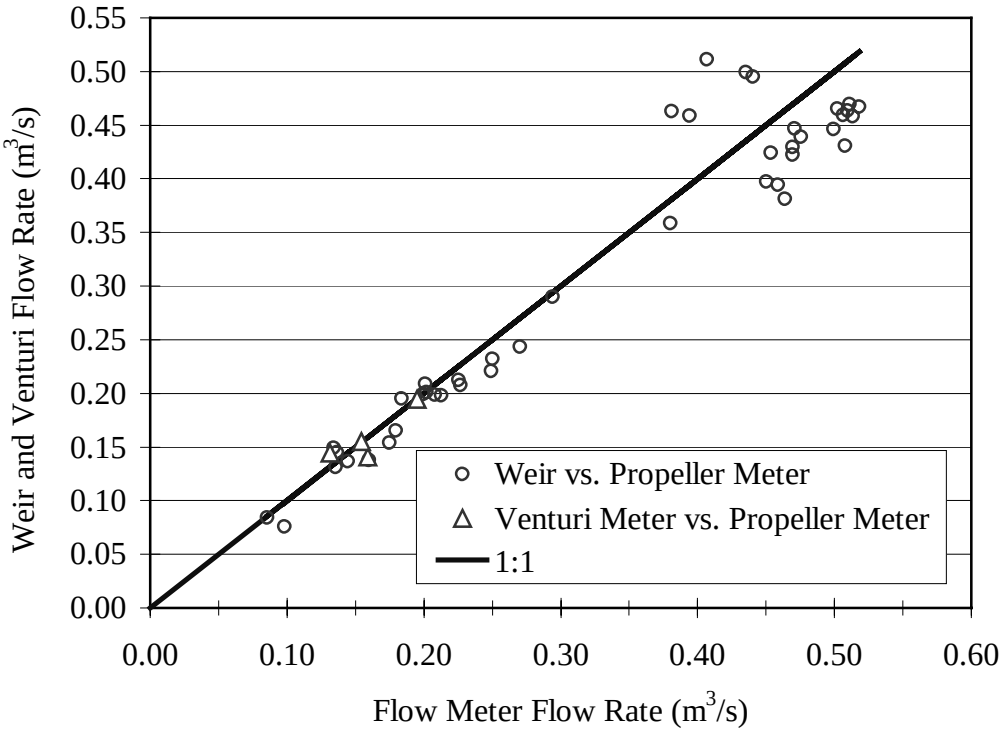

Figure 5.1: Calibration results comparing the flow rates from the propeller meters to the flow rates from the weir and from the Venturi meter

In an attempt to clarify the differences found using the flow meters and the weir, four experiments were done comparing the propeller meters and the Venturi meter. Figure 5.1 also shows these results. The average difference between these two devices was found to be 5.4%, with the flow meter measurements being greater than those from the Venturi meter. Note that the Venturi meter, as installed in the system, allowed calibration of only the flow from the North pump, which means that a calibration could not be done with a high flow rate.

The results showed that the Venturi meter was unable to bring new information to the flow calibration process. Therefore, a fourth flow-rate measurement technique was used. A 12-ft ID, 12-ft high circular tank was installed to allow the flows from the North and the

South pumps to be calibrated when operating independently. The procedure consisted of measuring the change of water depth in the tank during a given period of time. Having the diameter of the tank, the flow rate was then computed by dividing the volume of the water in the tank by the corresponding time period.

Thirteen calibration tests were done with the tank. Comparison between the propeller meters and the tank is provided in Figure 5.2. Tank measurements were considered to be accurate. This flow calibration led to

$$Q = 0.967\ Q_{\text{Propeller Meter}} \tag{5.1}$$

The flow rates were determined using the propeller meters and Equation 5.1.

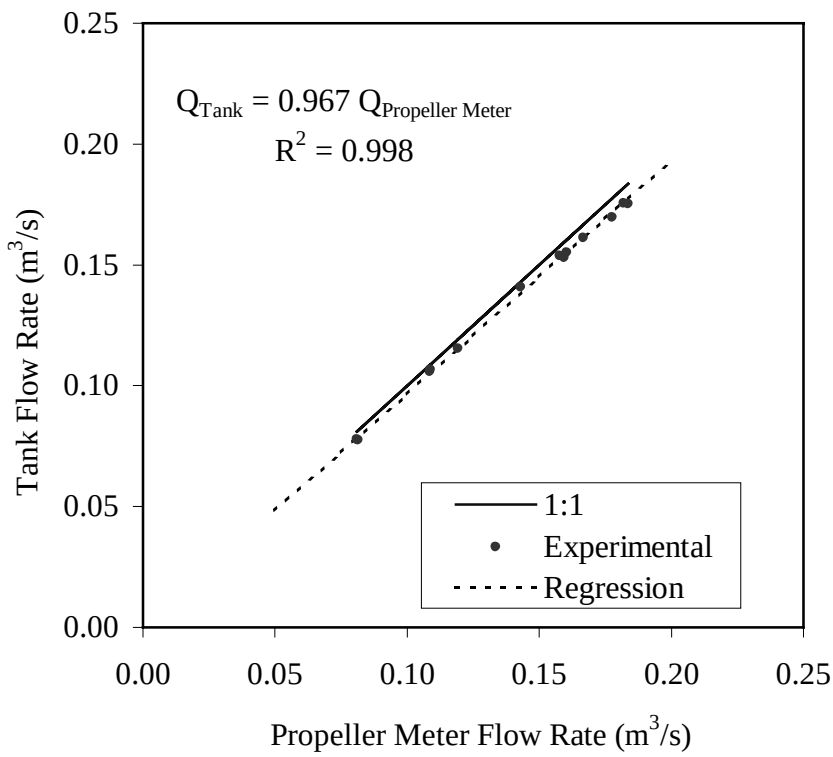

Figure 5.2: Calibration results comparing the flow rate measured from the flow meters to the flow rate measured from the tank

5.3. DRAG COEFFICIENT RESULTS

In this section, the results obtained from the different drag coefficient measurements are shown and discussed. Seventeen series of tests were done using a 3.5 in. (8.9 cm) diameter pipe for the different flows discussed in the previous chapter. Only two experiments were considered invalid and excluded from the analysis. For some tests, only four types of flow were used. The first five tests were done with one set of strain gages and the second ten tests with a different set.

After transferring the readings into the computer, they were processed to convert volts to force. As mentioned in Chapter 3, the mean of the two calibrations was used and an equation relating volts and force was generated for each strip (Figures 3.36 and 3.37). Table 5.1 shows the results for one of the calibrations and Table 5.2 shows the results of the corresponding test.

For example, by referring to Table 5.2, the data acquired for NPH (North outside pump, high flow rate) were 0.104 V for the top strip and 0.264 V for the bottom strip. To convert the results to force, the equations in Table 5.1 were used. For the top strip, the force was F_T = 0.104/0.142 = 0.731 N (0.165 lb_f). For the bottom strip, the force was F_B = 0.264/0.139 = 1.899 N (0.427 lb_f). The resultant drag force was $F_D = F_T + F_B$ = 0.731 + 1.899 = 2.63 N (0.591 lb_f). This same method was applied for all the tests.

Table 5.1: Calibration of m in V = mF for one experiment

Top		**Bottom**	
F in lb_f	**F in N**	**F in lb_f**	**F in N**
0.0313	0.139	0.0319	0.142

After calculating the drag force (F_D), the second step was to calculate the Froude number (Fr) using Equation 2.17 and the Reynolds number (Re) using Equation 2.16. Finally the drag coefficient (C_D) was calculated using Equation 2.14 and plotted versus the Froude number and versus the Reynolds number. The relationship between C_D and Fr for the ten useable tests with the 3.5 in. (8.9 cm) diameter smooth pier is shown in Figure 5.3. Figure 5.4 shows C_D versus Re for the same conditions. Test 6 was excluded from the set because its results

were considered erroneous due to some problems in the bottom strain gages that had to be replaced.

Table 5.2: Results of the corresponding test

	Volts		Forces using mean calibration					
			Top		Bottom		Total	
Flow	**Top**	**Bottom**	**(lb_f)**	**(N)**	**(lb_f)**	**(N)**	**(lb_f)**	**(N)**
0	0.000	0.000	0.000	0.000	0.000	0.000	0.000	0.000
NHP	0.104	0.264	0.164	0.731	0.427	1.900	0.592	2.631
NMP	0.093	0.337	0.147	0.653	0.546	2.426	0.693	3.079
NLP	0.084	0.499	0.132	0.587	0.809	3.596	0.941	4.183
NSIPH	0.559	1.137	0.884	3.930	1.843	8.190	2.727	12.12
NSIPM	0.443	1.244	0.700	3.113	2.015	8.959	2.716	12.07
NSIPL	0.388	1.297	0.614	2.729	2.100	9.341	2.716	12.07

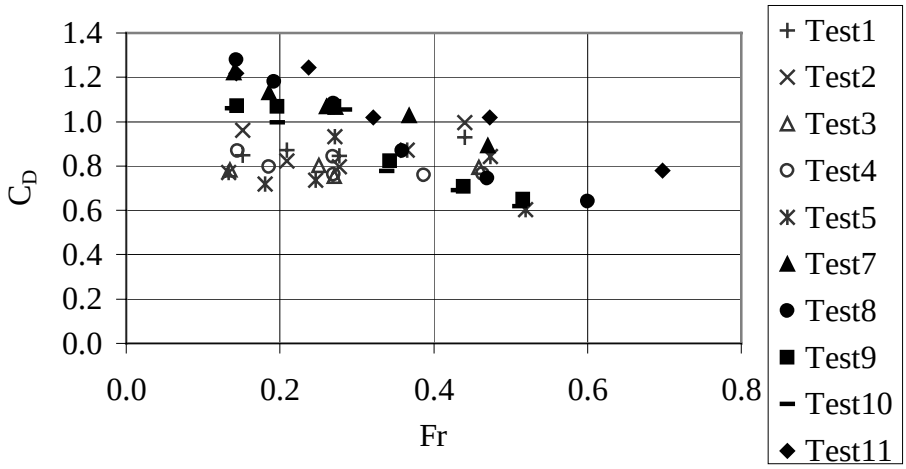

Figure 5.3: Relation between the drag coefficient and the Froude number for the tests performed with the smooth 3.5 in. (8.9 cm) diameter pipe

It is important to mention that Test 11 was performed after the redesign of the tail-gate. The redesign involved changing the place of the frame holding the tailgate from the

bottom of the channel to the top of its sidewalls. This change permitted higher Froude and Reynolds numbers.

As one can see in Figure 5.3 and Figure 5.4, for low Froude and Reynolds numbers, the drag coefficients for the first five sets of measurements were notably lower than the ones for the second five sets. This difference was much less for higher Froude and Reynolds numbers, since for the second sets of measurements the drag coefficient decreases more rapidly with increasing Fr and Re.

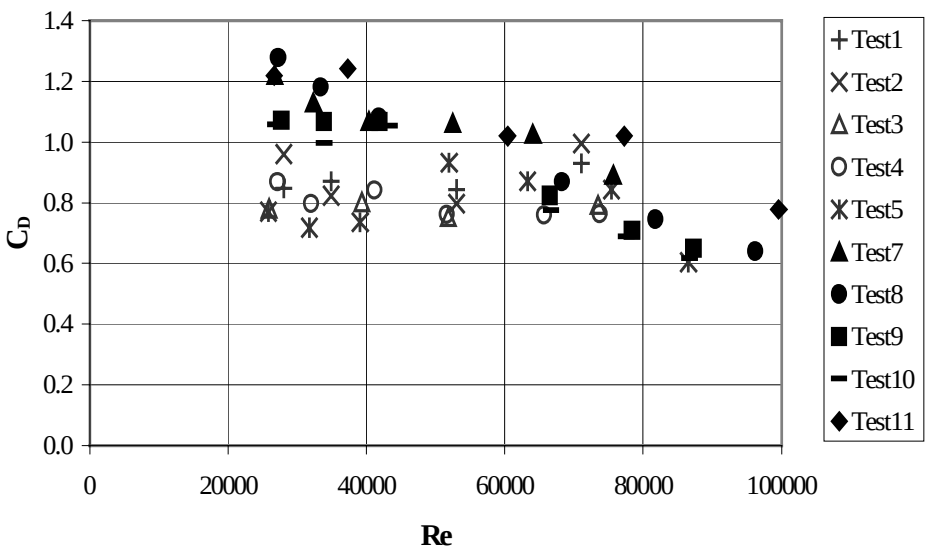

Figure 5.4: Relation between the drag coefficient and the Reynolds number for the tests performed with the smooth 3.5 in. (8.9 cm) diameter pipe

In order to identify the reasons for this difference between the first five experiments and the second five experiments, several possible causes were investigated. One possible cause was associated with the nature of the boundary layer and its separation from the pier. This was investigated by roughening the surface of the cylinder, assuring that the boundary layer became turbulent and thus possibly reducing the size of the separation zone and the magnitude of the drag coefficient compared to a laminar boundary layer for the same Reynolds number. This change is illustrated in Figure 2.4 for Re = 10^5 to 2.5×10^5. Since bridge piers in rivers have larger Reynolds numbers than in the model and usually have rougher sur-

faces than the plastic pipe used as a model pier, they always have turbulent boundary layers, so the same type of flow condition needs to be reproduced in the model.

The first method of roughening the pier was to cover the cylinder with a medium grain, waterproof sandpaper by fixing it to the pier using fine steel wires. Tests 12, 13, and 14 were performed using this method. The results are plotted in Figures 5.5 and 5.6.

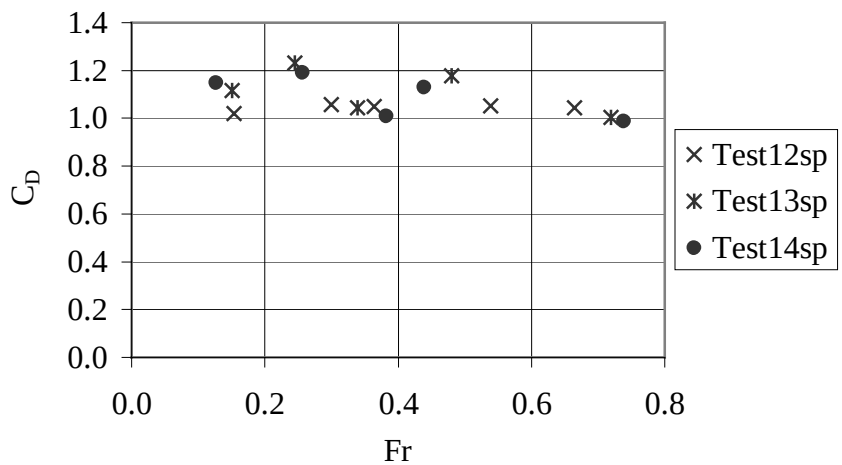

Figure 5.5: Relation between the drag coefficient and the Froude number for the tests performed with the 3.5 in. (8.9 cm) diameter pipe covered with sandpaper

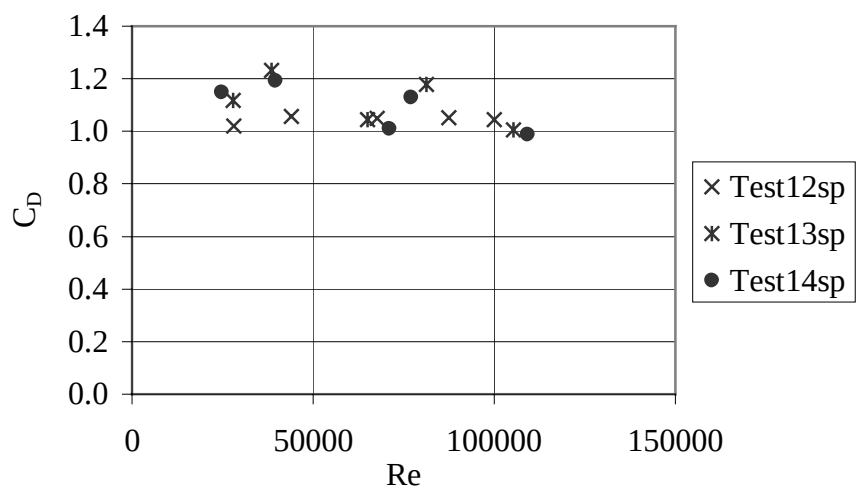

Figure 5.6: Relation between the drag coefficient and the Reynolds number for the tests performed with the 3.5 in. (8.9 cm) diameter pipe covered with sandpaper

As one can see by comparing Figures 5.5 and 5.6 with Figures 5.3 and 5.4, the drop in drag coefficient with increasing Fr and Re decreased. After studying these results and considering that the sandpaper was not tightly fixed to the cylinder at the end of the experiment, creating a bumpy and irregular surface, it was decided to glue a layer of medium size sand (0.25 mm to 0.5 mm) to the pier. This method would ensure a rough and regular surface. Figure 5.7 shows the roughened pier installed in the channel. Two tests were performed with this pier. Their results are summarized in Figures 5.8 and 5.9. Test 16 was not included because there were some technical problems with the strain gages during the data acquisition.

Figure 5.7: The 3.5 in. (8.9 cm) diameter roughened pipe in the middle of the channel's cross section

These results were similar to those obtained from the use of sandpaper. There was still a drop of the drag coefficient with increasing Froude and Reynolds numbers. Figures 5.10 and 5.11 show a summary of all the tests performed. Appendix A gives the detailed results of the 15 experiments for measuring the drag coefficients.

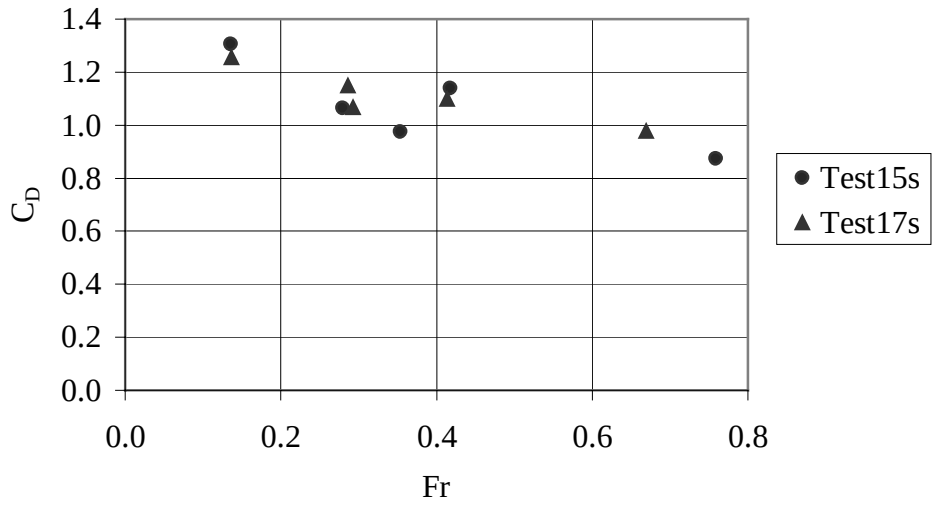

Figure 5.8: Relation between the drag coefficient and the Froude number for the tests performed with the roughened 3.5 in. (8.9 cm) diameter pipe

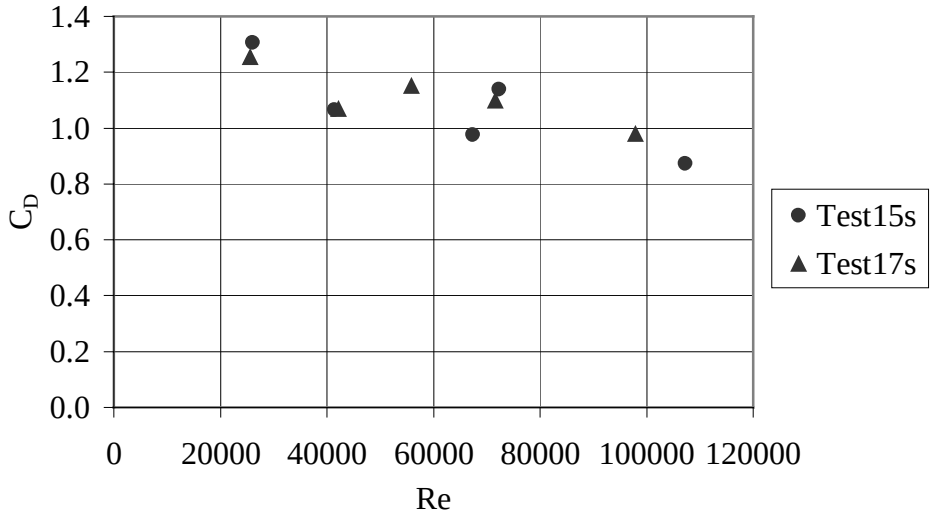

Figure 5.9: Relation between the drag coefficient and the Reynolds number for the tests performed with the roughened 3.5 in. (8.9 cm) diameter pipe

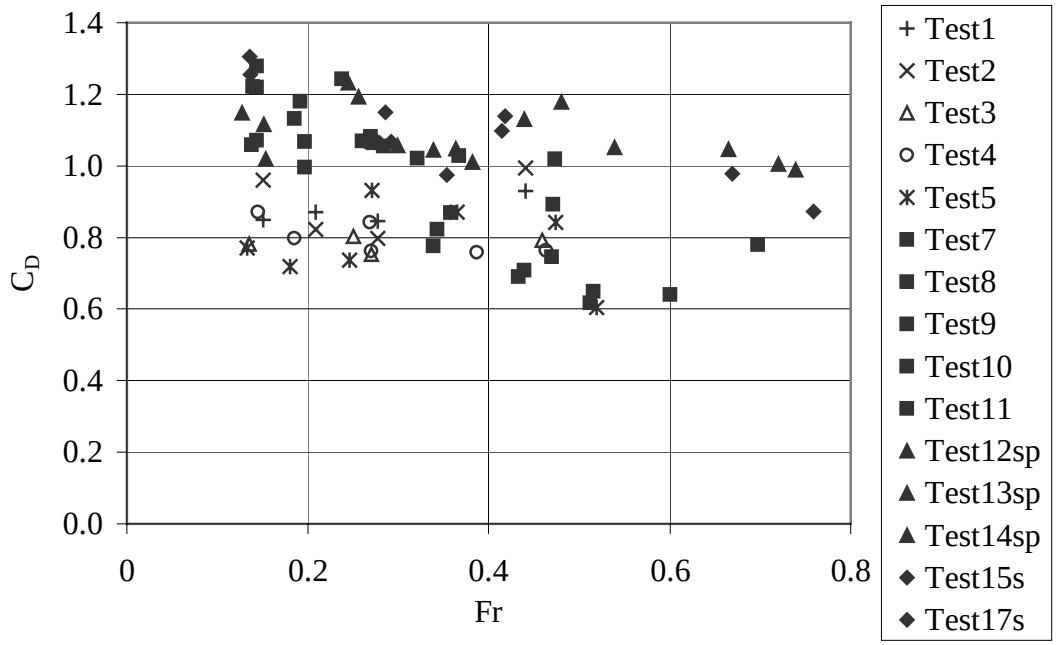

Figure 5.10: Comparative summary for C_D vs. Fr for all the experiments

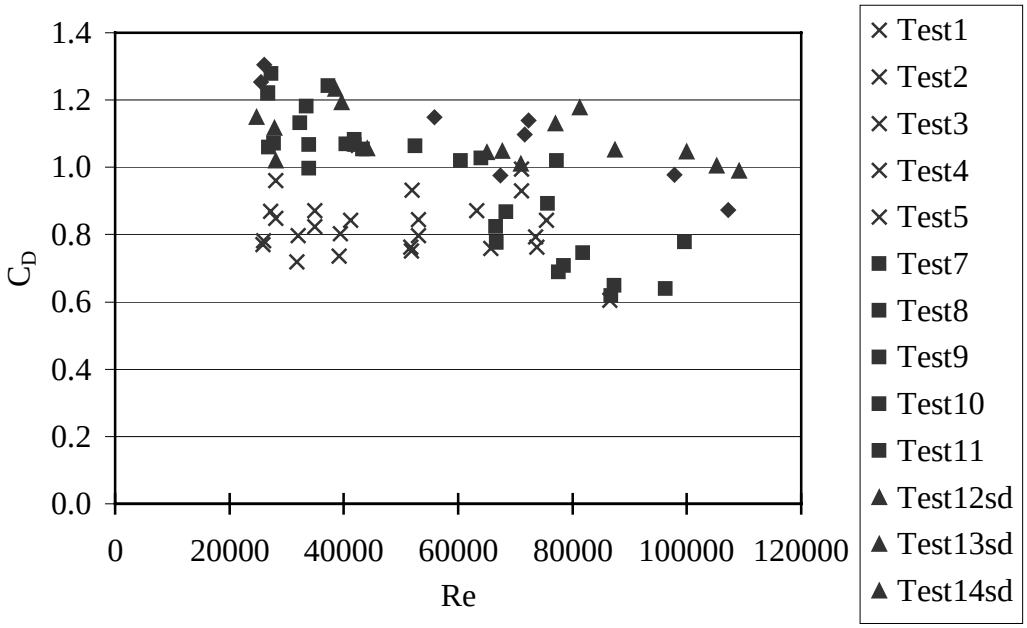

Figure 5.11: Comparative summary for C_D vs. Re for all the experiments

5.4. BACKWATER RESULTS

The backwater experiments were divided into four groups depending on the model pier(s) used (Figures 3.6 and 3.7). The four groups were

- Single 3.5 in. (8.9 cm) diameter circular pipe (Figure 3.6).
- Single 6.5 in. (16.5 cm) diameter circular pipe (Figure 3.6).
- Twin-cylinder 6.5 in. (16.5 cm) diameter pipes mounted one behind the other 2.2 ft (67 cm) apart.
- Rectangular pipe with semicircular nose and rectangular tail (diameter of the nose: 6.5 in. (16.5 cm). Length of the rectangle: 3 ft (91.4 cm)) (Figure 3.7). This is the "Yarnell" pier.

The first series of tests included twenty-eight experiments with the 3.5 in. (8.9 cm) diameter pier. This pier created a contraction ratio α = 5.8%. The water level (y) was measured in ten cross sections along the channel and the flow was recorded. Using this information, the Froude number (Equation 2.17) and the backwater generated by the pier (Δy) were calculated, as described at the end of Chapter 4. Figure 5.12 is a comparison of the experimental data for the 3.5 in. (8.9 cm) diameter pier with the values obtained from Yarnell's equation (Equation 2.2) and from a new proposed equation that is discussed later (Equation 5.3, which is called a 2-parameter equation in the following paragraphs). The reason for comparing with Yarnell's equation is because this equation is widely accepted and is in HEC-RAS, which is often used for the analysis of open channel flows. In addition, the new proposed equation is based on the form of Yarnell's equation.

A different pier was used in a second series of experiments. Twenty-two experiments were done with the 6.5 in. (16.5 cm) diameter pipe. In this case, the obstruction ratio α was equal to 10.8%. These results are plotted in Figure 5.13.

Twenty-four experiments were done with the twin-cylinder piers, i.e., with two 6.5 in. (16.5 cm) diameter piers mounted one behind the other. The distance separating the centers of the two cylinders was 2.2 ft (67 cm). The results are plotted in Figure 5.14.

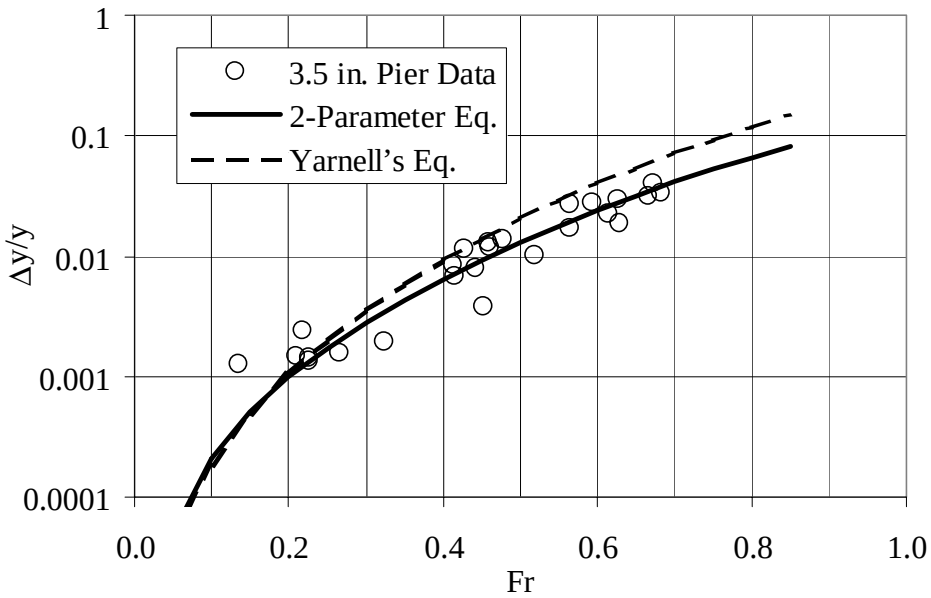

Figure 5.12: Plot of Δy/y vs. Fr for the 3.5 in. (8.9 cm) diameter pier. Yarnell's equation and a 2-parameter equation are also shown.

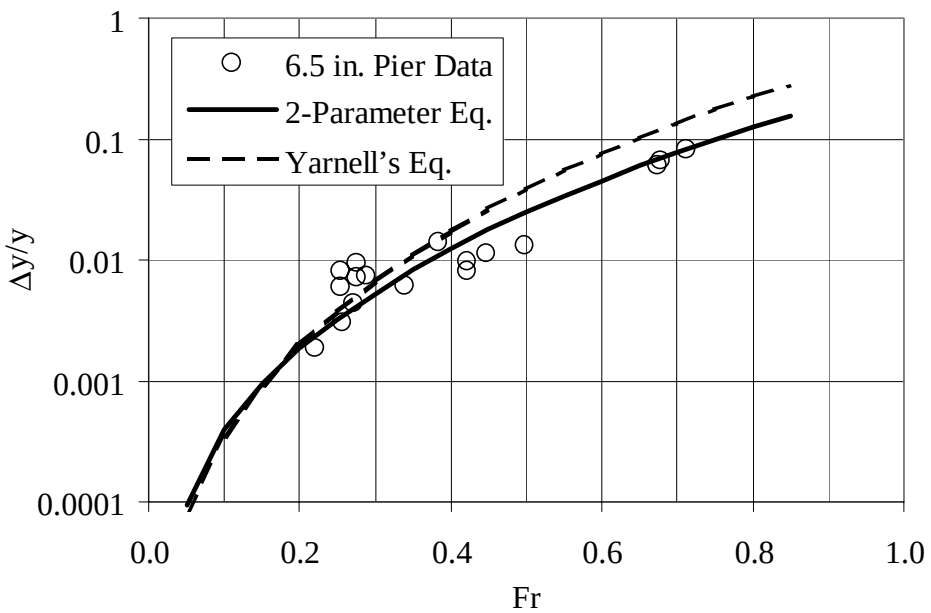

Figure 5.13: Plot of Δy/y vs. Fr for the 6.5 in. (16.5 cm) diameter pier. Yarnell's equation and a 2-parameter equation are also shown.

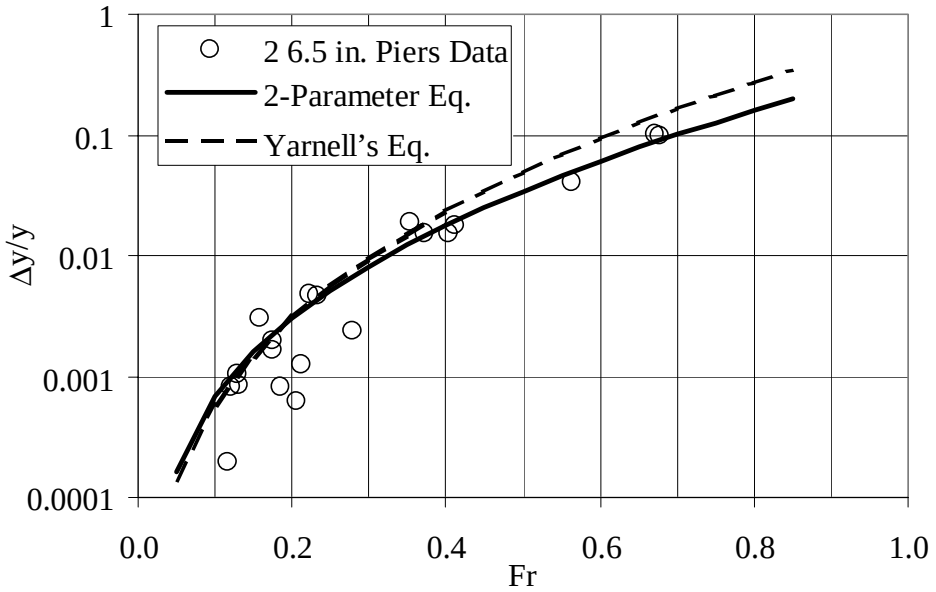

Figure 5.14: Plot of Δy/y vs. Fr for the twin-cylinder 6.5 in. (16.5 cm) diameter piers. Yarnell's equation and a 2-parameter equation are also shown.

The last set of experiments used a pier that was similar in shape to that used by Yarnell. It had a semicircular 6.5 in. (16.5 cm) diameter nose on the front of a 3 ft (91.4 cm) rectangular section (Figure 3.7). Twenty-seven experiments were performed with this pier shape, which had a contraction ratio of 10.8%. The results are plotted in Figure 5.15.

Appendix B gives the detailed results of the 100 experiments listed above.

5.5. TWO-DIMENSIONAL MOUND OF WATER UPSTREAM OF PIERS

Backwater calculations are usually performed as part of the analysis of upstream effects of channel encroachments for subcritical flows. Following standard engineering practice, such floodplain analyses are usually performed using one-dimensional open channel flow models such as HEC-RAS or WSPRO. The calculated backwater should reflect the uniform water level increase across the channel width, upstream of the bridge piers. However, measurements in this research clearly showed that there are local two-dimensional effects of bridge piers, with a mound on the water surface immediately upstream of the piers. There are actually two issues that are of interest. The first concerns the upstream extent of the two-dimensional water-level mound (i.e., at what upstream location may the water level be described by

a one-dimensional model). The second question concerns the upstream extent to which significant backwater effects are present. The first of these issues is addressed in the following discussion. The second issue is site specific and can be analyzed using empirical Δy/y values such as those in the previous section and standard open channel hydraulics models.

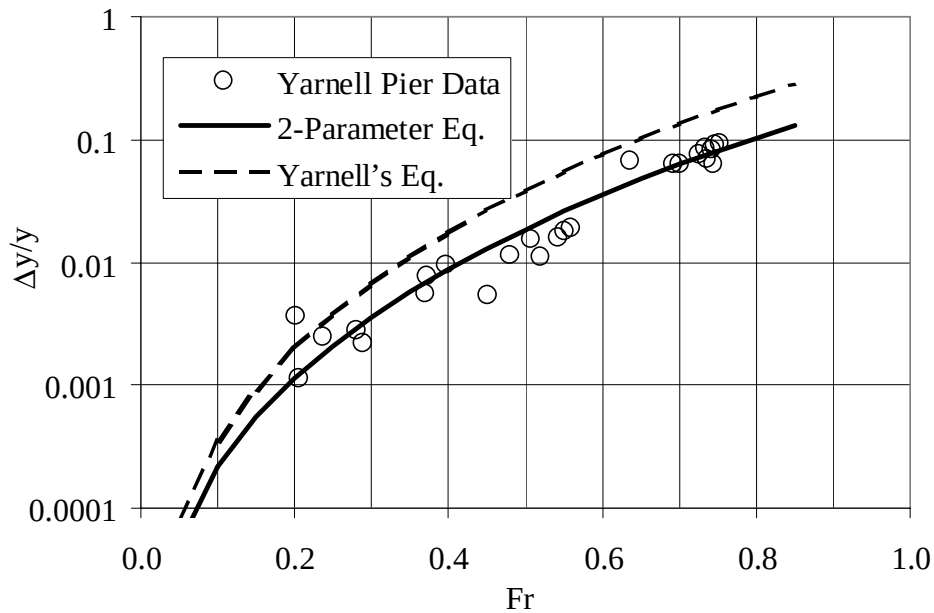

Figure 5.15: Plot of Δy/y vs. Fr for the Yarnell pier. Yarnell's equation and a 2-parameter equation are also shown.

Analyzing the water level variation for the four pier shapes and for several Froude number values showed that the two-dimensional mound of water in front of the pier was only localized and dissipated quickly in the upstream direction. For each experiment, Pitot tubes labeled 9, 10, and 11 (Figure 3.14) recorded the same water level elevation. This distance was almost equal to the channel width of 5 ft. Figures 5.16, 5.17, 5.18, and 5.19 show, for different Froude numbers, how the mound of water caused by the piers dissipated quickly in the upstream direction. It was noted that the maximum one-dimensional rise in water level occurred where the flow contraction began upstream of the piers.

These experimental results show that the two-dimensional effects are dissipated rapidly upstream of a pier, and that standard gradually varied hydraulic computation techniques may

be used to compute the upstream extent of the one-dimensional backwater influence. In this study, Δy values were obtained from the point at which the mound disappeared, i.e., where the water level at the sides and in the middle of the channel came together (Figures 5.16 –5.19).

5.6. COMPARISON BETWEEN YARNELL'S EQUATION AND THE EXPERIMENTAL DATA

As described in Chapter 2, the difference in water surface elevations immediately upstream and downstream from a pier is called backwater. The experimental backwater results for the four pier configurations were compared to the equation presented by David Yarnell who did 2600 experiments in a large channel. Not all of these experiments were for Type I (or Type A) flows. His channel was 312 ft (95.1 m) long, 10 ft (3.05 m) wide, and 10 ft (3.05 m) deep with flows up to 160 ft^3/s (4.5 m^3/s). His tests were run on wood piers giving four percentages of channel contraction, namely, 11.7, 23.3, 35, and 50%. However, modern bridge design normally involves channel contractions of less than 10%. Yarnell's empirical equation (Equation 2.2) for Type A flow is

$$\frac{\Delta y}{y} = K\left(K + 5Fr^2 - 0.6\right)\left(\alpha + 15\alpha^4\right)Fr^2 \tag{5.2}$$

where Δy is the one-dimensional backwater generated by the bridge pier(s), y is the original (i.e., undisturbed) local channel depth downstream of the pier, Fr is the Froude number downstream of the pier, α is the ratio of the flow area obstructed by the pier to the total flow area downstream of the pier, and K is a coefficient reflecting the pier shape.

The experimental results obtained during this research showed a similar trend to those predicted by Equation 5.2, as seen in Figures 5.12 through 5.15. Nevertheless, the present $\Delta y/y$ values were consistently lower than those predicted by Equation 5.2. Using the similarities in the shapes of the curves, Yarnell's equation was modified through introduction of two parameters that could be used to fit the new function to the experimental data. With the new parameters, β and μ, the modified equation is

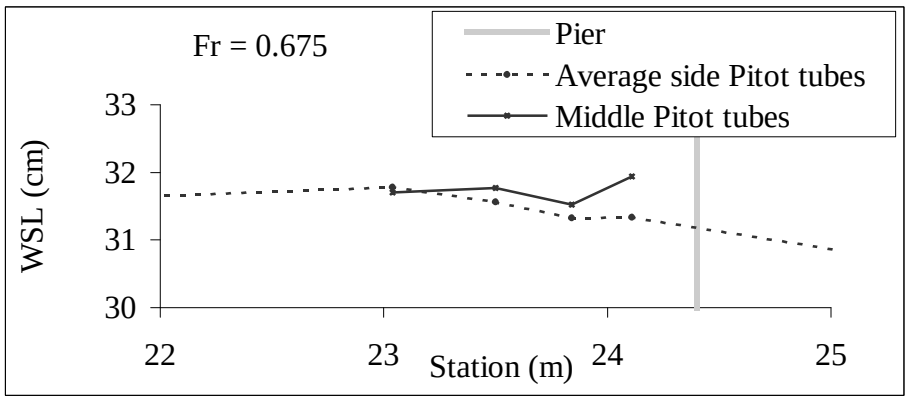

(a)

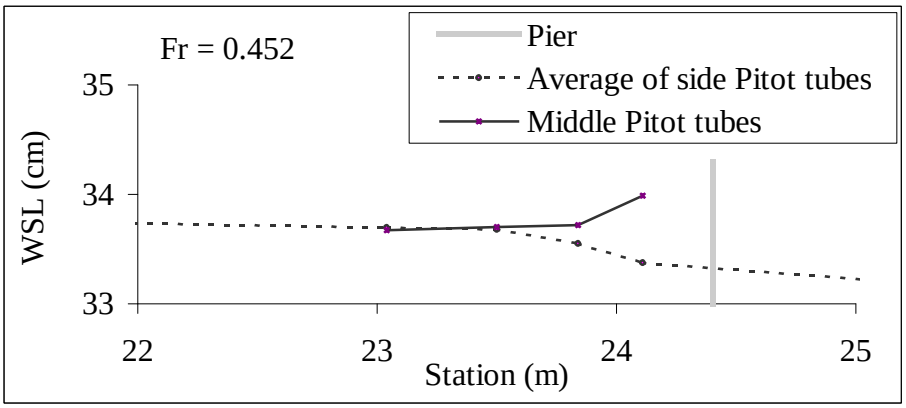

(b)

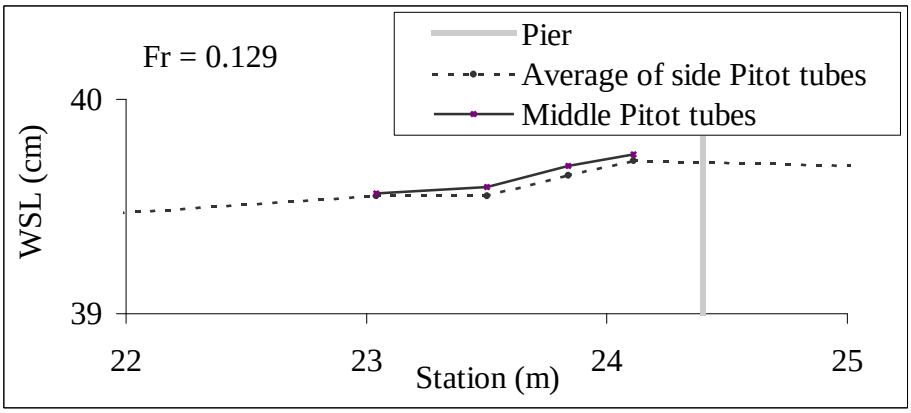

(c)

Figure 5.16: Water Surface Level (WSL) for the 3.5 in. (8.9 cm) diameter pier

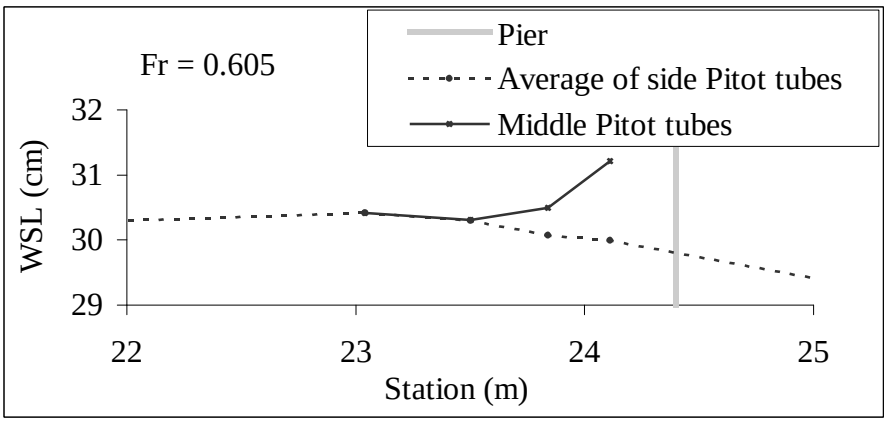

(a)

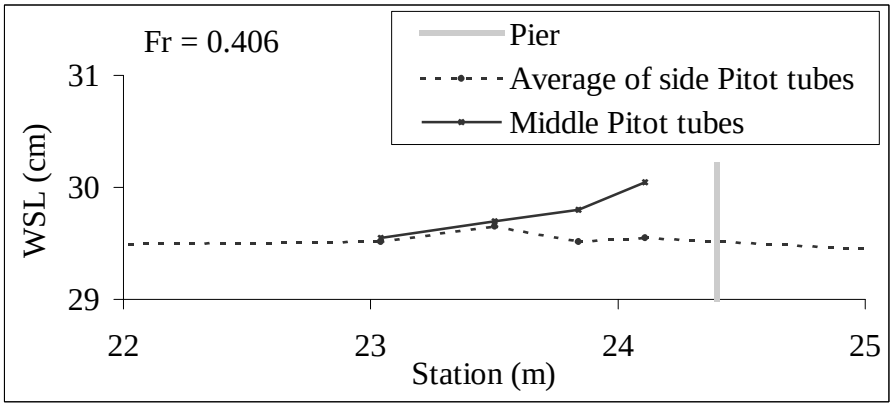

(b)

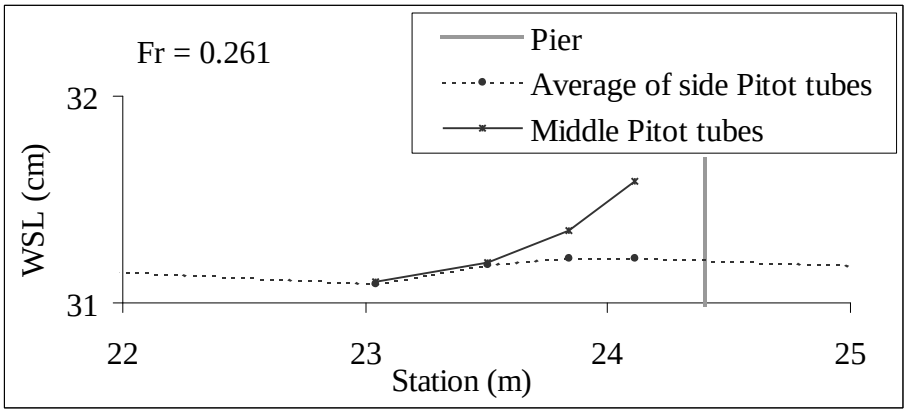

(c)

Figure 5.17: Water Surface Level (WSL) for the 6.5 in. (19.5 cm) diameter pier

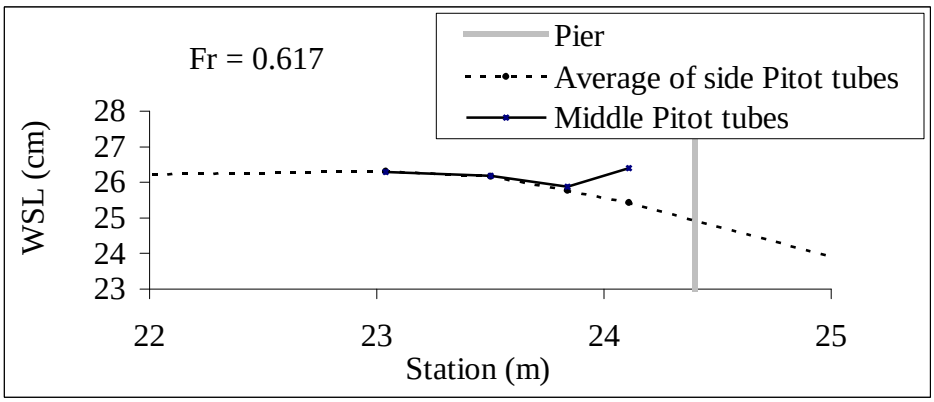

(a)

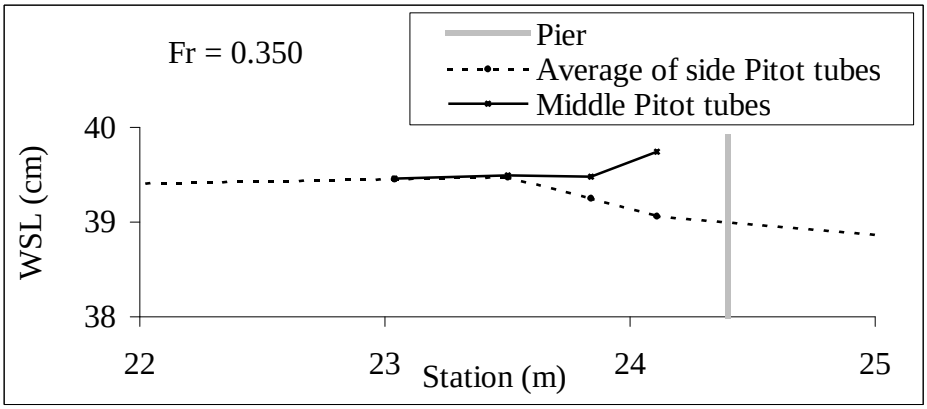

(b)

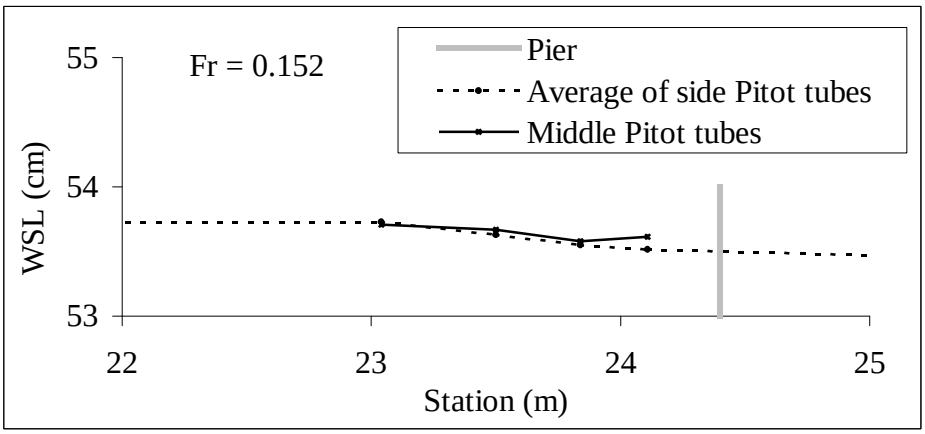

(c)

Figure 5.18: Water Surface Level (WSL) for the twin-cylinder 6.5 in. (16.5 cm) diameter piers

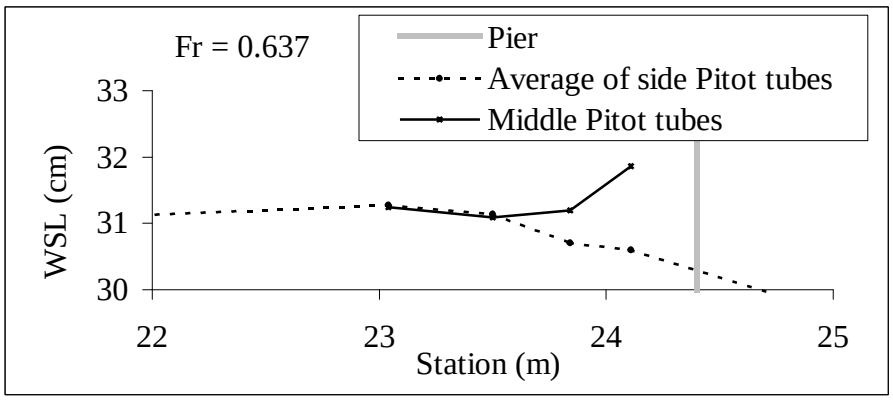

(a)

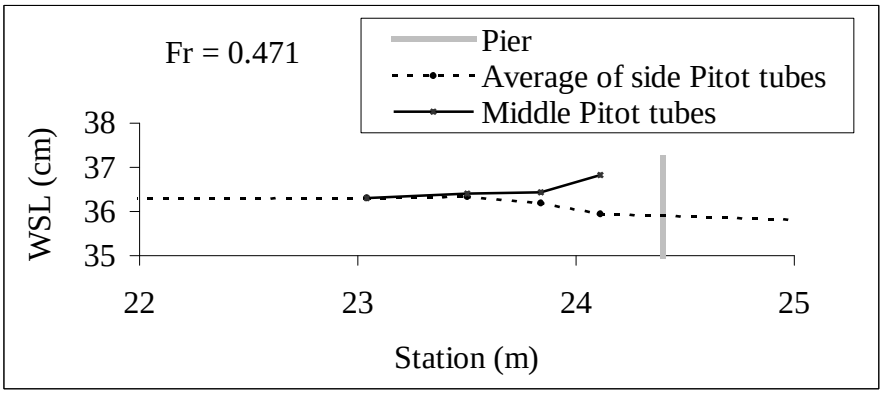

(b)

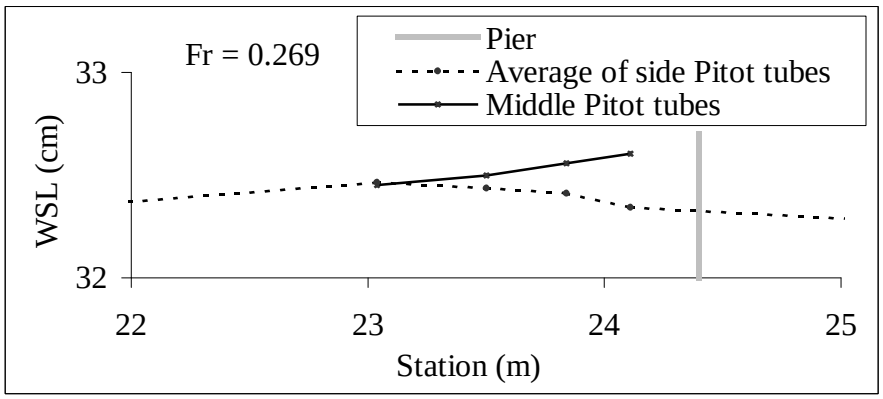

(c)

Figure 5.19: Water Surface Level (WSL) for the Yarnell pier

$$\left(\frac{\Delta y}{y}\right)_{calculated} = \beta K\left(K + \mu 5 Fr^2 - 0.6\right)\left(\alpha + 15\alpha^4\right) Fr^2 \tag{5.3}$$

The values of β and μ in Equation 5.3 were obtained by minimizing the mean square absolute error for the three data sets that used circular piers. The data for the Yarnell pier showed different behavior and was handled separately. The procedure for the circular pier data sets consisted of determining the values of those coefficients that minimized

$$\sigma = \sqrt{\frac{1}{N}\sum\left[\left(\frac{\Delta y}{y}\right)_{Experimental} - \left(\frac{\Delta y}{y}\right)_{Calculated}\right]^2} \tag{5.4}$$

where N is the number of data points. In calculating Equation 5.4, the data sets for the 3.5 in., 6.5 in., and twin piers were handled separately, and the average error of the three sets was minimized. The results are shown in Table 5.3, where RMS stands for root-mean-square. The reason for minimizing the absolute error, rather than relative error, is the belief that greater interest is placed on predicting large backwater values rather than uniform predictions over the entire range of $\Delta y/y$. The curves predicted by Equation 5.3 with parameters from Table 5.3 are also shown in Figures 5.12 through 5.15.

Table 5.3: β and μ coefficients for the circular piers

Coefficient β	1.24
Coefficient μ	0.40
RMS Absolute Error	σ = 0.00424

Data from the Yarnell pier experiments were analyzed separately from the data for the circular piers. A review of Figure 5.15 shows a number of data points near Fr = 0.5 that are lower than expected from the general curves. Trying to fit this data set by minimizing the absolute error leads to parameter estimates that are of questionable value. For this data set, the relative error, namely

$$\sigma = \sqrt{\frac{1}{N}\sum\left(\frac{\left(\frac{\Delta y}{y}\right)_{Experimental} - \left(\frac{\Delta y}{y}\right)_{Calculated}}{\left(\frac{\Delta y}{y}\right)_{Calculated}}\right)^2} \tag{5.5}$$

was minimized. The parameter values obtained for the Yarnell pier are presented in Table 5.4, and the resulting curve is shown in Figure 5.15. Because some values of $\Delta y/y$ in the denominator of Equation 5.5 are very small, the values of σ for relative errors are inherently larger than for absolute errors.

Table 5.4: β and μ coefficients for the Yarnell pier

Coefficient β	0.65
Coefficient μ	0.69
RMS Relative Error	σ = 0.517

Figure 5.20 compares results from this study with various empirical literature relationships that were described in Chapter 2. This figure is similar to Figure 2.3, except that a more representative range of contraction ratios α is shown. The calculations leading to Figure 5.20 were made using an expansion loss coefficient of 0.5 in calculating the value of Fr at which choking occurs. The ranges of values shown were calculated without reference to the range of variables used in obtaining the empirical equations. Indeed, for α = 0.025 and 0.05, D'Aubuisson's equation gives negative backwaters. On the other hand, for α = 0.15, which is within or close to the range of α values for all of the experiments, the predictions from all but one of the equations are rather close.

5.7. DRAG COEFFICIENTS AND SCALE EFFECTS

As shown in Chapter 2, drag forces exerted on bridge piers are directly related to the amount of increase in the water level elevation upstream of the pier. Drag coefficients calculated from Equation 2.28 are shown in Figure 5.21 for Yarnell's equation (Equation 5.2) and the results from this research (Equation 5.3). The trend exhibited by C_D for $\alpha \geq 0.1$ from both equations are generally what would be expected. This trend is that C_D should increase

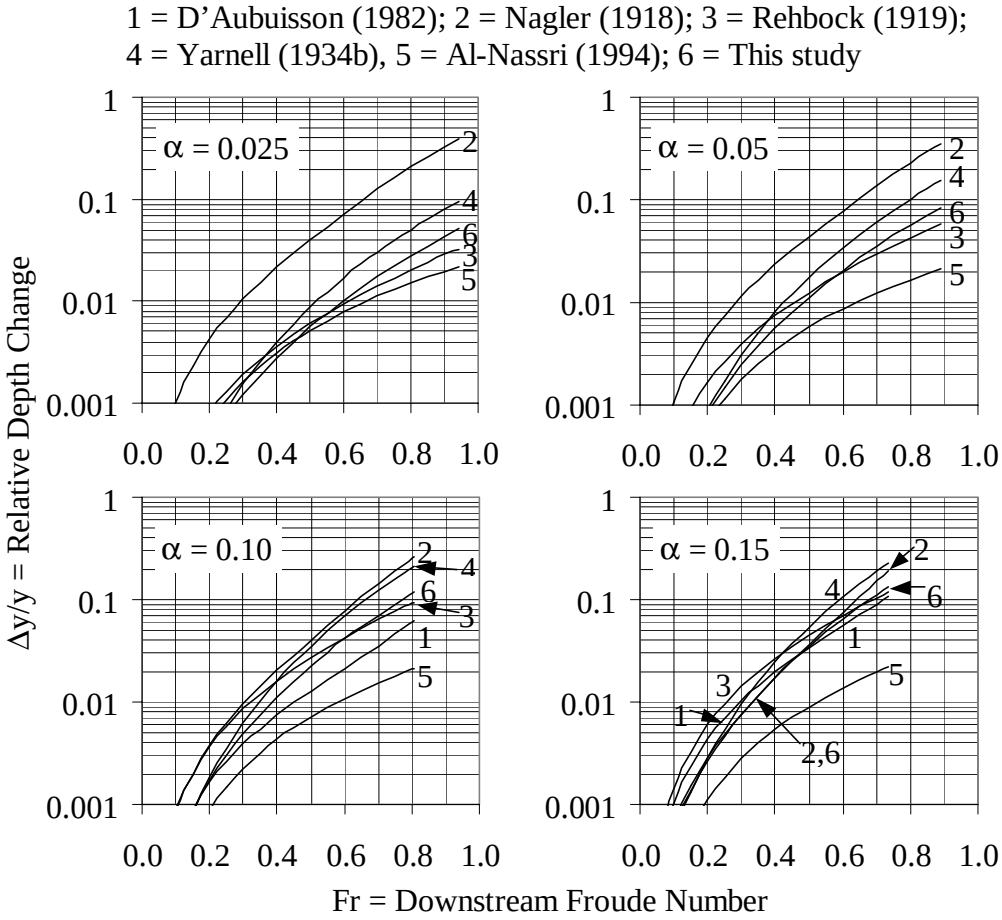

Figure 5.20: Various relationships for backwater, including the results from this study

with increasing Fr for a given α and that C_D should be independent of α for small α values since the amount of flow contraction becomes negligible as α decreases. On the other hand, the behavior of the curves for α = 0.05 and 0.025 for large Fr is different from what would be expected. The physical basis for a decrease in C_D with increasing Fr is not clear. These curves illustrate one of the cardinal principles of using empirical relationships, namely that such relationships should not be used outside the range of parameters for the experiments from which the relationships are derived. The smallest α used by Yarnell was 0.117. Thus, his equation should not be used for smaller α values. The equation proposed herein is based on Yarnell's equation, and this may be the reason for its showing similar behavior. Also, the smallest α in this research was 0.058. The behavior of the C_D curves in Figure 5.21 indicates

that these equations probably give acceptable results for the smaller α values and Fr less than about 0.5. However, for small α and large Fr, the relative errors may be substantial.

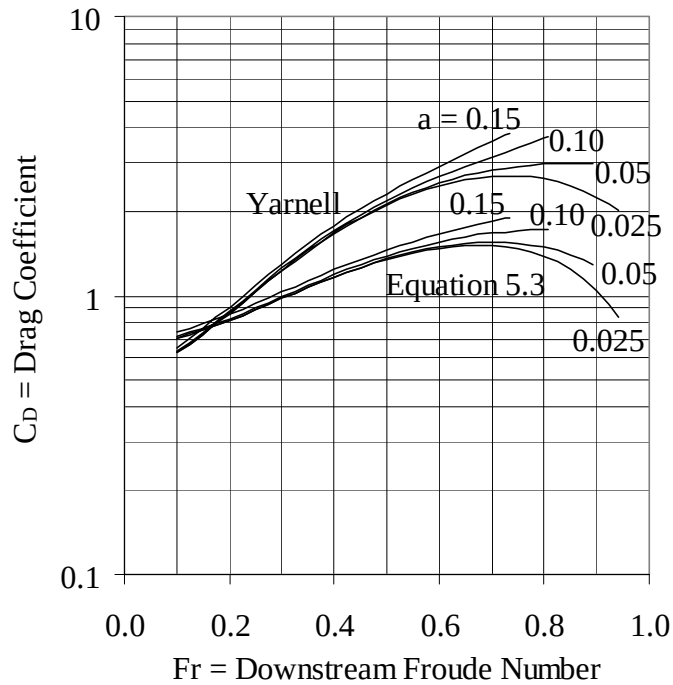

Figure 5.21: Drag coefficient as a function of downstream Fr for various values of the contraction ratio

Unlike the curves shown in Figure 5.21, the data shown in Figure 5.10 suggest that C_D values remain constant or might actually decrease with increasing Fr. Figure 5.22 was developed to evaluate the internal consistency of the data from the drag force measurements and from the backwater measurements. In this figure, the C_D values labeled "BW" were calculated from the measured values of Δy/y while those labeled "CD" were from the measurements of the drag forces. While there is very large scatter in the data, there also is a general consistency between these two data sets for α less than about 0.5.

The first part of the current research was aimed at measuring drag coefficients on bridge piers for a range of Froude and Reynolds numbers. Review of Figure 5.11 shows that the drag coefficient decreases for increasing Reynolds numbers. While the cause of the data scatter shown in this and other figures was not identified, it was noted that roughening the

pier's surface (test numbers 15s and 17s) reduced the downward trend of the drag coefficients with increasing Reynolds numbers. The average drag coefficient value for the set of experiments done with the roughened pier was found to be 1.1. This value has also been found by other researchers for the same range of Reynolds numbers, as shown in Figure 5.23.

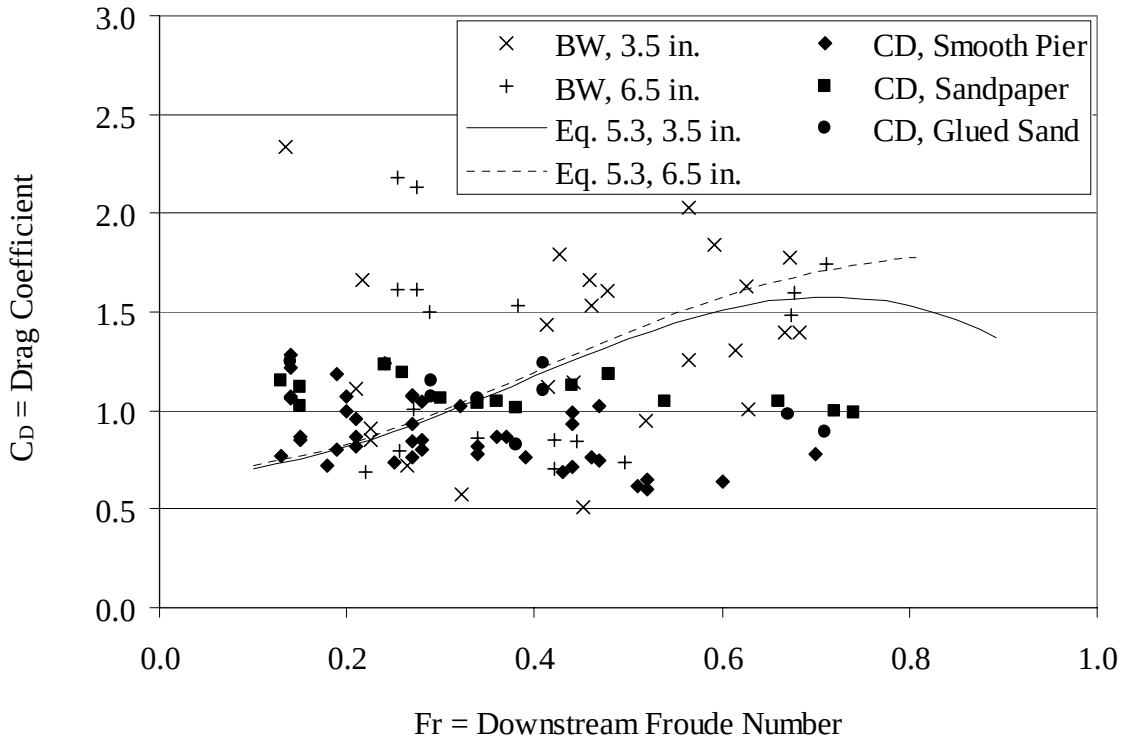

Figure 5.22: Measured and calculated C_D values along with the curve from Equation 2.28 with α = 0.05

Reynolds numbers for prototype piers usually have values higher than 10^6. For example, the Reynolds number of a circular pier with a diameter of 3.28 ft (1 m) in a flow with a velocity of 6.6 ft/s (2 m/s) is $5x10^6$. Few studies have been done to determine drag coefficients for high Reynolds numbers. However, at very high Reynolds numbers exceeding 10^6, the drag coefficient increases at a considerable rate from 0.22 for Re = 10^6 to a maximum value of 0.56 for Re= 4×10^6, based on the measurements reported by Roshko (1961), as shown in Figure 5.24. At Re = 10^7 the drag coefficient reaches a value of C_D = 0.55. These results are for flows with no free surface. For these conditions, C_D depends solely on the

Reynolds number. The backwater measured by Yarnell and in this study indicate that C_D increases with increasing Fr. This is the type of behavior that should be expected for free surface flows. Thus, these results indicate that the scale effects from not having the same Reynolds numbers in the model and prototype should not be a significant problem, so that the model results can be reliably used for prototype conditions.

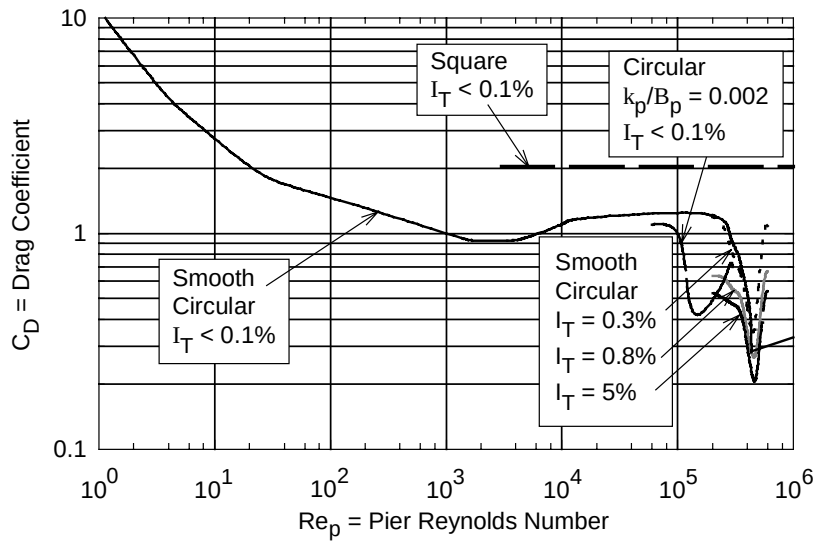

Figure 5.23: Drag coefficients for cylinders without free surface effects

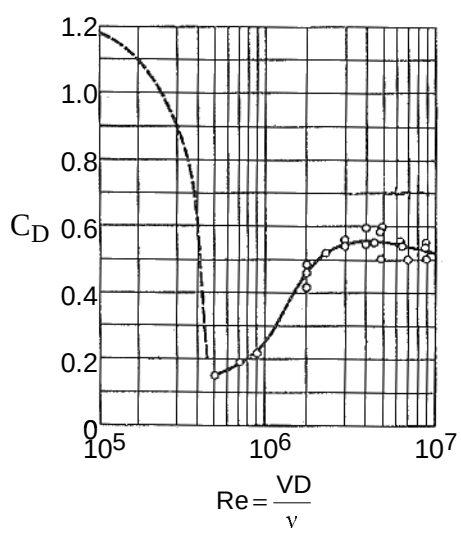

Figure 5.24: Drag coefficient for circular cylinder at very large Reynolds number after the measurements of Roshko (1961) and Jones *et al.* (1969)

CHAPTER 6. SUMMARY, DISCUSSION, AND CONCLUSIONS

This study has evaluated the water level change due to bridge piers and the nature of the variation of water level upstream of the piers. The three study objectives are stated in Section 1.1. The underlying objective was to evaluate the magnitude of the water level increase (backwater) caused by bridge piers, and to determine the upstream extent of significant backwater effects. Drag forces on bridge piers were also investigated since they provide complementary information on backwater effects. Indeed, Equation 2.28 shows the approximate relationship between the drag coefficient and backwater. While it is possible to represent backwater by increasing the value of Manning's n through the channel section containing piers, the discussion in Section 2.7 suggests that the effort required to select an appropriate n-value is probably as great as the effort to directly calculate the backwater using appropriate equations.

Chapter 3 describes the experimental equipment while Chapter 4 outlines the experiment procedures for measurement of drag coefficients and changes in water level associated with pier backwater. The results from these experiments are presented in Chapter 5.

Drag coefficients were measured because they are directly related to backwater effects, and it was hoped that such measurements would provide further insight into the factors that determine backwater. As shown in Figures 5.10 and 5.22, there is considerable scatter in the measured and calculated C_D values. One conclusion concerns scale effects, which are discussed in Sections 2.6 and 5.7. The physical model studies did not establish Reynolds number similarity, and prototype Re are much larger than model Re. However, both data from the literature and the results of this study indicate that the drag coefficients are controlled by the Froude number rather than the Reynolds numbers for piers in free surface flows. Thus, the inability to have equal model and prototype Reynolds numbers does not present a problem.

One of the issues that was investigated concerns the upstream extent of backwater effects, and in particular the two-dimensional water-level mound that is formed immediately upstream of the piers. For all cases, it was found that these two-dimensional effects are local

and are dissipated within an upstream distance equal to the width of the channel. This means that for most cases, these effects will exist only in or close to the right-of-way property. Off-site backwater effects can be calculated using standard one-dimensional hydraulic models.

The water level changes measured in this study are generally smaller than those calculated using Yarnell's equation for backwater caused by bridge piers, and this is true for all contraction ratios (α). Equation 5.3 is presented as an improved model for calculating backwater effects of bridge piers. Additional model studies can confirm (or improve) the parameter value estimates given in Table 5.3.

CHAPTER 7. REFERENCES

Al-Nassri, S. (1994): "Effect of bridge pier shape and contraction ratios on backwater profile," *Hydraulic Engineering 1994*, (ed. G. Controneo and R. R. Rumer), American Society of Civil Engineers, Buffalo, NY, p. 563-568.

Anonymous (1939): "Report of the engineering aspects of the flood of 1938: Appendix 1 - Theoretical and observed bridge pier losses," U. S. Engineer Office, Los Angeles, CA, p. 61, May.

Anonymous (1997): *SAP 2000 Analysis Reference*, vols. I and II, version 6.1, Computers and Structures, Inc., Berkeley, California.

Bos, M. G. (1989): *Discharge Measurement Structures*, Publication 20, Third edition, International Institute for Land Reclamation and Improvement, Wageningen, The Netherlands.

D'Aubuisson de Voisins, J. F. (1852): "A Treatise on Hydraulics for the Use of Engineers," Translated from French and adapted to English units by J. Bennett, p. 532, Boston, MA

Franzini, J.; Finnemore, J. (1997): *Fluid Mechanics with Engineering Applications*, Ninth Edition, McGraw Hill, New York, NY.

Hunt, John; Brunner, Gary W; Larock, Bruce E. (1999): "Flow transitions in bridge backwater analysis," *Journal of Hydraulic Engineering*, American Society of Civil Engineers, vol. 15, no. 9, pp. 981-983, September.

Jones, G. W.; Cinotta, J. J.; Walker, R. W. (1969): "Aerodynamic forces on a stationary and oscillating circular cylinder at high Reynolds numbers," NACA TR R-300.

Kaatz, Kelly J.; James, Wesley P. (1997): "Analysis of alternatives for computing backwater at bridges," *Journal of Hydraulic Engineering*, American Society of Civil Engineers, vol. 123, no. 9, pp. 784-792, September.

Nagler, F. A. (1918): "Obstruction of Bridge Piers to the Flow of Water," *Transactions*, American Society of Civil Engineers, v. 82, pp. 334-395.

Rehbock, T. (1919): "Zur Frage des Bruckenstanes," *Zentrolblatt des Bauverwattung*, Berlin, Germany, vol. 39, no. 37.

Roshko, A. (1961): "Experiments on the flow past a circular cylinder at very high Reynolds numbers," *Journal of Fluid Mechanics*, vol. 10, pp. 345-356.

Rouse, H. (1946): *Elementary Mechanics of Fluids*, Wiley, New York, NY, pp. 376.

Seckin, Galip; Yurtal, Recep; Haktanir, Tefaruk (1998): "Contraction and expansion losses through bridge constrictions," *Journal of Hydraulic Engineering*, American Society of Civil Engineers, vol. 124, no. 5, pp. 546-549, May.

Stevens, J. C. *et al*. (1942): "Hydraulic Models," *Manual of Engineering Practice*, No. 25, American Society of Civil Engineers, New York, p. 110.

TxDOT (1997): "Hydraulic Design Manual," Fourth Edition, Texas Department of Transportation, Design Division, Austin, TX, January.

Wisner, P; Townsend, R; Sabourin, J; Leitch, D. (1989): "Joint use of the HEC-2 model and a physical model for floodplain delineation upstream of a bridge," *Canadian Journal of Civil Engineering*, vol. 16, no. 1, p. 1-7, February.

Wood, A; Palmer, R; Petroff, C. (1997): " Comparison and assessment of zero-rise floodplain ordinances," *Journal of Water Resources Planning and Management*, vol. 123, no. 4, American Society of Civil Engineers, New York, NY, July-August.

Yarnell, D. L. (1934a): "Pile trestles as channel obstructions," U. S. Dept. of Agriculture, Technical Bulletin, p. 429, July.

Yarnell, D. L. (1934b): "Bridge piers as channel obstructions," U. S. Dept. of Agriculture, Technical Bulletin, pp. 442-451, November.

APPENDIX A. DATA FROM DRAG FORCE EXPERIMENTS

A.1. Smooth pier (Experiments 1 to 11)

Experi-ment	Flow	Depth (m)	Velocity (m/s)	Fr	Re	C_D
1	NPL	0.42	0.42	0.21	35000	0.87
	NPH	0.52	0.34	0.15	28100	0.85
	NSPL	0.39	0.86	0.44	71100	0.93
	NSPH	0.55	0.64	0.25	53100	0.85
2	NPL	0.42	0.42	0.21	35000	0.82
	NPH	0.52	0.34	0.21	28100	0.96
	NSPL	0.39	0.86	0.44	71100	0.99
	NSPH	0.55	0.64	0.28	53100	0.80
3	NPL	0.37	0.48	0.25	39400	0.80
	NPH	0.55	0.31	0.13	26000	0.78
	NSPL	0.38	0.89	0.46	73500	0.79
	NSPH	0.55	0.63	0.27	51900	0.75
4	NPL	0.35	0.50	0.27	41200	0.84
	NPM	0.45	0.39	0.19	32000	0.80
	NPH	0.52	0.33	0.15	27100	0.87
	NSPL	0.38	0.89	0.46	73800	0.76
	NSPM	0.43	0.80	0.39	65600	0.76
	NSPH	0.55	0.63	0.27	51700	0.76
5	NPL	0.38	0.47	0.25	39100	0.74
	NPM	0.46	0.39	0.18	31800	0.72
	NPH	0.56	0.31	0.13	25800	0.77
	NSPL	0.42	1.05	0.52	86500	0.60
	NSPM	0.45	0.77	0.37	63300	0.87
	NSPH	0.55	0.63	0.27	52000	0.93
7	NPL	0.36	0.49	0.26	40400	1.07
	NPM	0.46	0.39	0.19	32400	1.13
	NPH	0.55	0.33	0.14	26800	1.22
	NSPL	0.39	0.92	0.47	75700	0.89
	NSPM	0.45	0.78	0.37	64100	1.03
	NSPH	0.56	0.64	0.27	52400	1.06

Experi-ment	Flow	Depth (m)	Velocity (m/s)	Fr	Re	C_D
8	NPL	0.36	0.51	0.27	41900	1.08
	NPM	0.45	0.41	0.19	33400	1.18
	NPH	0.54	0.33	0.14	27300	1.28
	NSPL	0.38	1.17	0.60	96200	0.64
	NSPM	0.45	0.99	0.47	81800	0.75
	NSPH	0.54	0.83	0.36	68300	0.87
9	NPL	0.36	0.51	0.27	41900	1.07
	NPM	0.44	0.41	0.20	39900	1.07
	NPH	0.56	0.34	0.14	27700	1.07
	NSPL	0.43	1.06	0.52	87300	0.65
	NSPM	0.48	0.95	0.44	78400	0.71
	NSPH	0.56	0.81	0.34	66500	0.80
10	NPL	0.35	0.53	0.28	43400	1.05
	NPM	0.44	0.41	0.20	33900	1.00
	NPH	0.57	0.33	0.14	26900	1.06
	NSPL	0.43	1.05	0.51	86700	0.62
	NSPM	0.48	0.94	0.43	77600	0.69
	NSPH	0.58	0.81	0.34	66700	0.78
11	NPM	0.37	0.45	0.24	37300	1.24
	NPH	0.52	0.32	0.14	26700	1.22
	NSPL	0.30	1.21	0.7	99600	0.78
	NSPM	0.40	0.94	0.47	77300	1.02
	NSPH	0.53	0.73	0.32	60400	1.02

A.2. Pier roughened with sandpaper (Experiments 12 to 14)

Experi-ment	Flow	Depth (m)	Velocity (m/s)	Fr	Re	C_D
12	NPM	0.32	0.53	0.30	44100	1.06
	NPH	0.50	0.34	0.15	28100	1.02
	NSPL	0.34	1.21	0.66	100000	1.05
	NSPM	0.39	1.06	0.54	87400	1.05
	NSPH	0.52	0.82	0.36	67700	1.05
13	NPM	0.37	0.47	0.24	38500	1.23
	NPH	0.51	0.34	0.15	27900	1.12
	NSPL	0.32	1.28	0.72	10500	1.00
	NSPM	0.43	0.99	0.48	81300	1.18
	NSPH	0.55	0.79	0.34	65100	1.04
14	NPM	0.36	0.48	0.26	39600	1.19
	NPH	0.56	0.30	0.13	24700	1.15
	NSPL	0.33	1.32	0.74	109000	0.99
	NSPM	0.46	0.93	0.44	77000	1.13
	NSPH	0.52	0.86	0.38	71000	1.01

A.3. Pier roughened with medium-size sand (Experiments 15 to 17)

Experi-ment	Flow	Depth (m)	Velocity (m/s)	Fr	Re	C_D
15	NPM	0.27	0.62	0.38	51300	0.83
	NPH	0.54	0.31	0.38	51200	0.92
	NSPL	0.32	1.24	0.71	102700	0.89
	NSPM	0.45	0.88	0.41	72300	1.24
	NSPH	0.55	0.78	0.34	64700	1.06
17	NPM	0.31	0.51	0.29	42200	1.07
	NPH	0.52	0.31	0.14	25500	1.25
	NSPL	0.32	1.19	0.67	979000	0.98
	NSPM	0.45	0.87	0.41	71600	1.10
	NSPH	0.57	0.68	0.29	55800	1.15

APPENDIX B. DATA FROM BACKWATER EXPERIMENTS

Table B.1: Data for the 3.5 in. Pier

Experiment	Discharge (m^3/s)	Froude Number	Depth (cm)	$\Delta y/y$
S-1	0.573	0.672	32.62	0.0399
S-2	0.509	0.667	30.28	0.0310
S-3	0.508	0.415	41.43	0.0068
S-4	0.513	0.682	29.98	0.0334
S-5	0.500	0.459	38.36	0.0128
S-6	0.526	0.460	39.59	0.0119
S-7	0.428	0.427	36.32	0.0116
S-8	0.462	0.442	37.33	0.0080
S-9	0.433	0.413	37.35	0.0086
S-10	0.443	0.519	32.60	0.0101
S-11	0.415	0.477	33.00	0.0136
S-12	0.419	0.615	28.03	0.0225
S-13	0.430	0.565	30.19	0.0169
S-14	0.444	0.626	28.91	0.0294
S-15	0.382	0.593	27.04	0.0281
S-16	0.405	0.565	29.05	0.0269
S-17	0.414	0.628	27.45	0.0186
S-18	0.230	0.217	37.59	0.0024
S-19	0.554	0.753	29.54	0.0318
S-20	0.550	0.747	29.57	0.0320
S-21	0.155	0.135	39.60	0.0013
S-22	0.246	0.210	40.22	0.0015
S-23	0.238	0.226	37.45	0.0013
S-24	0.251	0.323	30.55	0.0020
S-25	0.433	0.265	50.28	0.0016
S-26	0.215	0.226	35.06	0.0014
S-27	0.510	0.453	39.19	0.0038
S-28	0.393	0.260	47.73	0.0002

Table B.2: Data for the 6 in. Pier

Experiment	Discharge (m^3/s)	Froude Number	Depth (cm)	$\Delta y/y$
L-1	0.460	0.677	27.99	0.0657
L-2	0.442	0.587	29.97	0.0614
L-3	0.227	0.256	33.33	0.0030
L-4	0.217	0.289	29.87	0.0074
L-5	0.245	0.383	26.87	0.0141
L-6	0.199	0.255	30.60	0.0082
L-7	0.311	0.421	29.55	0.0098
L-8	0.229	0.275	31.99	0.0094
L-9	0.317	0.340	34.52	0.0061
L-10	0.278	0.220	42.30	0.0019
L-11	0.218	0.275	30.95	0.0071
L-13	0.422	0.674	26.51	0.0607
L-14	0.192	0.254	30.00	0.0060
L-15	0.328	0.421	30.68	0.0081
L-16	0.339	0.446	30.14	0.0113
L-17	0.577	0.830	28.44	0.0594
L-18	0.559	0.777	29.09	0.0584
L-19	0.255	0.272	34.63	0.0043
L-20	0.348	0.497	28.53	0.0130
L-21	0.491	0.711	28.30	0.0830

Table B.3: Data for Twin 6 in. Piers

Experiment	Discharge (m^3/s)	Froude Number	Depth (cm)	$\Delta y/y$
2L-1	0.217	0.222	35.7	0.0048
2L-2	0.217	0.233	34.5	0.0046
2L-3	0.173	0.206	32.2	0.0006
2L-4	0.455	0.278	50.3	0.0024
2L-5	0.283	0.158	53.3	0.0030
2L-6		0.130	47.2	0.0008
2L-7	0.194	0.120	49.4	0.0008
2L-8	0.192	0.184	36.0	0.0008
2L-9	0.175	0.213	39.4	0.0013
2L-10	0.241	0.117	50.9	0.0002
2L-11	0.195	0.174	42.1	0.0017
2L-12	0.218	0.129	48.4	0.0010
2L-13	0.201	0.175	40.2	0.0020
2L-14	0.205	0.826	19.8	0.1128
2L-15	0.334	0.672	25.9	0.1005
2L-16	0.406	0.373	38.3	0.0154
2L-17	0.406	0.412	37.5	0.0179
2L-19	0.425	0.563	29.1	0.0405
2L-20	0.448	0.678	27.5	0.0986
2L-22	0.440	0.403	38.4	0.0151
2L-23	0.436	0.845	23.3	0.1351
2L-24	0.436	0.354	41.7	0.0187

Table B.4: Data for the Yarnell Pier

Experiment	Discharge (m^3/s)	Froude Number	Depth (cm)	$\Delta y/y$
Y-1	0.253	0.276	34.10	0.0003
Y-2	0.445	0.700	26.77	0.0635
Y-3	0.441	0.735	25.75	0.0691
Y-4	0.441	0.480	36.21	0.0113
Y-5	0.480	0.451	37.49	0.0053
Y-6	0.475	0.519	34.63	0.0113
Y-7	0.485	0.370	28.62	0.0056
Y-8	0.260	0.290	32.00	0.0022
Y-9	0.241	0.637	28.80	0.0670
Y-10	0.451	0.725	28.11	0.0754
Y-11	0.495	0.733	27.83	0.0855
Y-12	0.493	0.201	35.16	0.0037
Y-13	0.193	0.743	30.35	0.0834
Y-14	0.569	0.744	26.19	0.0634
Y-15	0.457	0.746	30.19	0.0914
Y-16	0.567	0.693	26.60	0.0635
Y-17	0.436	0.237	36.45	0.0025
Y-18	0.240	0.397	39.40	0.0096
Y-19	0.451	0.280	32.32	0.0028
Y-20	0.236	0.559	33.51	0.0188
Y-21	0.498	0.205	31.73	0.0011
Y-22	0.169	0.752	27.11	0.0926
Y-23	0.487	0.542	33.77	0.0160
Y-24	0.488	0.372	35.78	0.0078
Y-25	0.366	0.550	31.03	0.0177
Y-26	0.436	0.508	31.85	0.0154